Soft Responsive Objects that use Catalysis as a Design Tool

by

Ross William Jaggers

A Thesis Submitted in Fulfilment of the Requirements for the Degree of Doctor of Philosophy

Department of Chemistry, University of Warwick

February 2018

Table of Contents

Figures v

Tables viii

Acknowledgements ix

Declaration x

Publications List xi

Abstract xii

Chapter 1: Introduction 1

1.1 Thesis and Outline Scope 1

1.2 References 4

Chapter 2: Independent responsive behaviour and communication in hydrogel objects 7

2.1 Introduction 7

2.2 Results and Discussion 8

2.3 Conclusions 18

2.4 Experimental Methods 18

2.4.1 Materials 18

2.4.2 Microfluidic device construction 20

2.4.3 Composite gel synthesis 20

2.4.4 Hydrogel observation experiments 21

2.5 References 22

Chapter 3: Temporal and spatial programming in soft composite hydrogel objects **24**

3.1 Introduction 24
3.2 Results and Discussion 25
3.3 Conclusions 35
3.4 Experimental methods 35
3.4.1 Materials 35
3.4.2 Gel templates 35
3.4.3 'Pre-gel' formulation 36
3.4.4 Gel cross-linking 37
3.4.5 Object behaviour 37
3.4.6 Colour quantification 37
3.5 References 37

Chapter 4: Communication between hydrogel beads via chemical signalling **40**

4.1 Introduction 40
4.2 Results and Discussion 42
4.3 Conclusions 51
4.4 Experimental methods 51
4.4.1 Materials 51
4.4.2 Gel bead synthesis 51
4.4.2.1 Urease beads 52
4.4.2.2 Urease/silver beads 52
4.4.2.3 Silver beads 52
4.4.2.4 Dithiothreitol beads 52
4.4.3 Communication experiments 53
4.4.4 Full timings breakdown 53
4.5 References 54

Chapter 5: Control of capsule membrane permeability with catalytic particles **57**

5.1 Introduction 57
5.2 Results and discussion 60
5.3 Conclusions 70
5.4 Experimental methods 71
5.4.1 Poly(butyl methacrylate)-*b*-poly(2-dimethylaminoethylmethacrylate) synthesis 71
5.4.1.1 Materials 71
5.4.1.2 Synthesis 72
5.4.1.3 Characterisation 73
5.4.2 Microfluidic Device Construction and Capsule Formation 75
5.4.2.1 Materials 75
5.4.2.2 Preparation of Capsules by Microfluidics 75
5.4.3 Release Measurements 78
5.4.3.1 Triggered release of sodium sulfate from capsules: visual release studies 78
5.4.3.2 Triggered release of sodium fluoride from capsules: quantitative release studies 78
5.4.3.3 Triggered release of congo red dye from capsules: quantitative release studies 79
5.4.4 Quantification of manganese by Inductively Coupled Plasma – Optical Emission Spectroscopy (ICP-OES) detection 80
5.4.5 Confocal Microscopy 81
5.5 References 81

Chapter 6: Functions and applications of particle-vesicle composites **85**

6.1 Introduction 85
6.2 The beginnings of composite vesicles: functional liposomes 87
6.3 Stabilisation of vesicles by particles 88
6.4 Shape changes in vesicles 91
6.5 Moderating membrane permeability 99
6.6 Taxis of vesicles using particles 104
6.7 Conclusions 107
6.8 References 107

Chapter 7: Summary **115**

7.1 Thesis outlook 115
7.2 References 119

Figures

Figure 2.1 Synthesis and action of composite fibres 9
Figure 2.2 Autonomous fibre programming 10
Figure 2.3 The pH change of a fibre by colorimetric indicator 11
Figure 2.4 Fibre disassembly 12
Figure 2.5 Inhibition time at varying concentrations of urease 13
Figure 2.6 The pH change of a fibre by hue angle 14
Figure 2.7 The independent action of fibres of different compositions 15
Figure 2.8 Communication between gels by colorimetric indicator 16
Figure 2.9 Communication between gels by hue angle 17
Figure 2.10 The assembly of a microfluidic device 19
Figure 2.11 pH calibration of bromothymol blue indicator 21

Figure 3.1 The behaviour of ionically cross-linked hydrogel objects 26
Figure 3.2 The synthesis of soft responsive objects 27
Figure 3.3 Analysis of urease migration in hydrogel objects 28
Figure 3.4 Colour change in hydrogel trees with 'active' leaves 29
Figure 3.5 RGB line scans taken across the width of the most left hydrogel leaf 30
Figure 3.6 Plotting of the hue angle over time at selected locations across several line scans 31
Figure 3.7 Disintegration in hydrogel trees with 'active' leaves 32
Figure 3.8 A continuous soft object containing three distinct regions of different enzyme concentrations 34
Figure 3.9 3D designs used to create hydrogel templates 36

Figure 4.1 The three modes of action of a urease loaded hydrogel bead 42
Figure 4.2 The action of silver containing urease beads 43

Figure 4.3 Communication between urease (1 g dm^{-3}) beads and silver beads 45
Figure 4.4 Communication between urease (0.25 g dm^{-3}) beads and silver beads 46
Figure 4.5 Communication between urease (0.125 g dm^{-3}) beads and silver beads 47
Figure 4.6 Communication between dithiothreitol beads and silver containing urease beads 49
Figure 4.7 Communication between urease beads, dithiothreitol beads and silver beads 50

Figure 5.1 The formation of double droplets and capsules 61
Figure 5.2 Dark field microscopy images of capsules and their release 62
Figure 5.3 Cryo-SEM images of capsules with membrane embedded particles 63
Figure 5.4 Fluoride ion release profiles of capsules with and without embedded particles 64
Figure 5.5 Fluoride ion release profiles of *ca.* 6000 particle embedded capsules 65
Figure 5.6 Fluoride ion release of particle-embedded capsules with hydrogen peroxide and water blanks 66
Figure 5.7 Dark field microscopy video stills of capsules under high hydrogen peroxide loadings 67
Figure 5.8 Congo red release profiles of capsules with and without embedded particles 68
Figure 5.9 Confocal microscope image of a partially buckled polymer capsule 69
Figure 5.10 Molar mass distribution plot of the BMA block and the di-block copolymer 72
Figure 5.11 The H^1 NMR spectrum of poly(*n*-butyl methacrylate)-*block*-poly(2-dimethylamino ethyl methacrylate) 73

Figure 5.12 The DSC curve of poly(*n*-butyl methacrylate)-*block*-poly(2-dimethylamino ethyl methacrylate) 74
Figure 5.13 The assembly of a microfluidic device 76
Figure 5.14 A microfluidic device for the formation of monodisperse double droplets 77
Figure 5.15 Congo red loaded capsules embedded with manganese oxide particles before and after hydrogen peroxide triggers 79

Figure 6.1 The various routes towards particle-vesicle composite structures 85
Figure 6.2 Carboxyl-modified gold nanoparticle stabilised liposome and its destabilization at acidic pH 89
Figure 6.3 Fluorescence confocal micrographs of lipid giant vesicles decorated with the thermoresponsive PNIPAM microgels 90
Figure 6.4 Deformation of hollow magnetic shells 92
Figure 6.5 Spreading and transient tubulation in flat giant unilamellar vesicles 93
Figure 6.6 Shape deformation pathways of giant vesicle encapsulating dense colloids 94
Figure 6.7 Shape fluctuations of bounding membrane of vesicles containing hard beads 95
Figure 6.8 Pinched membrane deformations of membranes around beads 96
Figure 6.9 Phase diagram and aggregate snapshots of particle self-assembly on a fluid surface 97
Figure 6.10 Dark field microscopy video stills of capsules under high hydrogen peroxide loadings and fluoride ion release profiles of *ca.* 6000 particle embedded capsules 99
Figure 6.11 Near infrared triggered release using giant vesicles 101
Figure 6.12 Controlled leakage of a giant unilamellar vesicle upon approach of an optically trapped gold nanoparticle 102

Figure 6.13 Carboxyfluorescein leakage from magnetic liposomes 103
Figure 6.14 Composite vesicles containing platinum and gold nanoparticle rich domains 105
Figure 6.15 Vesicle entrapped platinum nanoparticles in the generation of stomatocytes 106

Tables

Table 4.1 Full timings breakdown 53

Acknowledgements

First and foremost, the work in this thesis would not have been possible without the help and support of a number of people within the Department of Chemistry, University of Warwick.

I would like to thank the many *BonLab* team members over the past four years for their encouragement, guidance and friendship. Namely Postdocs Yunhua, Cathy and Corinna, and fellow PhD students Rong, Tom, Rob Y, Rob B, Joe, Mr and Mrs Longbottom, Sam, Andrea, Patrik, Matt, Melody and Josh. Several of you have helped me with my work, and most have stopped me going insane.

Big thanks are also owed to a number of people outside of my research team without whom my life would have been much more difficult. In particular, I thank Jason Noone, Rob Jenkins, Dorothea Mangels, Dianne Walsh, Raj Randev, and Peter Scott who have always gone above and beyond to help me whenever asked. I also want to thank Tara Schiller and Ken Sloan for their support and mentorship.

My greatest thanks go to my friend and supervisor, Stefan. Stefan has always given me the freedom and support to pursue my academic and career goals at Warwick, and has been an outstanding mentor. I leave Warwick safe in the knowledge that I am a better Scientist for having worked with him.

Out in the 'real world', I thank my partner Josh for selflessly listening to me witter on about my research, as well as both inspiring and encouraging me to succeed.

Finally, I am indebted to my parents, Mark and Jane, who have financially and emotionally supported me throughout my many years of education. Without them, I would not have made it this far.

Declaration

This thesis is submitted to the University of Warwick in support of my application for the degree of Doctor of Philosophy. It has been composed by myself and has not been submitted in any previous application for any degree, apart from the following:

(i) The dark field microscopy images that feature in figures 5.2 and 5.7 were taken by Dr Rong Chen, University of Warwick, and were included in his thesis

(ii) The cryogenic scanning electronic microscopy images that feature in figure 5.7 were taken by Dr Rong Chen, University of Warwick, and were included in his thesis

Furthermore,

(iii) The CHN analysis measurements discussed in section 5.4.1.3 were conducted by Warwick Analytical Services Ltd, Coventry

(iv) The ICP-OES analysis measurements discussed in section 5.4.4 were conducted by Mr Philip Aston, University of Warwick

Parts of this thesis have been published by the author and page xi lists these publications.

Signed:  Date: 19/02/2018

Publications List

1. R. W. Jaggers, and S. A. F. Bon, Independent responsive behaviour and communication in hydrogel objects, *Materials Horizons*, 2017, **4**, 402-407, Cover article

2. R. W. Jaggers, and S. A. F. Bon, Temporal and spatial programming in soft composite hydrogel objects, *J. Mater. Chem. B*, 2017, **5**, 7491-7495, Cover article

3. R. W. Jaggers, and S. A. F. Bon, Communication between hydrogel beads via chemical signalling, *J. Mater. Chem. B*, 2017, **5**, 8681-8685

4. R. W. Jaggers, R. Chen, and S. A. F. and Bon, Control of vesicle membrane permeability with catalytic particles, *Materials Horizons*, 2016, **3**, 41-46

5. R. W. Jaggers, and S. A. F. Bon, Functions and applications of particle-vesicle composites, *In preparation*

6. R. V. Bell, T. Heuser, R. W. Jaggers, M. M. Stevens, and S. A.F. Bon, Enzymatic Catalysed Time-Controlled Release of Emulsion Droplets from Soft Matter Fibres, *In preparation*

Abstract

In this thesis, we have developed a series of chemoresponsive soft polymer objects that have either biological or inorganic catalysts integrated into them, namely the enzyme urease or particles of manganese oxide, respectively.

Firstly, we show the fabrication of soft hydrogel fibres and beads that have an individually programmed time delay in their response to a shared environmental stimulus. We utilise the enzyme urease to programme a self-regulated change in pH, which in turn activates fibre disintegration or a change in gel bead colour. This design allows for independent response behaviour of a collection of bodies in a single closed system, as well as inter-material communication on shorter length scales. Secondly, we create continuous objects of non-uniform dimensional composition that selectively respond to an environmental stimulus of urea and change colour or disintegrate at pre-defined locations within the hydrogel structure after pre-set time intervals. This gives objects both time and spatial programming, again using the enzyme urease. Thirdly, we demonstrate more complex chemical communication between millimetre-sized soft hydrogel beads in an aqueous environment. Silver cations (Ag^+) and the Ag^+ chelator dithiothreitol (DTT) are used as signalling molecules, and by exploiting their interplay, we conduct a series of 'conversations' between urease containing millimetre-sized beads. Competitive communication between three beads, whereby the central bead receives two competing signals from two senders, is shown. Lastly, we show giant polymer capsules which have membrane-embedded catalytically active manganese oxide particles, made using droplet-based microfluidics. It is demonstrated that these colloidal particles can regulate the membrane permeability of the capsules upon their exposure to, and catalytic reaction with, small amounts of dissolved hydrogen peroxide.

1 Introduction

"Trying is not succeeding"

- prof. dr. ir. Stefan Bon

1.1 Thesis Scope and Outline

Responsive materials, often termed *smart materials*, are those that are capable of transforming an environmental stimulus into a controlled, material response.[1] Soft smart materials that are typically polymeric in nature,[5] including hydrogels,[6–8] self-assembled structures such as vesicles,[9–11] micelles or worms,[12–14] elastomers,[15] functionalised surfaces,[16,17] polyelectrolyte layer-by-layer capsules,[18] and dispersed media such as emulsions or foams.[19,20]

Inspiration for these materials has, in many cases, been sought from the most sophisticated responsive materials on Earth, namely biological organisms and the soft components that they are composed of.[21] Cells and organisms have evolved the ability to convert environmental information into an active response. A key challenge in materials science is the design and creation of materials, or objects, that possess behaviour and characteristics like this, to generate what are known as biomimetic materials.[24]

Unfortunately, synthetic responsive behaviour is still somewhat rudimentary compared to that of nature. Materials can be designed to react to stimuli such as light, temperature, sound, pressure, chemical triggers, pH or electrolytes.[25] Furthermore, material responses can be wide ranging and include changes in its shape, size or dimensions,[26,27] change in permeability,[28,29] self-propulsion,[30] or self-erasure.[31] Some current and exciting examples include artificial muscles,[32] synthetic cells,[33] entirely soft robots,[34] self-replicating objects,[35] and walking hydrogels.[36]

Luckily, biology has already perfected tools capable of some of these actions by evolving complex bio-machinery that allows cells to function. For example, enzymes, nature's macromolecular biological catalysts, convert substrates into reaction products for use in metabolic processes, and can be readily integrated into man-made materials and objects to create responsive composite materials.[37] Inorganic catalysts operate in much the same way as their enzymatic counterparts,[38] and can also be used to give otherwise dormant materials active, responsive behaviour, without having to synthesise responsive materials from the ground up.

This concept of integrating active biological or inorganic components, namely enzymes or inorganic catalysts, into soft structures to generate responsive, composite materials is what we explore in this thesis. This approach allows us to create objects and materials that respond to environments containing their fuel sources, and when paired with other material actions and properties, we create systems capable of complex, novel behaviours.

In chapter 2, we explore independent responsive behaviour and communication in hydrogel objects. This chapter shows the fabrication of soft hydrogel alginate-based objects, namely fibres and beads, which have an individually programmed time delay in their response to a shared environmental stimulus. We utilise the enzyme urease to programme a self-regulated change in pH, which in turn activates the designed response of gel fibre disintegration or a change in gel bead colour. This design allows for independent response behaviour of a collection of bodies in a single closed system, as well as inter-material communication on shorter length scales.

In chapter 3, we build on the principles outlined in chapter 2 in the design and fabrication of soft composite hydrogel objects with temporal and spatial programming. Objects are, again, formed from the biopolymer sodium alginate, the enzyme urease, and oil droplets, and are formed by a simple gelation procedure to produce autonomous bodies with both time and spatial programming. These

continuous objects of non-uniform dimensional composition selectively respond to an environmental stimulus of urea and change colour or disintegrate at pre-defined locations within the hydrogel structure after pre-set time intervals.

Chapter 4 further explores chemical communication between millimetre-sized soft hydrogel beads in an aqueous environment. Silver cations (Ag^+) and the Ag^+ chelator dithiothreitol (DTT) are used as signalling molecules that, by exploiting their interplay with the enzyme urease, are used to conduct a series of 'conversations' between millimetre-sized beads. Competitive communication between three beads, whereby a central bead receives two competing signals from two senders, is shown.

Chapter 5 takes a look at using inorganic catalysis as a tool for making responsive soft materials, where capsule membrane permeability is controlled using catalytic particles. Giant polymer capsules which have membrane-embedded catalytically active manganese oxide particles are made using droplet-based microfluidics. It is demonstrated that these colloidal particles can regulate the membrane permeability of the polymersomes upon their exposure to, and catalytic reaction with, small amounts of dissolved hydrogen peroxide.

Chapter 6 explores the concepts set out in chapter 4 and offers a broader literature review of a selection of interesting particle-vesicle composites, considering the various merits and applications of such structures.

Finally, chapter 7 considers the outlook and future perspectives of the results obtained in chapters 1 – 4.

1.2 References

1 A. C. Balazs and J. M. Yeomans, *Soft Matter*, 2010, **6**, 703–704.

2 J. N. Israelachvili, *Intermolecular and surface forces*, Academic Press, Cambridge, MA, 2011.

3 A. Seeboth, D. Lötzsch, R. Ruhmann and O. Muehling, *Chem. Rev.*, 2014, **114**, 3037–3068.

4 J. Curie and P. Curie, *Bull. la Société minéralogique Fr.*, 1880, **3**, 90–93.

5 P. T. Mather, *Nat. Mater.*, 2007, **6**, 93–94.

6 H. Yuk, S. Lin, C. Ma, M. Takaffoli, N. X. Fang and X. Zhao, *Nat. Commun.*, 2017, **8**, 14230.

7 C. Zhu, J. Zhao, K. Kempe, P. Wilson, J. Wang, T. Velkov, J. Li, T. P. Davis, M. R. Whittaker and D. M. Haddleton, *Macromol. Biosci.*, 2017, **17**, 1600320.

8 S. J. Buwalda, K. W. M. Boere, P. J. Dijkstra, J. Feijen, T. Vermonden and W. E. Hennink, *J. Control. Release*, 2014, **190**, 254–273.

9 H. Lomas, I. Canton, S. MacNeil, J. Du, S. P. Armes, A. J. Ryan, A. L. Lewis and G. Battaglia, *Adv. Mater.*, 2007, **19**, 4238–4243.

10 A. Joseph, C. Contini, D. Cecchin, S. Nyberg, L. Ruiz-Perez, J. Gaitzsch, G. Fullstone, X. Tian, J. Azizi, J. Preston, G. Volpe and G. Battaglia, *Sci. Adv.*, 2017, **3**, e1700362.

11 K. Kita-Tokarczyk, J. Grumelard, T. Haefele and W. Meier, *Polym. J.*, 2005, **46**, 3540–3563.

12 A. M. Funhoff, S. Monge, R. Teeuwen, G. A. Koning, N. M. E. Schuurmans-Nieuwenbroek, D. J. A. Crommelin, D. M. Haddleton, W. E. Hennink and C. F. van Nostrum, *J. Control. Release*, 2005, **102**, 711–24.

13 P. A. FitzGerald, S. Gupta, K. Wood, S. Perrier and G. G. Warr, *Langmuir*, 2014, **30**, 7986–7992.

14 N. J. Warren and S. P. Armes, *J. Am. Chem. Soc.*, 2014, **136**, 10174–10185.

15 Q. Wang, G. R. Gossweiler, S. L. Craig and X. Zhao, *J. Mech. Phys. Solids*, 2015, **82**, 320–344.

16 D. Wang, S. Guo, Q. Zhang, P. Wilson and D. M. Haddleton, *Polym.*

Chem., 2017, **8**, 3679–3688.

17 N. Nath and A. Chilkoti, *J. Am. Chem. Soc.*, 2001, **123**, 8197–8202.

18 J. J. Richardson, J. Cui, M. Björnmalm, J. A. Braunger, H. Ejima and F. Caruso, *Chem. Rev.*, 2016, **116**, 14828–14867.

19 Y. Chen, N. Ballard and S. A. F. Bon, *Chem. Commun.*, 2013, **49**, 1524.

20 R. V. Bell, C. C. Parkins, R. A. Young, C. M. Preuss, M. M. Stevens and S. A. F. Bon, *J. Mater. Chem. A*, 2016, **4**, 813–818.

21 D. A. Hammer and N. P. Kamat, *FEBS Lett.*, 2012, **586**, 2882–2890.

22 A. Santner and M. Estelle, *Nature*, 2009, **459**, 1071–1078.

23 A. S. P. Jansen, X. Van Nguyen, V. Karpitskiy, T. C. Mettenleiter and A. D. Loewy, *Science*, 1995, **270**, 644–646.

24 P. Fratzl and F. G. Barth, *Nature*, 2009, **462**, 442–448.

25 M. Wei, Y. Gao, X. Li and M. J. Serpe, *Polym. Chem.*, 2017, **8**, 127–143.

26 Y. Zhang and L. Ionov, *Langmuir*, 2015, **31**, 4552–4557.

27 C. M. Yakacki, *Polym. Rev.*, 2013, **53**, 1–5.

28 S. Yu, T. Azzam, I. Rouiller and A. Eisenberg, *J. Am. Chem. Soc.*, 2009, **131**, 10557–10566.

29 J. Du and S. P. Armes, *J. Am. Chem. Soc.*, 2005, **127**, 12800–12801.

30 D. A. Wilson, R. J. M. Nolte and J. C. M. van Hest, *Nat. Chem.*, 2012, **4**, 268–274.

31 M. Tena-Solsona, B. Rieß, R. K. Grötsch, F. C. Löhrer, C. Wanzke, B. Käsdorf, A. R. Bausch, P. Müller-Buschbaum, O. Lieleg and J. Boekhoven, *Nat. Commun.*, 2017, **8**, 15895.

32 A. Simaite, F. Mesnilgrente, B. Tondu, P. Souères and C. Bergaud, *Sensors Actuators B Chem.*, 2016, **229**, 425–433.

33 R. J. R. W. Peters, M. Marguet, S. Marais, M. W. Fraaije, J. C. M. van Hest and S. Lecommandoux, *Angew. Chemie Int. Ed.*, 2014, **53**, 146–150.

34 M. Wehner, R. L. Truby, D. J. Fitzgerald, B. Mosadegh, G. M. Whitesides, J. A. Lewis and R. J. Wood, *Nature*, 2016, **536**, 451–455.

35 T. Wang, R. Sha, R. Dreyfus, M. E. Leunissen, C. Maass, D. J. Pine, P. M. Chaikin and N. C. Seeman, *Nature*, 2011, **478**, 225–228.

36 D. Morales, E. Palleau, M. D. Dickey and O. D. Velev, *Soft Matter*, 2014,

10, 1337–1348.

37 D. Brady and J. Jordaan, *Biotechnol. Lett.*, 2009, **31**, 1639–1650.

38 P. Munnik, P. E. de Jongh and K. P. de Jong, *Chem. Rev.*, 2015, **115**, 6687–6718.

2 Independent responsive behaviour and communication in hydrogel objects

This chapter details research published in the paper: R. W. Jaggers and S. A. F. Bon, *Materials Horizons*, 2017, **4**, 402-407

2.1 Introduction

Living organisms can exhibit autonomy in their response to an external stimulus, a concept that drives both biological function and independent behaviour.[1–3] Some form of intelligence is required to act in this way, and it is this principle that underpins the design of artificial life.[4,5] For example, neural networks model the human brain and robotic devices can perform complex tasks.[6,7]

A key question in material design is "*can this complex concept be stripped down to its essence without loss of autonomy?*".

A multitude of materials translate environmental stimuli into direct material responses. Examples include the catalytically driven actuation of colloidal particles,[8–10] light-triggered inversion of emulsions[11] and triggered change in capsule permeability.[12–15] Though simple stimuli-response pathways can generate sophisticated behaviour, control is often dominated by the environmental cues, not the material itself.[16]

Alternatively, materials that moderate their own behaviour over time and selectively respond to their environments display autonomy and more closely resemble those found in nature.[17,18] For example, the oscillatory Belousov-Zhabotinsky reaction has been used as an internal driver and communication tool,[19,20] kinetic control has been used to trap supramolecular self-assemblies in metastable states,[21–23] and homeostatic control has been demonstrated.[24–26]

Furthermore, enzymes have been used to programme the time-domain, as in the case of pH-responsive self-assemblies that utilize an internal feedback system.[27–29]

Here we show the fabrication of soft hydrogel objects, namely fibres and beads, that have an individually programmed time delay in their response to a shared environmental stimulus. We utilise the enzyme urease to programme a self-regulated change in pH, which in turn activates the designed response of gel fibre disintegration or a change in gel beads colour.

Remarkably, we not only observe the desired independent response behaviour in a collection of bodies in a closed system, but also inter-material communication on shorter length scales. We believe that the incorporation of response time control and communication into the design of hydrogel objects aids the development of autonomous materials.

2.2 Results and Discussion

Aqueous solutions of sodium alginate (1 wt. % for fibres, 5 wt. % for beads, at pH 7) were used as the base material to construct hydrogels. Calcium chloride hexahydrate was used as a source of calcium ions to establish ionic cross-linking. Once formed using fluidic devices, these Ca^{2+} cross-linked hydrogels are stable when dispersed in water over a wide pH range. Alginate-based hydrogels are widely used in food, personal care, and pharmaceutical applications.[30]

For fibres, we employed a flow focussing device (see figure 2.1) which allows for coloured oil droplets to be embedded along the length. The oil droplets were used to distinguish fibres from one another as well as a way to track their disassembly. The sodium alginate solution contained varying amounts of the enzyme urease, which together with the oil droplets becomes entrapped upon crosslinking into the hydrogel matrix.[31] The enzyme is introduced to indirectly control pH over time within the fibre. It does this by converting urea, added to the liquid environment in which the gels are placed, into ammonia and carbon dioxide. Importantly, the

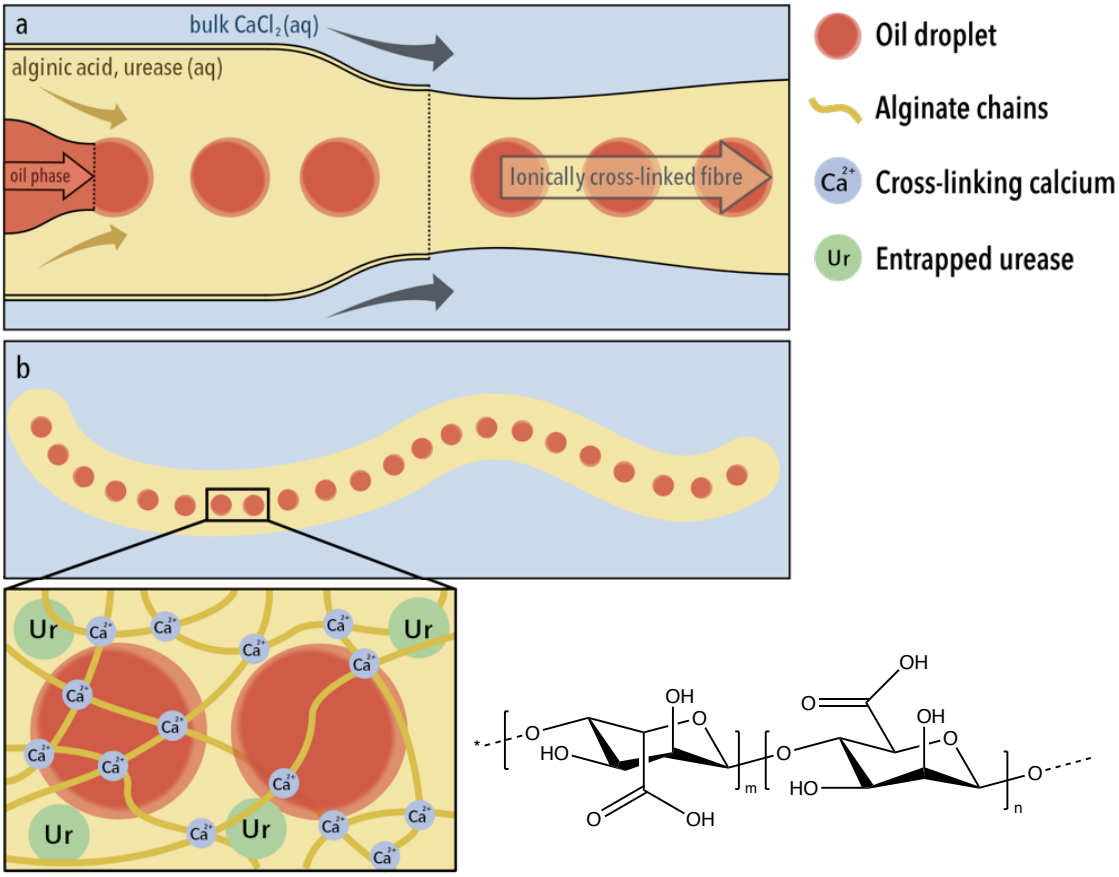

Figure 2.1 | Synthesis and action of composite fibres **(a)** Formation of calcium ion cross-linked alginic acid fibres using a microfluidic synthesis. A fluid stream of alginic acid solution (1 wt. %) containing oil droplets meets a bulk solution containing calcium ions (0.1 mol dm^{-3}), upon which an ionically cross-linked gel fibre forms **(b)** The gel network, cross-linked by calcium ions, entraps both the enzyme urease and oil droplets. The structure of alginic acid, a linear copolymer with homopolymeric blocks of (1-4)-linked β-D-mannuronate (m) and α-L-guluronate (n), is shown.

activity of urease is pH dependent, with a bell-shaped activity curve (See panel b *material time programming* and legend for its mathematical fit, figure 2.2).[32]

When we place one of our hydrogel fibres (10 g dm^{-3} urease) into acidic water of pH 4 in the presence of urea (0.09 mol dm^{-3}) and bromothymol blue as a pH colorimetric indicator, it becomes evident that the local pH rises from within the

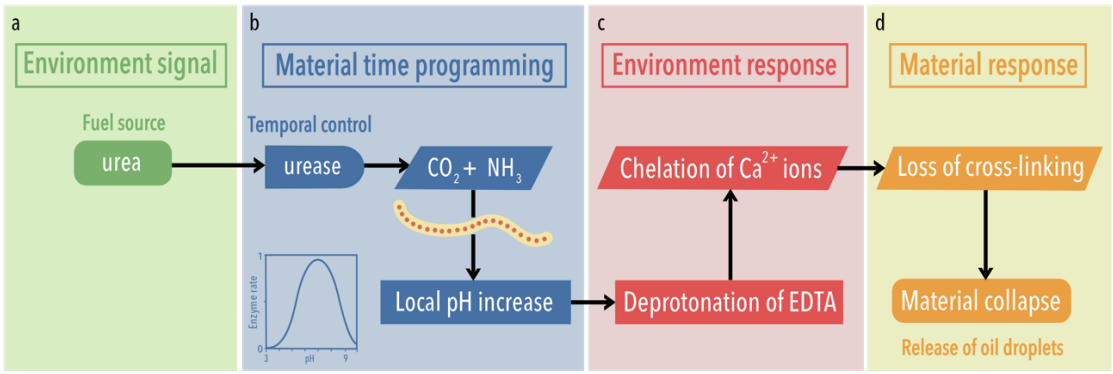

Figure 2.2 | Following a course of programmed behaviour, the fibre converts urea, the fuel, to ammonia, due to the inclusion of urease in its structure (**a**) after a defined time period, the fibre generates a local increase in pH (**b**) this time-programming is afforded due to the bell-shaped activity curve of urease, where the relative enzyme rate, $v' = (1+ 2 \times 10^{-9}/[H^+] + [H^+]/5 \times 10^{-6})^{-1}$. Graph reproduced from reference 32. (**c**) Within the low pH (3.50) bulk environment, partially protonated ethylenediaminetetraacetic acid (EDTA) can be found. As the pH of the fibre increases locally, EDTA is deprotonated locally and chelates calcium ions (**d**) This results in a loss of cross-linking and the release of oil droplets.

fibre is a direct result of enzyme activity (see video that accompanies the paper DOI: 10.1039/C7MH00033B, and figure 2.3).

Our first goal in autonomous hydrogel material design is to demonstrate programmed time delay in the disintegration of the fibres and thus release of the oil droplets.

The sodium salt of ethylenediaminetetraacetic acid (EDTA) is added to the bulk aqueous solution as a chelating agent for calcium ions, acting as a dormant Ca^{2+}-sink. The initial pH of the aqueous medium containing both EDTA and urea in which the fibres are placed is set at a value of 3.50. EDTA has a maximum binding affinity for Ca^{2+} at high pH, when all 6 of its donor groups (4 carboxylic acid groups and 2 nitrogens) are ionised. At pH 7.5, only a fraction of the EDTA will be in this form, thus its affinity will be reduced.[33] This affinity continues to decrease as the pH is lowered. This was verified by placing a hydrogel fibre into

an EDTA solution of pH 3.50 without urea. Without the ability to raise its pH, it remained intact over a period of at least 5 days.

When urea is present in the hydrogel fibre environment (see panel a, *environmental trigger*, figure 2.2), the specific amount of enzyme entrapped within the fibre controls the increase in pH as a function of time (panel b, *material time programming*). The bell-shaped pH-activity curve of urease allows us to use its auto-catalytic behaviour as a tool for time-programming. With low enzyme activity at low pH values, the generation of base provides a positive feedback mechanism that

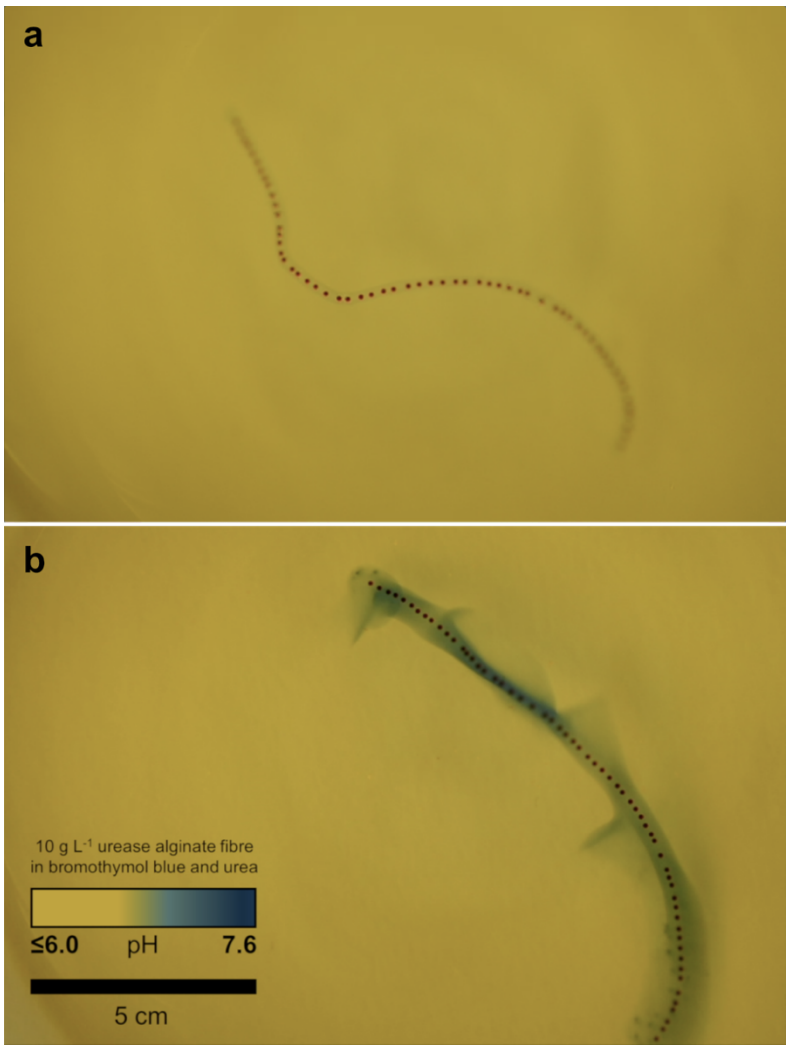

Figure 2.3 | The pH change of a fibre containing 10 g dm^{-3} of urease is followed using the indicating dye bromothymol blue (BMB). As the pH locally increases, a change from yellow to blue is observed, shown in images **a** and **b**, respectively.

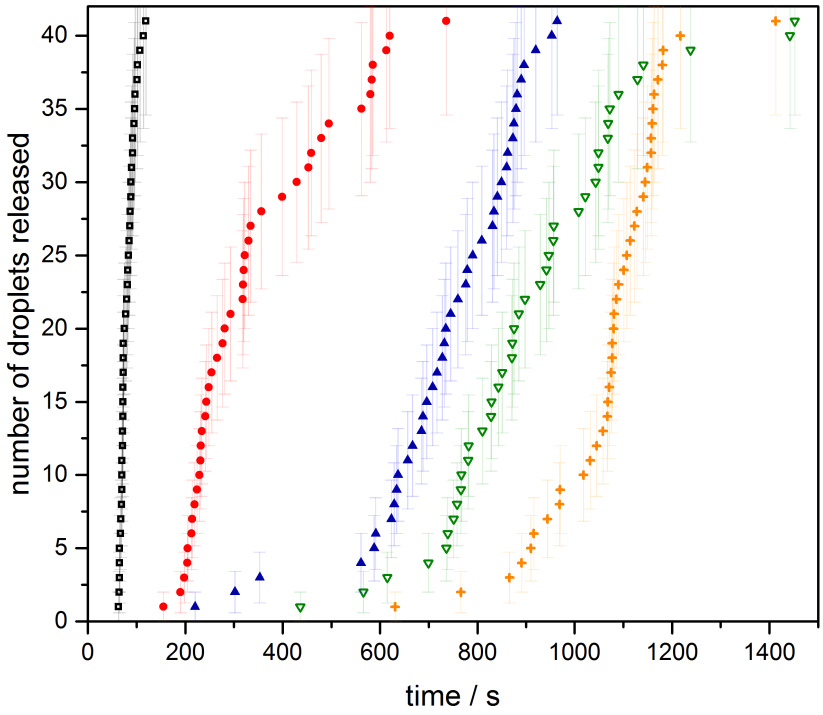

Figure 2.4 | Fibre disassembly. The release of 41 entrapped oil droplets from fibres with different enzyme loadings, 10 (■), 8 (●), 6 (▲), 5 (▽) and 4 g dm^{-3} (+), is tracked. As enzyme concentration within the fibre decreases, release follows after an increasingly longer dormancy period. Square root error bars.

elevates the pH into the higher activity window. The transition from low to high pH follows sigmoidal behaviour, which allows for easy introduction of a dormancy period by variation of the enzyme concentration. A higher enzyme concentration results in a shorter dormancy period.

Upon a pH increase inside and in close proximity of the fibre, EDTA transitions to its Ca^{2+} chelating form, hereby promoting cation exchange (figure 2.2, panel c, *environment response*). This results in the eventual disintegration of the alginate-gel matrix and subsequent release of the entrapped oil droplets (panel d, *material response*).

A series of hydrogel fibres each containing 41 oil droplets were fabricated with urease concentrations of 4.0, 5.0, 6.0, 8.0, and 10.0 g dm^{-3}. The rate of fibre disintegration was tracked by measuring the release of the entrapped oil droplets

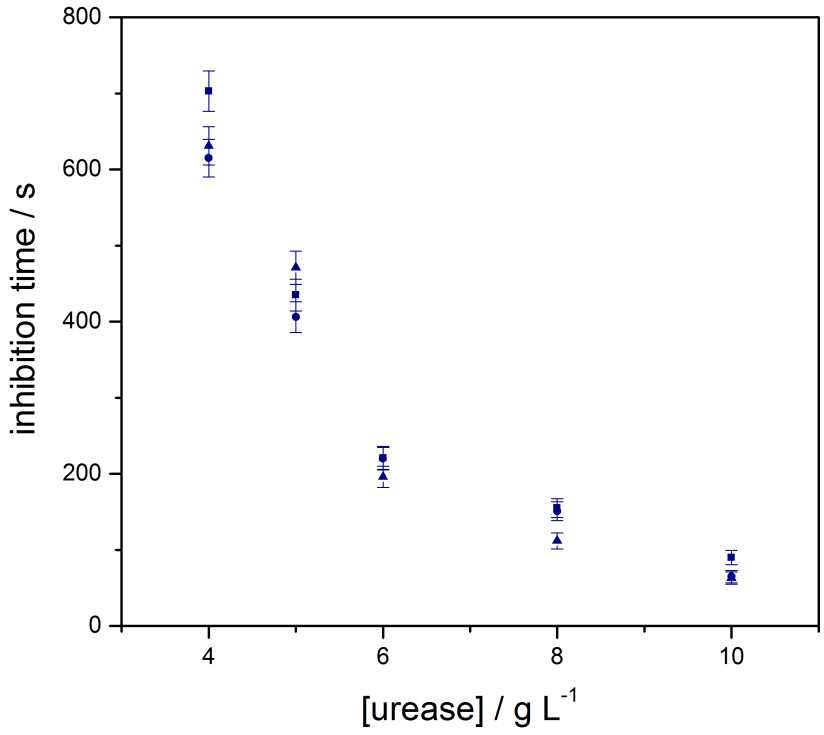

Figure 2.5 | Inhibition time at varying concentrations of urease. As the concentration of urease increases, the inhibition time prior to material disassembly (defined here as the time taken for the first oil droplet to be released) is reduced. This results in a shorter dormancy period. Square root error bars.

(See figure 2.4 and figure 2.5). An increase in enzyme loading leads to a shorter dormancy period before hydrogel matrix collapse, characterised by droplet release. To confirm the relationship between droplet release and pH increase, we analysed the colour changes seen in the previously mentioned bromothymol blue indicator experiment (figure 2.6). We quantify this change in colour by measuring the hue angle of the corresponding HSV histogram. Fibres were analysed using ImageJ to collect an RGB (the red, green, blue additive colour model) histogram of their total area, excluding white reflection spots. These three-figure RGB coordinates can be converted into the alternative three-figure HSV (hue, saturation, value) coordinates and this hue value can be plotted. By calibrating colour against pH (figure 2.11), figure 2.6 is produced.[34]

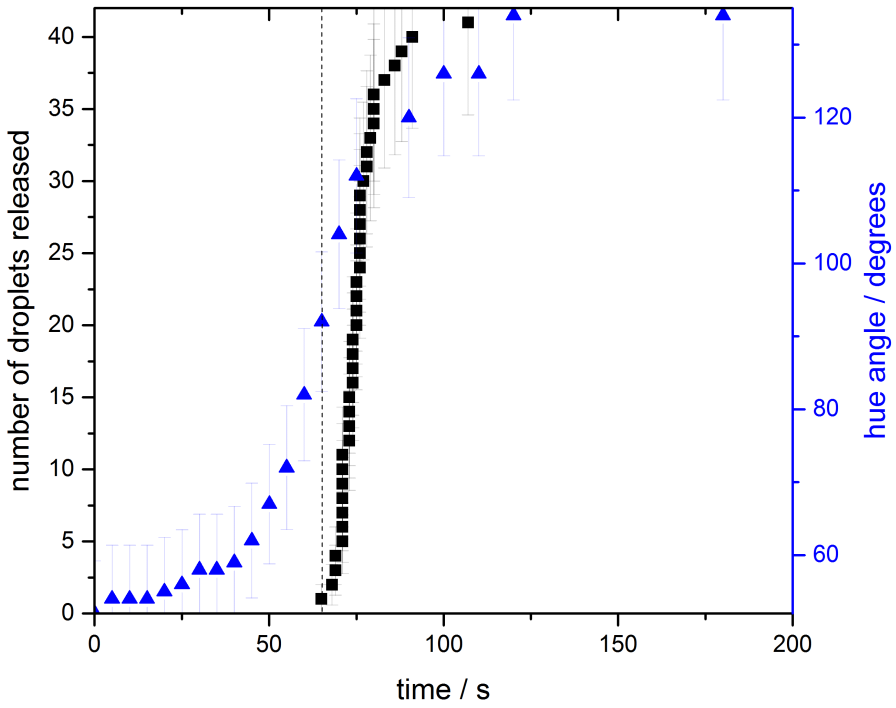

Figure 2.6 | The pH change of a fibre containing 10 g dm^{-3} of urease is followed using the indicating dye bromothymol blue (BMB). As the pH locally increases, a change from yellow to blue is observed. By taking an RGB histogram and converting to HSV, the change in hue angle, and by extension, colour, is monitored (▲) and compared to disassembly of the 10 g dm^{-3} fibre (■). Onset of fibre disassembly corresponds to a hue angle of 92 degrees, equal to a pH of 6.3 (see calibration in figure 2.11 in the experimental methods section). Square root error bars.

The fibre starts with a hue angle of *ca.* 50 °, corresponding to a yellow colour, and finishes with an angle of *ca.* 140°, typical of a blue colour. Not only does the shape of the release curves resemble that of the pH change, but the pH at which fibre disassembly starts can be deduced by means of a hue angle-pH calibration, shown in figure 2.11 (experimental methods). Disassembly starts at a pH of approximately 6.3.

As we can program bespoke time delay in the disintegration behaviour of the fibres, a collection of them can act independently in a single closed system. To demonstrate this, a set of fibres with urease concentrations of 10.0, 8.0 and 4.0 g

dm^{-3} were prepared, containing red, blue, and orange oil droplets, respectively. As in the case of the single fibre experiments, a reduction in urease concentration leads to a longer inhibition period, such that the fibres disintegrate in a pre-defined order, as shown in figure 2.7 and the video that accompanies the paper, DOI: 10.1039/C7MH00033B. The corresponding dormancy time periods were in approximate agreement with the results presented in figures 2.4 and 2.5.

At first glance, self-regulating behaviour means that disintegration of one fibre should not affect the others. Upon closer inspection of the video footage,

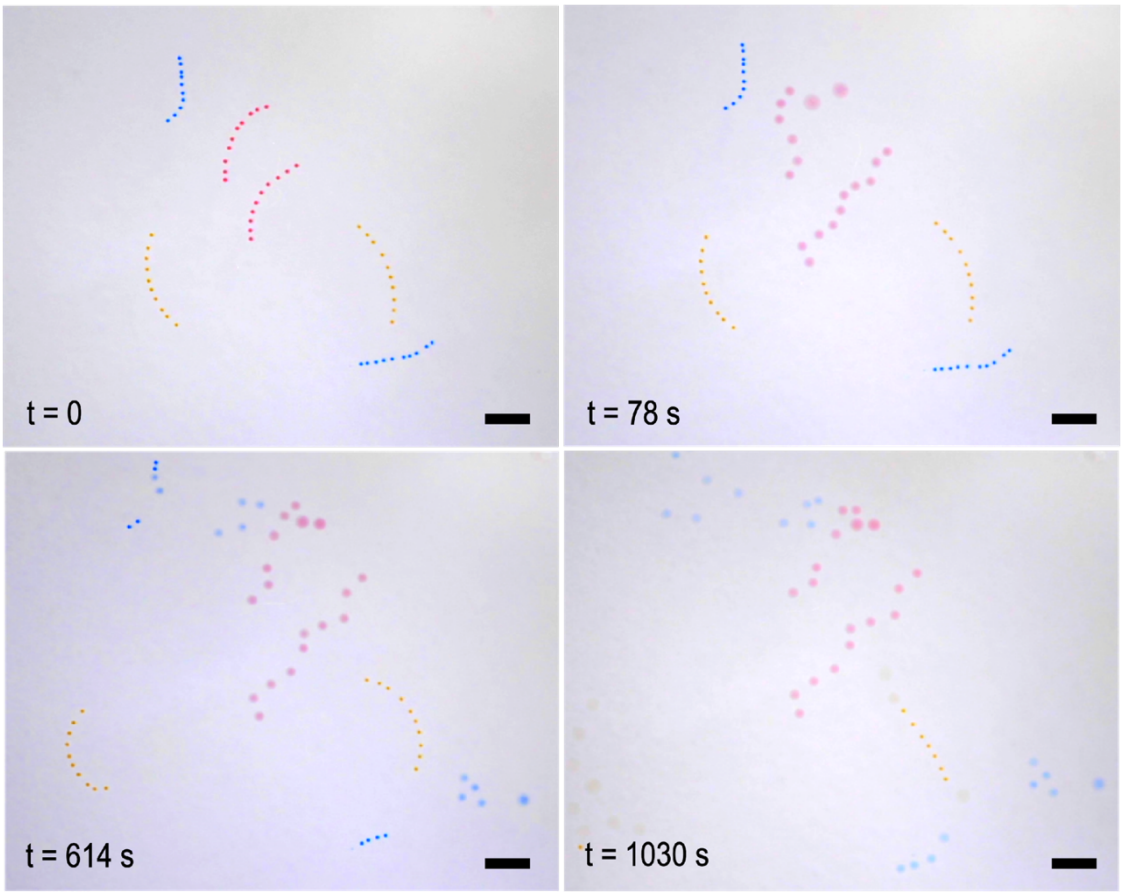

Figure 2.7 | The independent action of fibres of different compositions in a closed system. Three populations of fibres can be seen: 10 g dm^{-3} (red), 8 g dm^{-3} (blue) and 4 g dm^{-3} (orange). Fibres of a higher enzyme concentration start to disassemble before those of a lower concentration. At the beginning, all fibres are intact. After 78 seconds, only the red fibres have released their oil droplets. After 614 seconds, the blue fibres have released their droplets and after 1030 seconds, the orange fibres have released theirs. Scale bar = 1 cm.

however, it appears that the disintegration of the red fibre at the top influences that of its less active neighbour, a blue one. This observation prompted us to look at how the gels might communicate with one another, and in turn, the effect this has on their programmed behaviour.

For this we designed an experiment (lasting approximately 1000 seconds, see figure 2.8) in which a gel bead of high enzyme concentration (1.0 g dm^{-3}) already at high pH, as indicated by its blue colour originating from bromothymol blue, makes

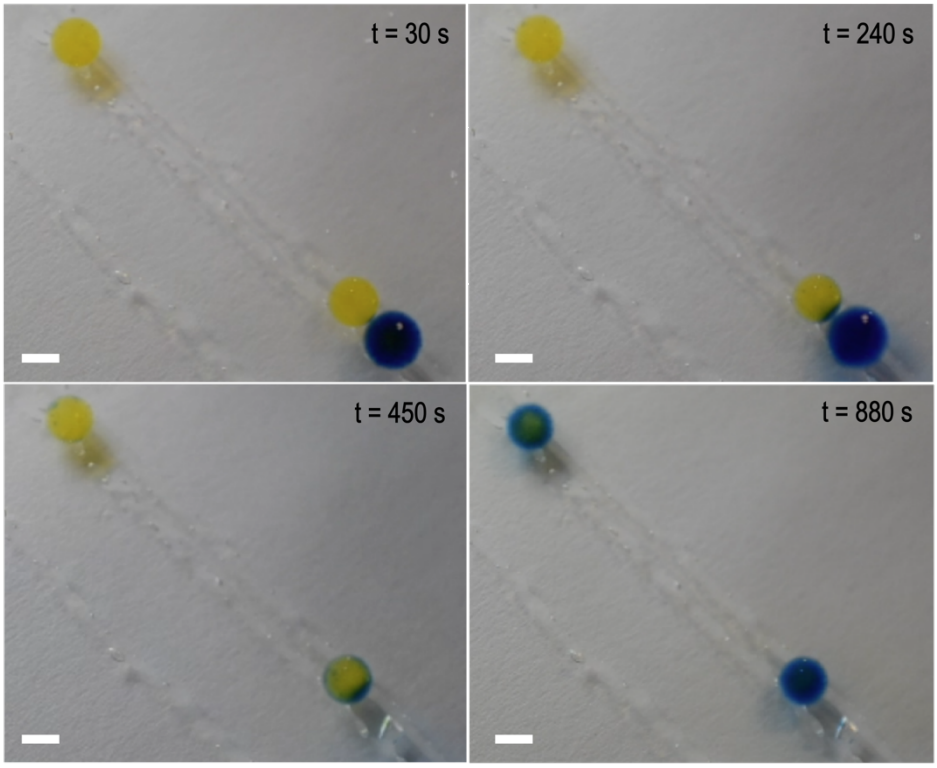

Figure 2.8 | Communication between gels. Alginic acid gel beads containing 0.008 g dm^{-3} of urease and the indicating dye bromothymol blue (BMB) are placed in a bath of urea at pH 3.50 (the yellow beads at 30 seconds). A gel bead containing 10 g dm^{-3} of urease is temporarily introduced, touching only one of the two 0.008 g dm^{-3} urease beads. This higher concentration bead has already been exposed to a urea solution and produces ammonia locally, and can be seen 'infecting' the bead it touches (t = 240 and 450 seconds). As a result, the infected bead transitions from a low to high pH at a faster rate than its uninfected partner. Scale bar = 0.5 cm. See video that accompanies the paper DOI: 10.1039/C7MH00033B.

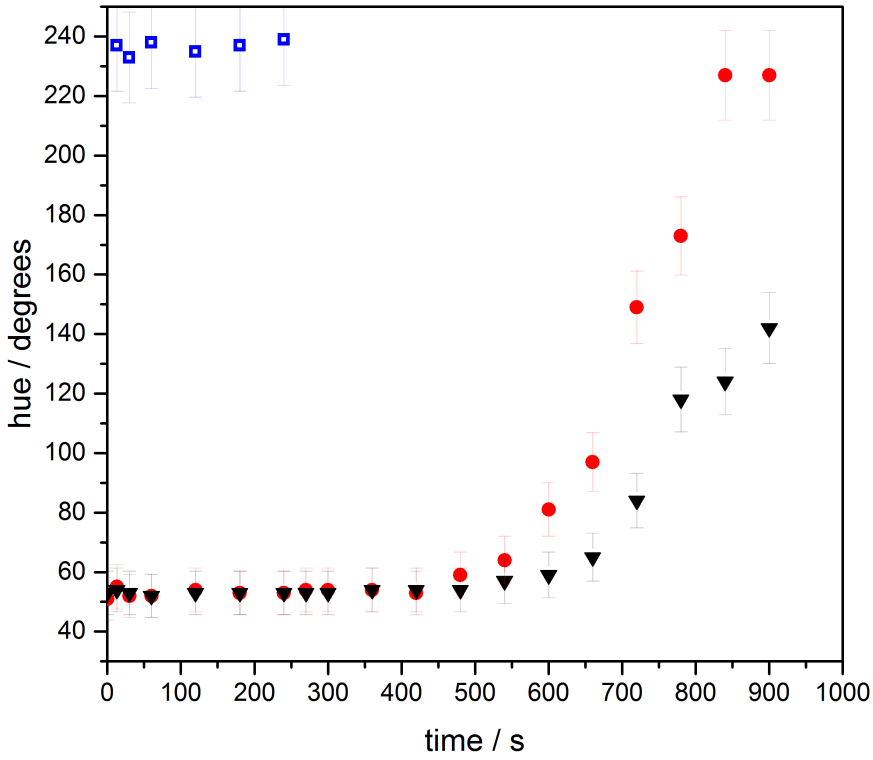

Figure 2.9 | Communication between gels. Alginic acid gel beads containing 0.008 g dm^{-3} of urease and the indicating dye bromothymol blue (BMB) are placed in a bath of urea at pH 3.50 (● and ▼). A gel bead containing 10 g dm^{-3} (the blue bead at 30 seconds, □) of urease is temporarily introduced, touching only one of the two 0.008 g dm^{-3} urease beads (●). This higher concentration bead has already been exposed to a urea solution and produces ammonia locally, and can be seen 'infecting' the bead it touches (t = 240 and 450 seconds). As a result, the infected bead transitions from a low to high pH at a faster rate than its uninfected partner (▼), as indicated by BMB. Hue values are calculated by taking an RGB histogram and converting to HSV. Square root error bars.

temporary contact (240 seconds) with one of two yellow beads of lower urease concentration (0.008 g dm^{-3}) in a pH 3.50 urea solution. Contact with the blue bead 'infects' the yellow bead and it transitions faster to blue (exceeding a pH of 7.6 as indicated by the presence of bromothymol blue and quantified in figure 2.9) than its unaffected counterpart. A plausible explanation is that the transient pH increase generated by the first bead drives the lower concentration bead up its bell-shaped pH activity curve due to the diffusion of locally generated base. This push

decreases the pre-programmed dormancy period and allows the infected gel bead to reach a higher pH in a shorter time period. We quantify this change in colour as before by measuring the hue angle. The two 0.008 g dm^{-3} beads start with a hue angle of *ca.* 50 °, corresponding to a yellow colour. The 1 g dm^{-3} bead has an angle of *ca.* 230 °, typical of a deep blue colour. Over the course of the experiment the triggered bead reaches this maximum hue angle whilst the un-triggered bead does not. This is due to an increased dormancy period and a slower rate of change.

2.3 Conclusions

To conclude, our studies show that it is possible to design and fabricate hydrogel objects that can react with time control in response to a trigger originating from their environment. This provides a level of autonomy and ultimately shifts control from the environment to the material itself. Additionally, communication between nearby hydrogel objects was demonstrated. We believe that the combination of uniquely programmed response behaviour and communication opens up exciting opportunities in the design of soft robotic materials that are capable of signal transduction. As an example, soft robotic objects have to rely on the ability to send signals and act upon them in often complex environments. A chemical signalling pathway is an obvious choice. A collection of synthetic 'tissues' or 'organs' may receive a shared stimulus, and need to act differently and independently. The ability to build soft systems with independent function operating in the same physical space brings us closer to this biologically inspired design.

2.4 Experimental methods

2.4.1 Materials

Alginic acid sodium salt (referred to as sodium alginate in this paper), calcium chloride hexahydrate (98%), urease from Canavalia ensiformis (Jack bean) type III (100K units), urea (99.0 - 100.5%), oil blue N (96%) and oil red O were purchased

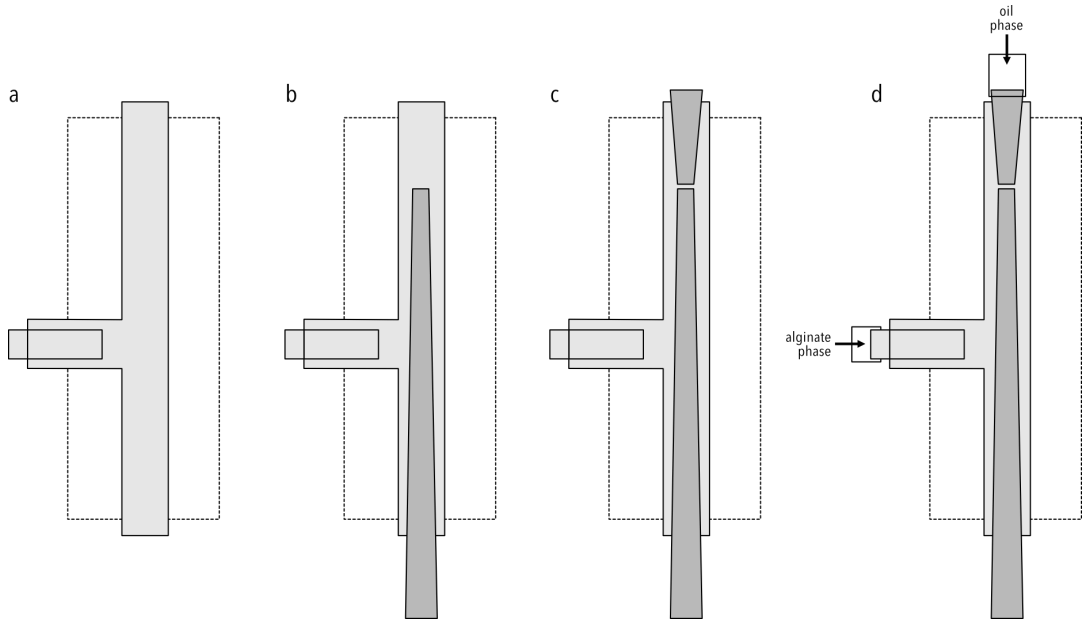

Figure 2.10 | The assembly of a microfluidic device, from left to right, a-d (a) creation of outer phase channel (b) insertion of the flow focused collection capillary (c) insertion of the flow focused middle phase capillary (d) connection of aqueous and oil phases through feed tubing connected to pump-driven syringes.

from Sigma Aldrich. Ethylenediaminetetraacetic acid (99%) was purchased from Avocado Research Chemicals Ltd. and hydrochloric acid (37%) was purchased from VWR international. Vegetable oil was purchased from Costcutters Ltd. Bromothymol blue, ACS reagent, was purchased from Fisher Scientific. Oleoresin paprika oil 80,000 NS was purchased from Kalsec.

Standard wall borosilicate glass capillaries (GC100-10, OD 1.0 mm, ID 0.58 mm and GC200-7.5, OD 2.0 mm, ID 1.16 mm) were purchased from Harvard Apparatus. Evo-Stik Two Part epoxy resin was applied to seal the capillaries where necessary. Solutions were introduced to the microfluidic device through the Clear Tygon® tubing (0.8 mm ID, ColePalmer) attached to syringes driven by positive displacement syringe pumps (Harvard Apparatus, PHD 2000 series). Weller Dispensing Needles KDS3012P (GA 30, ID 0.15 mm) were used to connect the tubing to the microfluidic device.

2.4.2 Microfluidic device construction

A glass capillary with an inner and outer diameter of 1.16 mm and 2.00 mm, respectively, forms the outer casing of the device and contains the flow of the aqueous alginate phase. Within this, two capillaries with inner and outer diameters of 0.58 mm and 1.00 mm, respectively, were tapered to 110 μm with a laser puller to allow flow focusing of the inner oil phase. These tapered capillaries were aligned to create a flow-focused junction where droplets of oil are formed. The output capillary of the device is angled into a bath of 0.1 mol dm^{-3} aqueous calcium chloride solution.

2.4.3 Composite gel synthesis

A vegetable oil phase containing 2 mg cm^{-3} of either oil red O, oil blue N or paprika oil was pumped through a 1 wt. % solution of sodium alginate of the desired urease concentration to form droplets of low size dispersity. This oil droplet containing flow of alginate solution was collected in a continuous phase of 0.1 mol dm^{-3} calcium chloride hexahydrate, where upon an alginate-droplet cable was formed. Typical flow rates were 0.005 mL min^{-1} for the oil phase and 0.15 mL min^{-1} for the aqueous alginate phase. This procedure generates calcium cross-linked sodium alginate hydrogel fibres in which the enzyme urease is entrapped, where it is locally confined but its activity is retained. 300 μm diameter oil droplets are embedded along the length of the fibre, their positions fixed until cross-linking in the gel matrix is disrupted. Fibres of 41 droplets in length are used for the fibre studies in all cases. These are cut from a freshly synthesised length of fibre, of which the enzyme-sodium alginate solution was prepared that day.

Fibres were washed in distilled water and deposited into 20 cm^3 of 0.1 mol dm^{-3} ethylenediaminetetraacetic acid (EDTA) containing 2 cm^3 of 1 mol dm^{-3} urea, corrected to a pH of 3.5 using a 1 mol dm^{-3} hydrochloric acid solution. Fibres are stable in this solution over a matter of days, eventually disintegrating after this time (a considerably longer timescale than studied here).

2.4.4 Hydrogel observation experiments

Responsive behaviour was filmed on a Nikon D5100 camera with AF-S DX Micro NIKKOR 40mm f/2.8G Lens immediately following the addition of the fibre to the urea/EDTA solution.

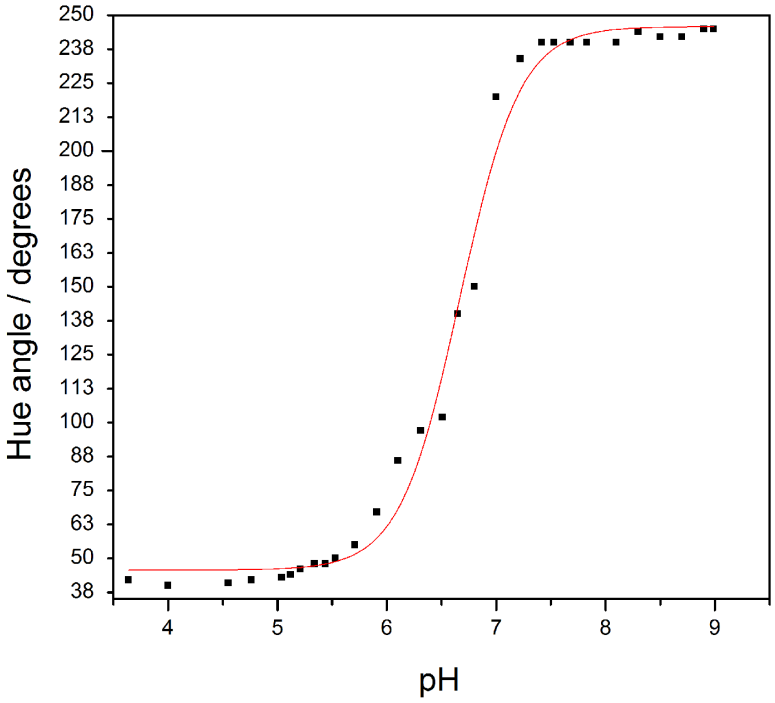

Figure 2.11 | pH calibration of bromothymol blue indicator. The pH of a bromothymol blue (BMB) solution containing 4 g dm^{-3} of urease and 0.09 mol dm^{-3} of urea is measured. As the pH increases, a change from yellow to blue is observed. By taking an RGB histogram and converting to HSV, the change in hue angle, and by extension, colour, of the solution is tracked over the course of the experiment. A Boltzmann curve is fitted, where y = 245.84826 + (45.71295-245.84826)/(1 + exp((x-6.66741)/0.27339)).

Local pH changes were observed by placing a fibre embedded with 10 g dm^{-3} of urease into 20 cm^3 of saturated bromothymol blue solution containing 2 cm^3 of 1 mol dm^{-3} urea.

Gel beads were formed by dropping 5 wt. % solutions of sodium alginate containing 2 mg dm^{-3} bromothymol blue and either 0.008 g dm^{-3} or 10 g dm^{-3} of urease into a 0.1 mol dm^{-3} calcium chloride hexahydrate solution. The 0.008 g dm^{-3} urease beads were washed and placed into 20 cm^3 of distilled water containing 2 cm^3 of 1 mol dm^{-3} urea. The 10 g dm^{-3} urease beads were washed then placed into a 1 mol dm^{-3} urea solution. They were introduced to the 0.008 g dm^{-3} urease beads when required.

2.5 References

1 J. A. Loeser, *Nature*, 1939, **143**, 880–883.

2 E. Bonabeau, M. Dorigo and G. Theraulaz, *Nature*, 2000, **406**, 39–42.

3 J. B. Pollack and H. Lipson, *Nature*, 2000, **406**, 974–978.

4 M. Heisenberg, *Nature*, 2009, **459**, 164–165.

5 R. O. Doyle, *Nature*, 2009, **459**, 1052–1052.

6 P. Fratzl and F. G. Barth, *Nature*, 2009, **462**, 442–448.

7 D. Rus and M. T. Tolley, *Nature*, 2015, **521**, 467–475.

8 A. R. Morgan, A. B. Dawson, H. S. Mckenzie, T. S. Skelhon, R. Beanland, H. P. W. Franks and S. A. F. Bon, *Mater. Horiz.*, 2014, **1**, 65–68.

9 K. K. Dey, X. Zhao, B. M. Tansi, W. J. Méndez-Ortiz, U. M. Córdova-Figueroa, R. Golestanian and A. Sen, *Nano Lett.*, 2015, **15**, 8311–8315.

10 O. E. Shklyaev, H. Shum, A. Sen and A. C. Balazs, *Sci. Adv.*, 2016, **2**, e1501835.

11 C. Miesch and T. Emrick, *J. Colloid Interface Sci.*, 2014, **425**, 152–8.

12 R. W. Jaggers, R. Chen and S. A. F. Bon, *Mater. Horiz.*, 2016, **3**, 41–46.

13 F. Ahmed and D. E. Discher, *J. Control. Release*, 2004, **96**, 37–53.

14 S. Yu, T. Azzam, I. Rouiller and A. Eisenberg, *J. Am. Chem. Soc.*, 2009, **131**, 10557–10566.

15 K. T. Kim, J. J. L. M. Cornelissen, R. J. M. Nolte and J. C. M. van Hest, *Adv. Mater.*, 2009, **21**, 2787–2791.

16 M. A. C. Stuart, W. T. S. Huck, J. Genzer, M. Müller, C. Ober, M. Stamm, G. B. Sukhorukov, I. Szleifer, V. V. Tsukruk, M. Urban, F. Winnik, S.

Zauscher, I. Luzinov and S. Minko, *Nat. Mater.*, 2010, **9**, 101–113.

17 E. D'Elia, S. Eslava, M. Miranda, T. K. Georgiou and E. Saiz, *Sci. Rep.*, 2016, **6**, 25059.

18 T. Sun, G. Qing, B. Su and L. Jiang, *Chem. Soc. Rev.*, 2011, **40**, 2909–2921.

19 R. Yoshida, *Adv. Mater.*, 2010, **22**, 3463–83.

20 O. Kuksenok, P. Dayal, A. Bhattacharya, V. V. Yashin, D. Deb, I. C. Chen, K. J. Van Vliet and A. C. Balazs, *Chem. Soc. Rev.*, 2013, **42**, 7257.

21 S. Ogi, K. Sugiyasu, S. Manna, S. Samitsu and M. Takeuchi, *Nat. Chem.*, 2014, **6**, 188–195.

22 S. Ogi, T. Fukui, M. L. Jue, M. Takeuchi and K. Sugiyasu, *Angew. Chemie Int. Ed.*, 2014, **53**, 14363–14367.

23 E. Mattia and S. Otto, *Nat. Nanotechnol.*, 2015, **10**, 111–119.

24 A. E. Engelhart, K. P. Adamala and J. W. Szostak, *Nat. Chem.*, 2016, **8**, 448–453.

25 H. Ye, M. Daoud-El Baba, R.-W. Peng and M. Fussenegger, *Science*, 2011, **332**, 1565–1568.

26 X. He, M. Aizenberg, O. Kuksenok, L. D. Zarzar, A. Shastri, A. C. Balazs and J. Aizenberg, *Nature*, 2012, **487**, 214–218.

27 S. Debnath, S. Roy and R. V. Ulijn, *J. Am. Chem. Soc.*, 2013, **135**, 16789–16792.

28 T. Heuser, E. Weyandt and A. Walther, *Angew. Chem. Int. Ed. Engl.*, 2015, **54**, 13258–13262.

29 T. Heuser, A.-K. Steppert, C. Molano Lopez, B. Zhu and A. Walther, *Nano Lett.*, 2015, **15**, 2213–2219.

30 K. Y. Lee and D. J. Mooney, *Prog. Polym. Sci.*, 2012, **37**, 106–126.

31 F. Muzika, T. Bánsági, I. Schreiber, L. Schreiberová and A. F. Taylor, *Chem. Commun.*, 2014, **50**, 11107–11109.

32 G. Hu, J. A. Pojman, S. K. Scott, M. M. Wrobel and A. F. Taylor, *J. Phys. Chem. B*, 2010, **114**, 14059–14063.

33 Y. V. Griko, *Biophys. Chem.*, 1999, **79**, 117–127.

34 A. Hanbury, *Pattern Recognit. Lett.*, 2008, **29**, 494–500.

3 Temporal and spatial programming in soft composite hydrogel objects

This chapter details research published in the paper: R. W. Jaggers, and S. A. F. Bon, *J. Mater. Chem. B*, 2017, **5**, 7491-7495

3.1 Introduction

Soft, flexible and deformable structures are commonplace in nature, where evolution has developed elegant and efficient designs to accommodate a wide range of functions.[1] For many years, nature has inspired the creation of machines capable of 'life-like' tasks,[2] and these efforts have spawned the field of research known as *soft robotics*. This discipline seeks to create soft structures capable of adaptation, with a sensitivity and agility that can supersede mechanical, hard-bodied robots.[3,4]

Soft robots can have the ability to perform shape transformations,[5,6] for example, muscle like actuation,[7,8] or locomotion,[9–11] and can interact with their environments.[12,13] They are typically composed of hydrogels,[14,15] polymers[16,17], including elastomers,[18–20] and must be robust.[21,22] However, the majority of soft robots are still composed of both soft and rigid counterparts, the latter being required for power and control.[23,24]

A key challenge in this field is the design of entirely soft robots, in which responsive autonomous behaviour and function is built in and programmed. An impressive soft robotic system is the *octobot*, capable of the catalytic decomposition of an on-board fuel to power arm movement.[25] This example offers a soft analogue of the previously existing hardware version of itself, and shows that soft systems can be programmed to act in an autonomous, robotic fashion. Furthermore, large (millimetre scale) soft objects have been designed to interact with their environments, such as the soft-robotic ray that swims in response to a light

source,[26] the hydrogel actuator that walks in an electric field,[14] the tissue-engineered jellyfish that propels in an electric field,[27] and the sequentially self-folding shapes formed from shape memory polymers.[28]

Critically, a soft object of this nature should be capable of non-uniform, autonomous behaviour when provided with a fuel. Large soft objects need to be built in a way that their structures can vary, in order to introduce different functionalities into different parts of the object and allow for more complex behaviours, such as spatial or temporal programming.[29]

In this work, we show that soft hydrogel-based objects can be programmed to carry out non-uniform actions across their structures when exposed to a single fuel source, based on principles outlined in our previous work.[30] We demonstrate the temporal and spatial responsive nature of the soft bodies programmed by non-uniform distribution of the enzyme urease to introduce triggerable active zones in the otherwise dormant jelly. These active zones process the trigger fuel, urea, to create local pH gradients that alter the object's structure, as depicted in figure 3.1. In its simplest form (generation 1) we show a temporal and spatial colour change, associated with a local change in pH. The concept is then extended to control of material disintegration (generation 2).

3.2 Results and Discussion

Hydrogel objects are made from viscous aqueous solutions of the biopolymer sodium alginate, sourced from brown algae. Gels are easily formed upon exposure to Ca^{2+} (aq.).[30,31] Sodium alginate is used widely in the pharmaceutical and food industries due to its lack of toxicity and high biocompatibility,[32] and is a good candidate for building soft sustainable materials.[33] We used a templating strategy to fabricate centimetre-sized structures, typically a few millimetres thick.

Templates corresponding to the desired soft object shape were printed using a *FormLab* 2 SLA micro-stereolithographic printer. Aqueous sodium alginate

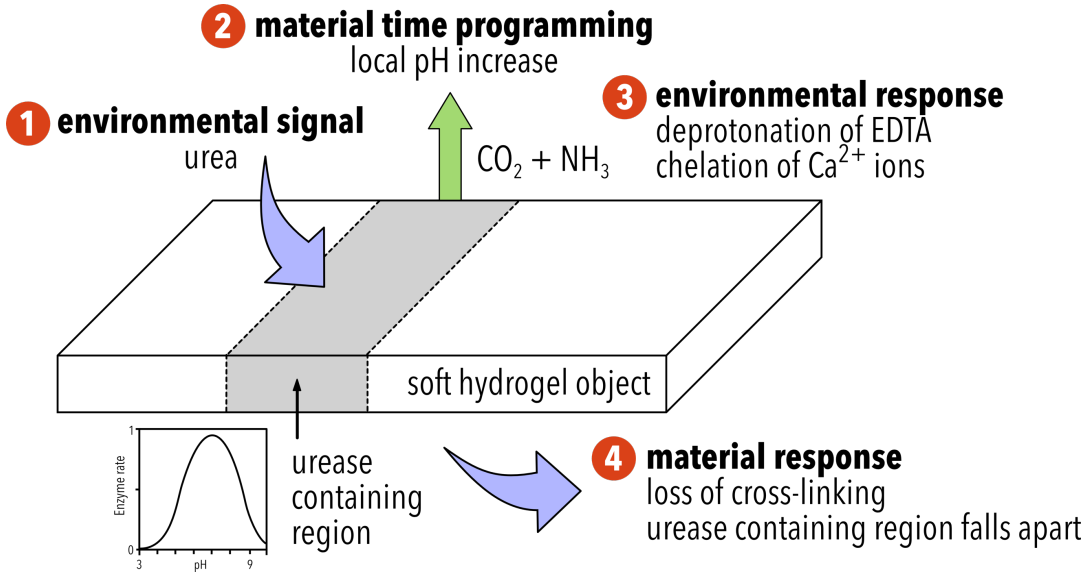

Figure 3.1 | Schematic describing the behaviour of ionically cross-linked hydrogel objects: (1) the semi-permeable soft object converts the fuel source, urea, to ammonia, due to the inclusion of urease in selected parts of its structure (2) after a defined period of time, urea containing regions of the object generate a local pH increase. Time-programming is possible due to the bell-shaped activity curve of urease, depicted in the figure[38] with an enzyme rate, $v' = (1 + 2 \times 10^{-9} / [H^+] + [H^+]/5 \times 10^{-6})^{-1}$ (3) partially protonated ethylenediaminetetraacetic acid (EDTA) is found in the low pH (3.50) environment. As the pH of the urease containing regions of the object increases, EDTA is locally deprotonated and chelates calcium ions from the hydrogel (4) loss of ionic cross-linking results in the disintegration and collapse of the urease containing regions.

formulations, termed 'pre-gels', were loaded manually into designated regions of the printed templates. These were immediately ionically cross-linked by spraying a liquid aerosol of calcium chloride solution onto them (see figure 3.2 for schematic).

The 'pre-gel' formulations used contained different ingredients such as coloured oil droplets and/or the pH indicator dye bromothymol blue (BMB), and specified amounts of the enzyme urease. Urease is introduced to these soft objects to spatially control pH over time. The enzyme is trapped inside the gel and does not migrate or diffuse (see figure 3.3).[34,35] Urease raises the pH by converting urea into

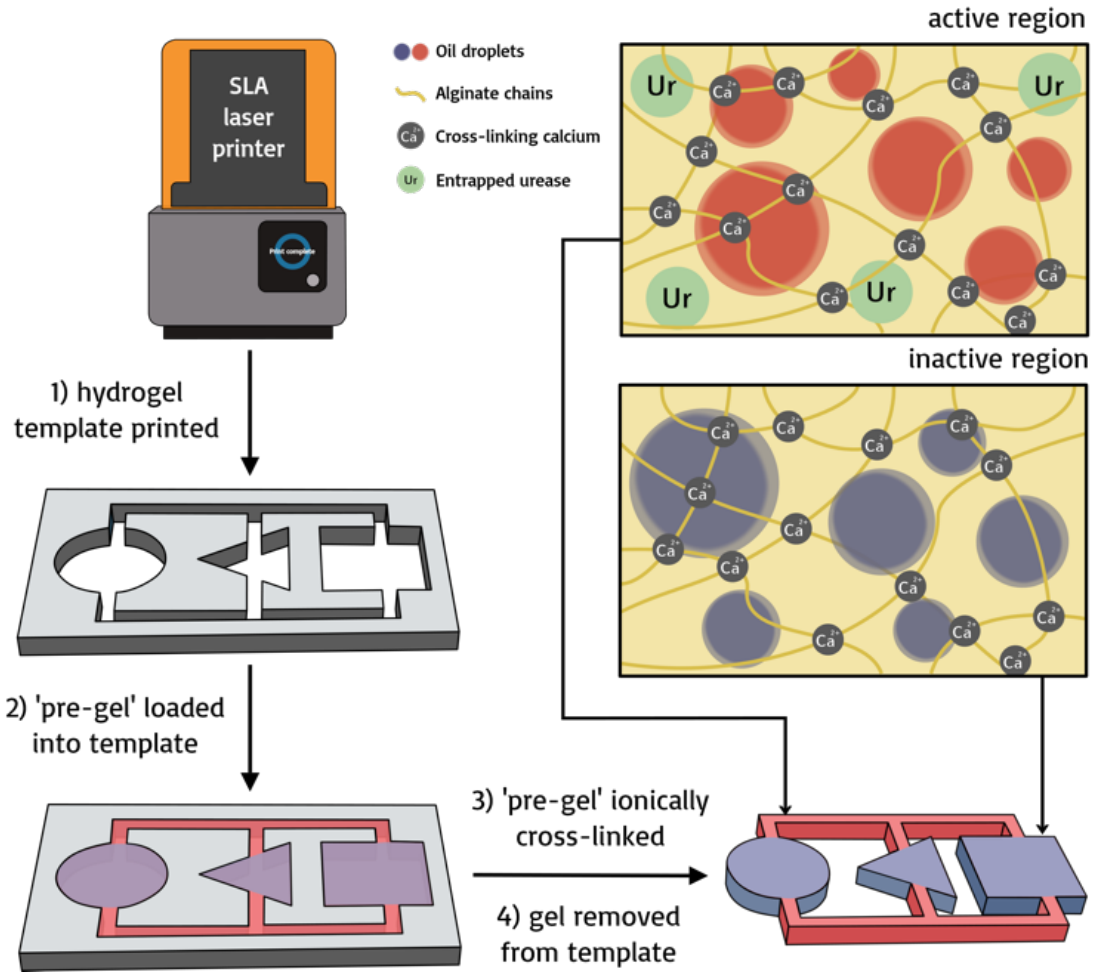

Figure 3.2 | Schematic depicting the synthesis of soft responsive objects. 1) The object template is designed and printed using computer aided desing (CAD) and a stereolithographic (SLA) laser printer 2) The 'pre-gel' is loaded into the template in the desired arrangement 3) the pre-gel is ionically cross-linked upon exposure to a 0.1 mol dm^{-3} aqueous solution of calcium chloride hexahydrate 4) following cross-linking, the soft object is removed from the template. Active regions contain the enzyme urease, whilst inactive regions do not.

ammonia and carbon dioxide, which we introduce as the trigger into the liquid environment in which the gels are placed.

The regional concentration of entrapped urease regulates the local increase in pH as a function of time. Time-programming is afforded due to the bell-shaped pH-activity curve of urease and its associated auto-catalytic behaviour. Low enzyme

activity is observed at low pH values; the generation of base elevates the pH into the higher activity window of the bell-shaped pH-activity curve, providing a positive feedback mechanism. As the initial increase in pH follows sigmoidal

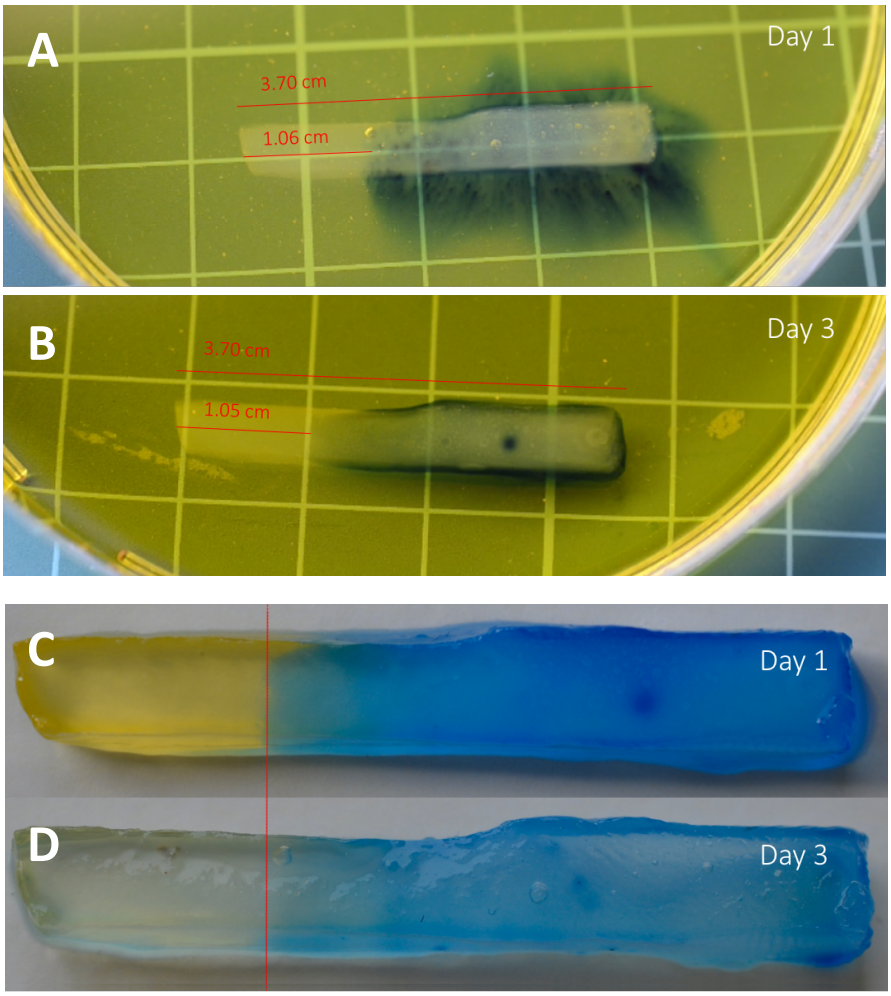

Figure 3.3 | Photographs of 1 wt. % calcium cross-linked alginate hydrogel objects containing urease at a concentration of 1 g dm^{-3} along approximately three quarters of its length. Photographs A and B show the hydrogel object, immersed in a saturated solution of the pH indicator bromothymol blue and 0.1 mol dm^{-3} urea, immediately after synthesis and 3 days later, respectively. A transition from yellow to blue indicates a pH higher than 7.6, and is therefore indicative of the location of urease (that is converting urea into ammonia and carbon dioxide). As images A and B show, the location of the urease appears to be approximately the same after 3 days, suggesting that the enzyme does not migrate through the hydrogel matrix. Images C and D are of the hydrogel objects removed from each of the solutions pictured in images A and B, respectively.

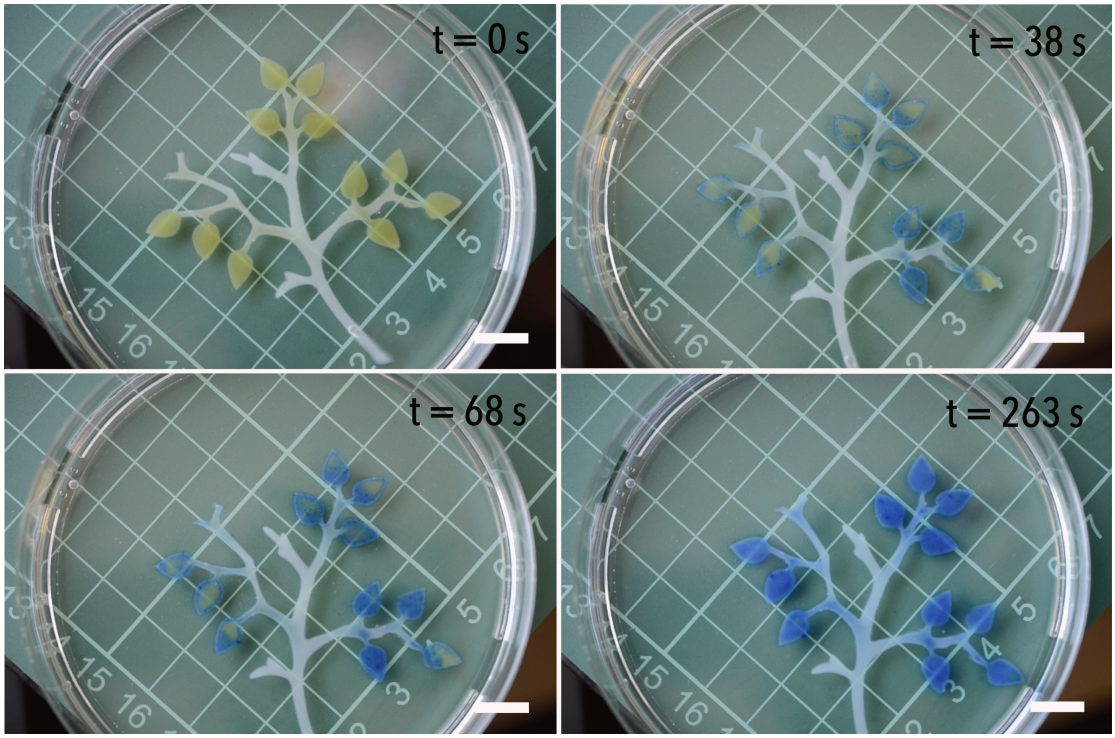

Figure 3.4 | A continuous soft object is formed from both inactive (white) regions that contain no urease, and active regions (coloured) that contain urease at a concentration of 20 g dm^{-3} and the pH indicator bromothymol blue. This object is placed in a bath of urea at a concentration of 0.45 mol dm^{-3}, at a pH of 3.5 (hence the yellow regions). Once the active regions have processed the urea into ammonia, the pH locally rises (above the indicating pH of 7.6) to produce a blue colour. See the supporting video that accompanies paper DOI:10.1039/C7TB02011B for the full sequence. Scale bar = 1 cm.

behaviour, the introduction of a dormancy period by variation of urease concentration is possible (see figure 3.1).

We will first discuss Generation 1 hydrogels where the temporal and spatial pH responses manifest themselves as colour changes.

When placed into acidic water of pH 3.5 in the presence of urea (0.45 mol dm^{-3}), a urease (20 g dm^{-3}) and pH indicator dye containing hydrogel, in the form of leaves on an inactive jelly tree, evidently generate a pH increase in excess of 7.6, as

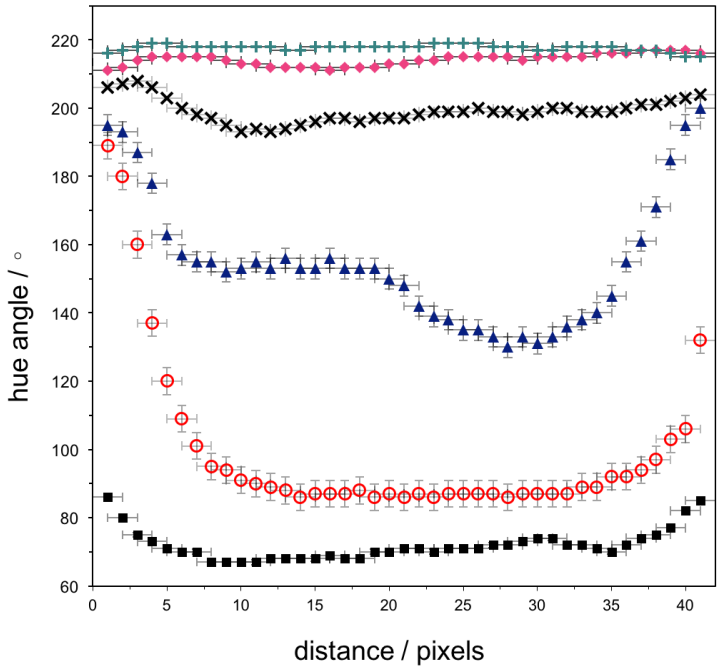

Figure 3.5 | An RGB line scan is taken across the width of the most left leaf at the following time intervals: t = 0 ■, t = 26 ○, t = 38 ▲, t = 68 ×, t = 136 ◆, and t = 263 +. From these, the hue angle is calculated (used as a numerical representation of colour, as discussed in chapter 2) and plotted against the distance of the line scan in the graph. This graph shows the change in colour across the width of the leaf. Square root error bars.

determined by the pH colorimetric indicator bromothymol blue (see figure 3.4 and the video that accompanies paper DOI:10.1039/C7TB02011B). We are able to quantify this change in colour by measuring the hue angle of the corresponding HSV histogram of a line scan from one of the leaves. The leaf starts with a hue angle of *ca.* 65°, corresponding to a yellow colour, and finishes with an angle of *ca.* 220°, that of the colour blue (N.B. the hue is the angle around the central vertical axis of an HSV cylindrical coordinate representation of a colour. The indicator bromothymol blue changes colour with pH, and as we are able to track this numerically, we are able to quantify its colour). As figure 3.5 shows, the colour change starts at the outside of the leaf and progresses inwards, as urea diffuses into the object. By comparing the hue angle over time at different points across this line scan, the change of colour over time is observed, as in figure 3.6. This curve is indicative of the pH increase over time generated by the activity of urease. As

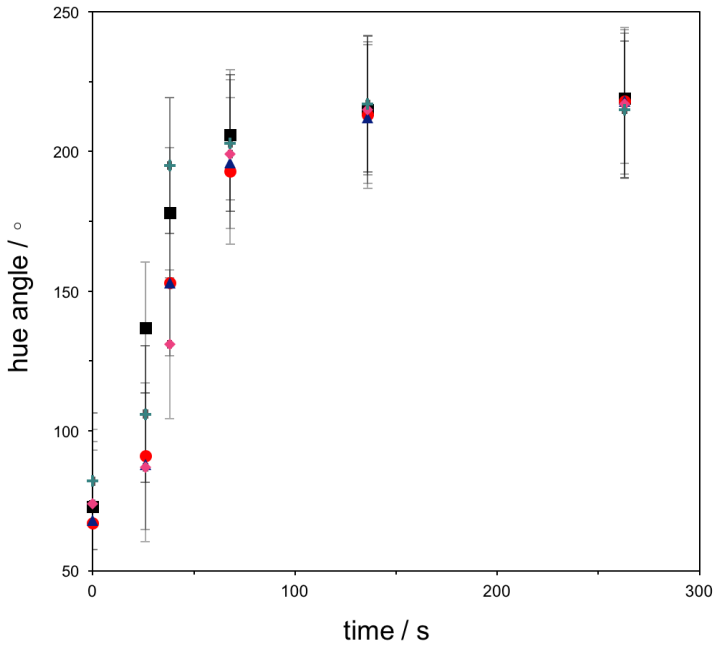

Figure 3.6 | Plotting the hue angle over time at selected locations across several line scans (at the pixel distances in figure 3.5 ■ = 4, ● = 10, ▲ = 18, ◆ = 30, and + = 40) produces the graph above. This graph depicts the change in colour of the leaf over time. Square root error bars.

figure 3.4 shows, this response is not only time programmed, but also spatially programmed. By having a non-uniform distribution of urease across the hydrogel structure, we are able to create a single, millimetre-sized soft object with anisotropic behaviour when exposed to a single stimulus.

In generation 2 systems, we utilise this temporal and spatial programming in the selective and coordinated disintegration of a hydrogel object (as described in figure 3.1), paired in some cases with the release of oil droplets. We achieve this by adding the sodium salt of ethylenediaminetetraacetic acid (EDTA) to the hydrogel environment as a chelating agent for calcium ions, acting as a dormant Ca^{2+}-sink. Objects are placed into an aqueous environment containing both EDTA and urea set at a pH value of 3.50. EDTA binds Ca^{2+} ions best at high pH, when all 6 of its donor groups (4 carboxylic acid groups and 2 nitrogens) are ionised. At a pH of 7.5, only a fraction of the EDTA is in this ionised form and its affinity for Ca^{2+} ions is reduced. As the pH is lowered further, the affinity of this chelator continues to decrease.[36] This was verified by placing enzyme loaded hydrogel objects into an

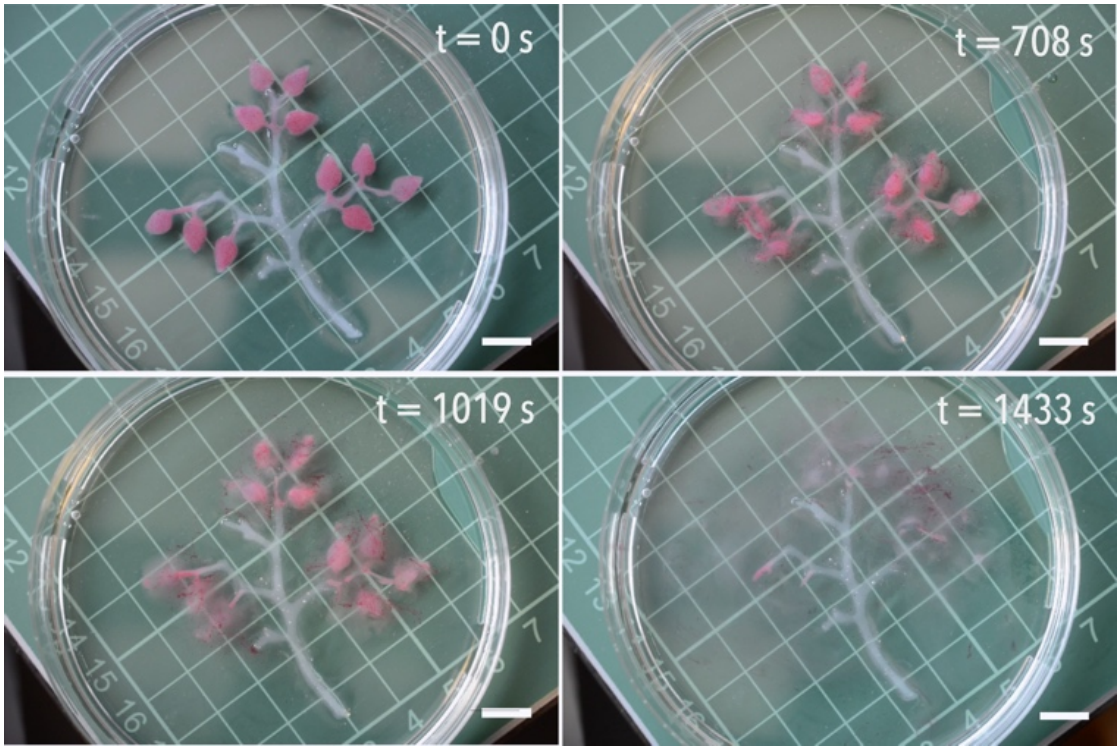

Figure 3.7 **|** A hydrogel tree is formed from an inactive branch structure (clear, no urease) and active leaves (red emulsified oil droplets, 20 g dm^{-3} urease). When immersed in an EDTA/urea environment (0.1 and 0.45 mol dm^{-3}, respectively) at pH 3.5, the leaves disintegrate to leave a naked tree branch due to local pH increases. See the supporting video that accompanies paper DOI:10.1039/C7TB02011B for the full sequence. Scale bar = 1 cm.

EDTA solution of pH 3.50 without urea. Without the ability to raise its pH, it remained intact over a period of at least 14 days. These ionically cross-linked objects are stable for months in the absence of EDTA. Upon a pH increase inside and in close proximity of the object (as a result of the programmed enzymatic reaction), EDTA transitions to its Ca^{2+} chelating form and thus promotes cation exchange. This results in the eventual disintegration of the alginate-gel matrix and subsequent release of any entrapped oil droplets.

To recap this system (also summarised in figure 3.1), the object converts urea, the fuel, to ammonia, due to the inclusion of urease in its structure. After a defined time period, dependent on the concentration of urease, the object generates a local increase in pH. Partially protonated ethylenediaminetetraacetic acid (EDTA) is

present in the low pH (3.50) environment. As the pH of the active sites on the hydrogel object increases locally, EDTA is deprotonated locally and chelation of calcium ions results in a loss of cross-linking and disintegration of the object, as well as the release of oil droplets if they are present.

Figure 3.7 (and the video that accompanies paper DOI:10.1039/C7TB02011B) demonstrates time and spatial programming in a millimetre-sized soft object that make use of this autonomous, enzyme-powered system when exposed to a fuel source of urea. A 5 wt. % alginate skeleton has 1 wt. % alginate leaves attached to it that contain a coloured emulsified oil (Oil Red O in vegetable oil) and urease at a concentration of 20 g dm^{-3}. Introduction to an EDTA and urea environment causes the leaves to disintegrate and 'fall off' the tree, thus decreasing the object's size and changing its shape. Disintegration of the leaves results in the release of the emulsified oil, the droplets of which are no longer stabilised once liberated from the alginate matrix. All 11 leaves start to disintegrate at the same time, marked by the release of oil droplets at 220 seconds, and all disappear at approximately the same time (see the video that accompanies paper DOI:10.1039/C7TB02011B). This design concept allows for the generation of a soft object that is programmed to change shape over time, thus allowing it to exist in more than one form during its lifetime. In this example, the enzyme concentration builds in a dormancy period prior to the objects transformation, the length of which is determined by the concentration of urease at a fixed concentration of urea. As a result, a single destabilisation event is observed for all regions containing a single urease concentration. If, however, a single object contains three distinct regions of different urease concentrations, it will respond at three pre-defined time intervals in response to one urea stimulus.

Figure 3.8 (and the video that accompanies paper DOI:10.1039/C7TB02011B) shows a composite gel object with regions that contain urease at a concentration of 20, 10 and 5 g dm^{-3}, and blue, red and yellow oil droplets, respectively. Following the introduction of the object to an EDTA and urea environment, the object sequentially disintegrates region by region. At 160 seconds, the first segment,

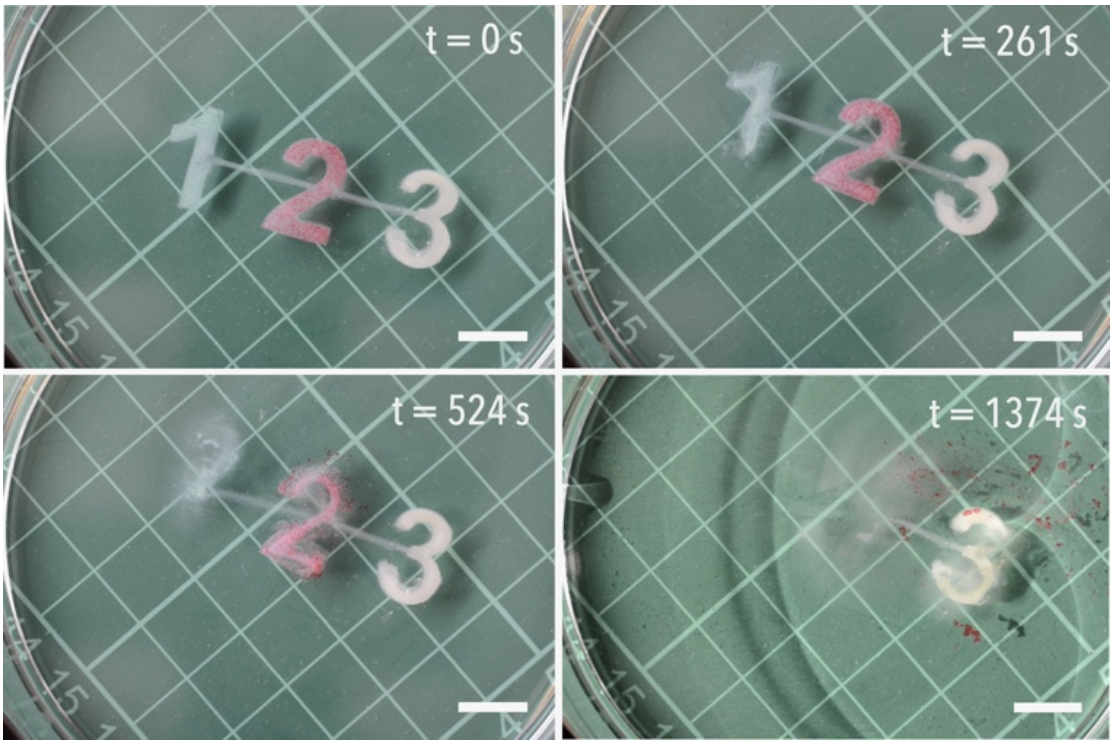

Figure 3.8 | A continuous soft object containing three distinct regions of different enzyme concentrations is immersed in an EDTA/urea environment (0.1 and 0.45 mol dm^{-3}, respectively) at pH 3.5. Due to local pH increases, segment 1 containing emulsified blue oil droplets and 20 g dm^{-3} urease, disintegrates first, followed by segment 2 that contains emulsified red oil droplets and 10 g dm^{-3} urease, and then segment 3 that contains emulsified yellow oil droplets and 5 g dm^{-3} urease. See the supporting video that accompanies paper DOI:10.1039/C7TB02011B for the full sequence. Scale bar = 1 cm.

containing 20 g dm^{-3} urease, starts to disintegrate. This is followed by the second segment, containing 10 g dm^{-3} urease, at 300 seconds, and finally the third segment, containing 5 g dm^{-3} urease, at 780 seconds. These three segments have fully disintegrated after 550, 1110, and 4140 seconds, respectively, releasing their oil droplets in the process. Reducing the urease concentration both increases the dormancy period before material decomposition and the length of the decomposition time for a given region in the object. This clearly demonstrates that one object can be programmed to exhibit three distinct responses with both spatial and temporal programming.

3.3 Conclusions

In conclusion, we demonstrate the design and fabrication of continuous soft hydrogel objects that are programmed to spatially and temporally respond to the environmental cue of a fuel source, urea. The enzyme urease provides the objects with in-built time-programming, allowing the objects to produce their own local pH fields after pre-defined time periods by means of varied enzyme concentrations. By controlling the distribution of the enzyme urease across the body of the object, regions of the object selectively disintegrate upon activation of the enzyme. This results in an object with autonomous control over its response to an environmental stimulus. Such a material is valuable in the design and fabrication of entirely soft robots, offering a way to selectively build responsive characteristics into entirely soft objects.

3.4 Experimental methods

3.4.1 Materials

Alginic acid sodium salt (*syn.* sodium alginate) from brown algae, urease from *Canavalia ensiformis* (Jack bean) type IX powder, 500,000 units/g solid, calcium chloride hexahydrate (98%), oil blue N (96%), oil red O and urea (powdered, ≥ 98%) was purchased from Sigma Aldrich. Ethylenediaminetetraacetic acid (EDTA, 99%), ethanol (absolute, analytical grade) and hydrochloric acid (37%) was purchased from VWR international. Vegetable oil was purchased from Costcutters Ltd. Bromothymol blue, ACS reagent, was purchased from Fisher Scientific. Oleoresin paprika oil 80,000 NS was purchased from Kalsec. Span 80 was purchased from Fluka.

3.4.2 Gel templates

Templates corresponding to the desired hydrogel shapes were created in the software package *123 Design* (see figure 3.9). These were uploaded into the software

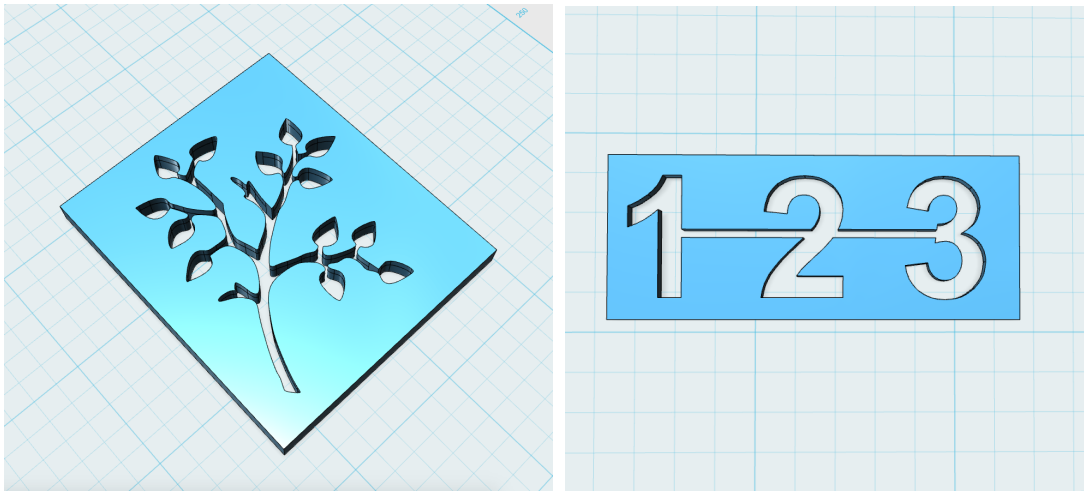

Figure 3.9 | 3D drawings created in *123 Design* that were printed on the *Formlab* 2 SLA printer; the hydrogel tree (left) and 1-2-3 object (right) are shown.

package *PreForm* and printed into 3D polymer objects using the FormLab 2 SLA printer (grey resin GPGR03). Polymer templates were washed in ethanol for 20 minutes to remove residual monomer, then post-cured under a UV lamp (365 nm) for 30 minutes. The bottom faces of the gel templates were coated with a thin layer of silicone grease (to keep the template water tight) and placed onto a flat silicone surface.

3.4.3 'Pre-gel' formulation

Solutions of sodium alginate were prepared by dissolving dry powders of alginic acid sodium salt into deionised water at either 1 or 5 wt. %. Active regions of the material were created by dissolving the enzyme urease into 1 % sodium alginate solutions at a concentration of either 5, 10 or 20 mg cm^{-3}. Coloured regions of the gel were created by emulsifying an enzyme loaded 1 wt. % alginate solution with vegetable oil (containing 1 mg cm^{-3} of either oil blue N, oil red O or paprika oil), using 1 mg cm^{-3} of the surfactant Span 80 (enough to stabilise the emulsion for *ca.* 10 minutes). In the case of the pH indicator experiments, the 'pre-gel' solutions contained 1 mg cm^{-3} of the dye bromothymol blue. These 'pre-gels' are loaded into the templates in the desired combination prior to gelation.

3.4.4 Gel cross-linking

Pre-gel loaded templates are exposed to a fine jet spray of 0.1 mol dm^{-3} calcium chloride solution to induce ionic cross-linking of the alginate polymer chains by calcium ions. After several jet sprays, the gel surface is covered in a further 2 cm^3 of 0.1 mol dm^{-3} calcium chloride and left to fully cross-link for 20 minutes. Following this, the template was removed and the object rinsed with deionised water to remove residual calcium chloride.

3.4.5 Object behaviour

The composite gel objects were placed into a petri dish containing 20 cm^3 of 0.1 mol dm^{-3} EDTA and 2 cm^3 of 5 mol dm^{-3} urea solution. Their behaviour was filmed using a Nikon D5100 camera equipped with a AF-S Micro Nikkor 40 mm 1:2.8 G lens. Still images are taken from these videos where appropriate.

3.4.6 Colour quantification

The hydrogel leaf on the far left of figure 2 was analysed using *ImageJ (Fiji)* to collect an RGB histogram of the pixels that make up a line scan across its width. These RGB coordinates were converted into HSV values, from which the reported hue angles were taken.[37] See further details in the discussion section of chapter 2.

3.5 References

1 M. H. Dickinson, C. T. Farley, R. J. Full, M. A. R. Koehl, R. Kram and S. Lehman, *Science*, 2000, **288**, 100–106.

2 A. W. Feinberg, *Annu. Rev. Biomed. Eng.*, 2015, **17**, 243–265.

3 D. Rus and M. T. Tolley, *Nature*, 2015, **521**, 467–475.

4 S. Kim, C. Laschi and B. Trimmer, *Trends Biotechnol.*, 2013, **31**, 287–294.

5 A. D. Marchese, R. Tedrake and D. Rus, *Int. J. Robot. Res.*, 2016, **35**, 1000–1019.

6 B. Mazzolai, L. Margheri, M. Cianchetti, P. Dario and C. Laschi, *Bioinspir. Biomim.*, 2012, **7**, 25005.

7 M. Cianchetti, M. Calisti, L. Margheri, M. Kuba and C. Laschi, *Bioinspir. Biomim.*, 2015, **10**, 35003.

8 A. Wang, H. Yu and S. Cang, *J. Franklin Inst.*, 2017, **354**, 1759–1783.

9 M. T. Tolley, R. F. Shepherd, B. Mosadegh, K. C. Galloway, M. Wehner, M. Karpelson, R. J. Wood and G. M. Whitesides, *Soft Robot.*, 2014, **1**, 213–223.

10 A. D. Marchese, C. D. Onal and D. Rus, *Soft Robot.*, 2014, **1**, 75–87.

11 C. D. Onal and D. Rus, *Bioinspir. Biomim.*, 2013, **8**, 26003.

12 D. Han, H. Gu, J. Kim and S. Yokota, *Sensors Actuators A Phys.*, 2017, **257**, 47–57.

13 H. Jin, E. Dong, M. Xu, C. Liu, G. Alici and Y. Jie, *Smart Mater. Struct.*, 2016, **25**, 85026.

14 D. Morales, E. Palleau, M. D. Dickey and O. D. Velev, *Soft Matter*, 2014, **10**, 1337–1348.

15 L. Ionov, *Adv. Funct. Mater.*, 2013, **23**, 4555–4570.

16 I. A. Anderson, T. A. Gisby, T. G. McKay, B. M. O'Brien and E. P. Calius, *J. Appl. Phys.*, 2012, **112**, 41101.

17 A. Argiolas, B. C. Mac Murray, I. Van Meerbeek, J. Whitehead, E. Sinibaldi, B. Mazzolai and R. F. Shepherd, *Soft Robot.*, 2016, **3**, 101–108.

18 H.-T. Lin, G. G. Leisk and B. Trimmer, *Bioinspir. Biomim.*, 2011, **6**, 26007.

19 C. Larson, B. Peele, S. Li, S. Robinson, M. Totaro, L. Beccai, B. Mazzolai and R. Shepherd, *Science*, 2016, **351**, 1071–1074.

20 D. Hughes and N. Correll, *Bioinspir. Biomim.*, 2015, **10**, 55002.

21 C. Lee, M. Kim, Y. J. Kim, N. Hong, S. Ryu, H. J. Kim and S. Kim, *Int. J. Control. Autom. Syst.*, 2017, **15**, 3–15.

22 K. Suzumori, *Rob. Auton. Syst.*, 1996, **18**, 135–140.

23 K. B. Shimoga and A. A. Goldenberg, *Proc. IEEE Int. Conf. Robot. Autom.*, 1992, 1300–1305.

24 S. W. Kwok, S. A. Morin, B. Mosadegh, J.-H. So, R. F. Shepherd, R. V. Martinez, B. Smith, F. C. Simeone, A. A. Stokes and G. M. Whitesides,

Adv. Funct. Mater., 2014, **24**, 2180–2187.

25 M. Boncheva, S. A. Andreev, L. Mahadevan, A. Winkleman, D. R. Reichman, M. G. Prentiss, S. Whitesides and G. M. Whitesides, *Proc. Natl. Acad. Sci.*, 2005, **102**, 3924–3929.

26 S.-J. Park, M. Gazzola, K. S. Park, S. Park, V. Di Santo, E. L. Blevins, J. U. Lind, P. H. Campbell, S. Dauth, A. K. Capulli, F. S. Pasqualini, S. Ahn, A. Cho, H. Yuan, B. M. Maoz, R. Vijaykumar, J.-W. Choi, K. Deisseroth, G. V. Lauder, L. Mahadevan and K. K. Parker, *Science*, 2016, **353**, 158–162.

27 J. C. Nawroth, H. Lee, A. W. Feinberg, M. L. Ripplinger, L. M. McCain, A. Grosberg, J. O. Dabiri and K. K. Parker, *Nat. Biotechnol.*, 2012, **30**, 792–797.

28 Y. Mao, K. Yu, M. S. Isakov, J. Wu, M. L. Dunn and H. Jerry Qi, *Sci. Rep.*, 2015, **5**, 13616.

29 X. He, J. Fan, J. Zou and K. L. Wooley, *Chem. Commun.*, 2016, **52**, 8455–8458.

30 R. W. Jaggers and S. A. F. Bon, *Mater. Horiz.*, 2017, **4**, 402–407.

31 A. Johnson and J. B. Speakman, *J. Soc. Dye. Colour.*, 1946, **62**, 97–100.

32 K. Y. Lee and D. J. Mooney, *Prog. Polym. Sci.*, 2012, **37**, 106–126.

33 M. Szekalska, A. Puciłowska, E. Szymańska, P. Ciosek and K. Winnicka, *Int. J. Polym. Sci.*, 2016, **2016**, 1–17.

34 A. R. DeGroot and R. J. Neufeld, *Enzyme Microb. Technol.*, 2001, **29**, 321–327.

35 N. Das, A. M. Kayastha and O. P. Malhotra, *Biotechnol. Appl. Biochem.*, 1998, **27**, 25–9.

36 Y. V. Griko, *Biophys. Chem.*, 1999, **79**, 117–127.

37 A. Hanbury, *Pattern Recognit. Lett.*, 2008, **29**, 494–500.

38 G. Hu, J. A. Pojman, S. K. Scott, M. M. Wrobel and A. F. Taylor, *J. Phys. Chem. B*, 2010, **114**, 14059–14063.

4 Communication between hydrogel beads via chemical signalling

This chapter details research published in the paper: R. W. Jaggers, and S. A. F. Bon, *J. Mater. Chem. B*, 2017, **5**, 8681-8685

4.1 Introduction

Communication is a significant capability of living organisms. Human beings actively communicate with each other on a physical basis, such as visually,[1] audibly,[2] or by touch.[3]

The most primitive and arguably most important form of information exchange, which also underpins the above, is chemical communication.[4,5] Living organisms rely on this method of signal transduction, such as plants,[6] vertebrates,[7] and insects,[8] as do biological cells and microorganisms.[9]

Biological cells can communicate with one another by exchange of chemical signals, in the form of secreted signalling molecules, such as hormones, neurotransmitters or ions.[10] These molecules can be detected by receptors of a target cell that can subsequently trigger a response.[11,12] Furthermore, simple microorganisms such as the amoeba release chemical signals to induce self-assembly of individuals into multi-cellular colonies, allowing for collective motion.[13,14] It is theorised that protocells (the earliest versions of modern day cells)[15] communicated by such elementary chemical signalling, in the absence of complicated biochemical machinery.[14]

Man-made materials have been proposed and designed in an effort to mimic communication in and between organisms. The ability to exchange information by means of chemical signal transduction has been demonstrated computationally, for example gels and microcapsules that undergo communication and auto-

chemotaxis,[14,16–19] vesicles that communicate through nanotubes,[20] and microcapsules that self-assemble.[21]

A number of interesting studies have demonstrated that this kind of communication between synthetic objects is indeed realistic. Sen and co-workers showed that silica particles flock around photo-active silver chloride colloids in water, which themselves show schooling behaviour. The swarming phenomenon is induced by localised electrolyte gradients established through secretion of ions.[22] Giménez *et al.* designed capped silica nanoparticles that can send hierarchical messages, such that a chemical signal opens a gate that allows for a secondary signal to be sent.[23] Furthermore, communication mediated cargo delivery, where Janus nanoparticles must interchange chemical messengers in order to open a series of gates, has been demonstrated.[4]

Moving away from nanoscale dimensions, communication between an interconnected network of giant vesicles has been demonstrated by Orwar and coworkers.[24,25] The lumina of vesicles, connected by nanotubes, are able to exchange material by their interconnecting bridges. Recently, Mansy *et al.* elegantly designed artificial cells which have the ability to sense and synthesise quorum signalling molecules, allowing for chemical communication with a range of bacteria.[26]

At a macroscopic length scale, the oscillatory, non-equilibrium Belousov–Zhabotinsky (BZ) reaction has been used to propagate chemical waves across a series of hydrogel objects, thus enabling them to pass on a signal.[27,28]

In this work, we demonstrate that millimetre-sized, soft hydrogel objects containing different signalling and receiving molecules, can communicate by exchange of chemical signals when placed in proximity to each other in an aqueous environment. Simple chemical and biological tools are used to allow for communication to operate in short timescales (seconds to minutes). Beads encapsulating one of three species, namely the enzyme urease, the enzyme

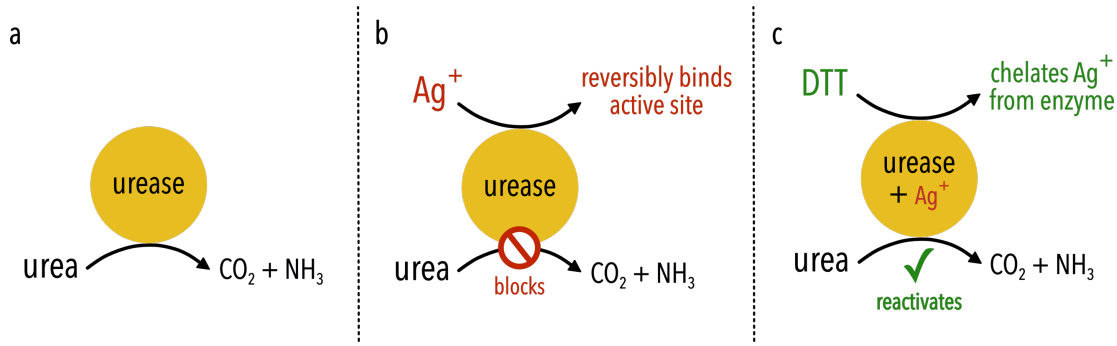

Figure 4.1 | The three modes of action of a urease loaded hydrogel bead (a) when exposed to an acidic aqueous solution of urea, a bead containing urease generates carbon dioxide and ammonia within its core and in its surrounding environment (b) if a 'urease' bead is exposed to aqueous silver ions (Ag^+), the ions reversibly bind to the enzyme active site and inhibit it. The bead can no longer produce carbon dioxide or ammonia (c) if a silver bound 'urease' bead is exposed to dithiothreitol (DTT), Ag^+ ions can be chelated from the enzyme and thus reactivate it, allowing it to produce carbon dioxide and ammonia once again.

inhibitor silver (Ag^+), and the Ag^+ chelator dithiothreitol (DTT), are shown to interact when placed in contact with one another (see figure 4.1). By exploiting the interplay between the enzyme, its reversible inhibitor, and this inhibitor's chelator, we demonstrate a series of 'conversations' between the beads, following the release of encapsulated Ag^+ and DTT into the surrounding solution and adjacent beads.

These communicating beads are an original example of chemically mediated signalling between mixed soft artificial objects, and provides insight into the design of biomimetic materials that are able to communicate without continuous external input.

4.2 Results and Discussion

Hydrogel beads are formed from aqueous solutions of the biopolymer sodium alginate, and are formed by depositing the solution from a pipette tip into a 0.1 mol dm^{-3} aqueous solution of calcium chloride hexahydrate or calcium hydroxide.

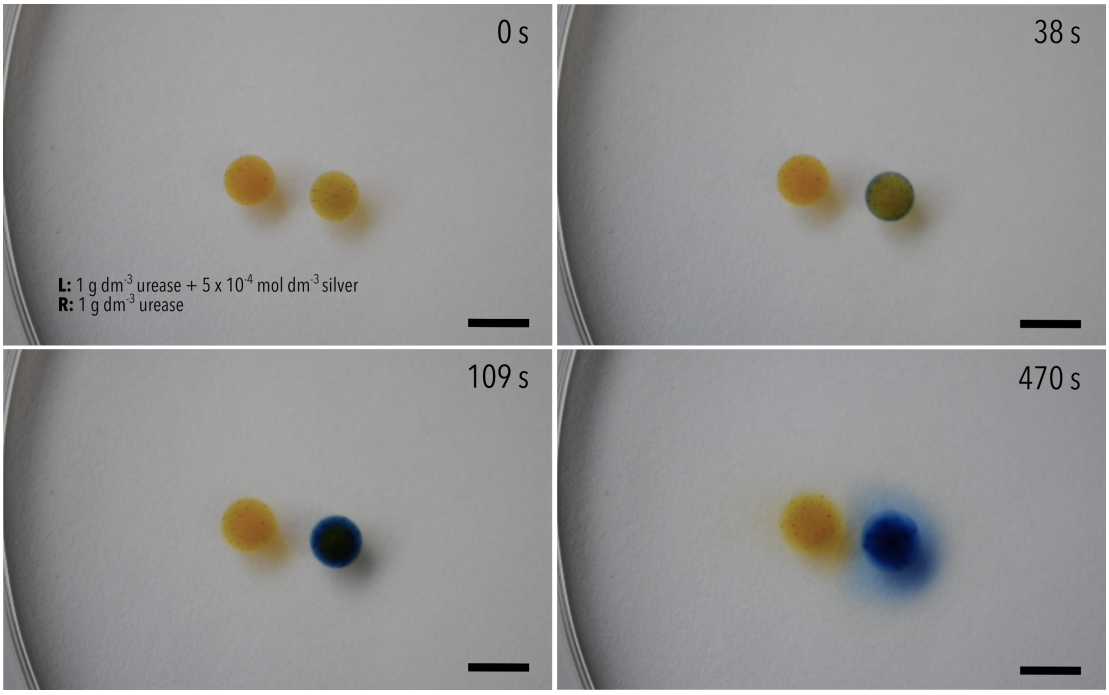

Figure 4.2 | Two beads are immersed in a 0.1 mol dm^{-3} solution of urea; the left bead contains urease at a concentration of 1 g dm^{-3} and silver nitrate at a concentration of 5 x 10^{-4} mol dm^{-3}, and the right contains urease at a concentration of 1 g dm^{-3} only. After 25 seconds, the bead containing only urease increases in pH past a value of 7.6, signified by a change in colour of the pH indicator bromothymol blue from yellow to blue. The bead containing Ag^{+} ions does not undergo this pH and colour change. Scale bar = 5 mm. See the video that accompanies the paper for full sequence.

The desired components, either urease, silver cations or DTT, are dissolved into the alginate solution prior to deposition, along with the colorimetric pH indicator bromothymol blue. Acetic acid is used to adjust the pH to 3.5 for both the alginate and the calcium ion solutions. The beads reside in the calcium solutions for only a few minutes, resulting in a solid cross-linked shell and a liquid core (see experimental methods for the full protocol). As a monitoring tool in our study, we focus on the colorimetric behaviour of an 'enzyme' bead. This alginate hydrogel bead is loaded with the enzyme urease at a concentration of 1 g dm^{-3}, which is entrapped in the bead and cannot leave.[29,30] Upon exposure to a 0.1 mol dm^{-3} aqueous solution of urea (also corrected to pH 3.5), the urease generates carbon

dioxide and ammonia, thus increasing the pH in the bead and its immediate local area (see figure 4.1, a). Inclusion of the colorimetric pH indicator bromothymol blue within the bead allows us to visualise this change that manifests as a transition from yellow to dark blue when a pH of 7.6 is surpassed (see figure 4.2, right bead). This colour change happens after a defined time period, in this case after 25 seconds. Note that the dormancy period can be tailored by variation of the enzyme concentration. A lower concentration of urease results in an increased delay before pH increase, and thus colour change from yellow to blue thanks to the bell-shaped pH activity curve for this enzyme (see our previous study, and chapters 2 and 3, for further information about this time programming).[31,32]

The first communication tool we employ is the deactivation of urease using silver ions (Ag^+).[33,34]

Silver (as well as other heavy metal) ions are able to reversibly bind with the active site of urease, deactivating it, and thus halting its production of carbon dioxide and ammonia (see figure 4.1, b).[35] This means that a urease containing bead introduced to silver ions, in the form of an aqueous silver nitrate solution, is unable to undergo a pH increase when exposed to a solution of urea. We checked this by preparing a bead which contained both urease at a concentration of 1 g dm^{-3} (identical to its active partner beside it) and silver ions at a concentration of 5 x 10^{-4} mol dm^{-3}. Its behaviour is compared with the 'enzyme' bead (see figure 4.2). The presence of silver ions in the left bead halts the production of ammonia and prevents a colour change, thus acting as an 'off' switch.

This interplay between urease and silver can be used as a tool for communication between two gel beads. If a bead containing urease sits next to a bead containing silver nitrate, silver ions diffuse from the 'silver' bead into the 'enzyme' bead. This will lead to local deactivation of urease and thus the switching off of the colour change. Figures 4.3, 4.4 and 4.5 displays three scenarios a, b, and c, in which the concentration of entrapped enzyme is varied, this being 1, 0.25 and 0.125 g dm^{-3}, respectively. Each experiment contains three beads aligned. In scenarios a and c,

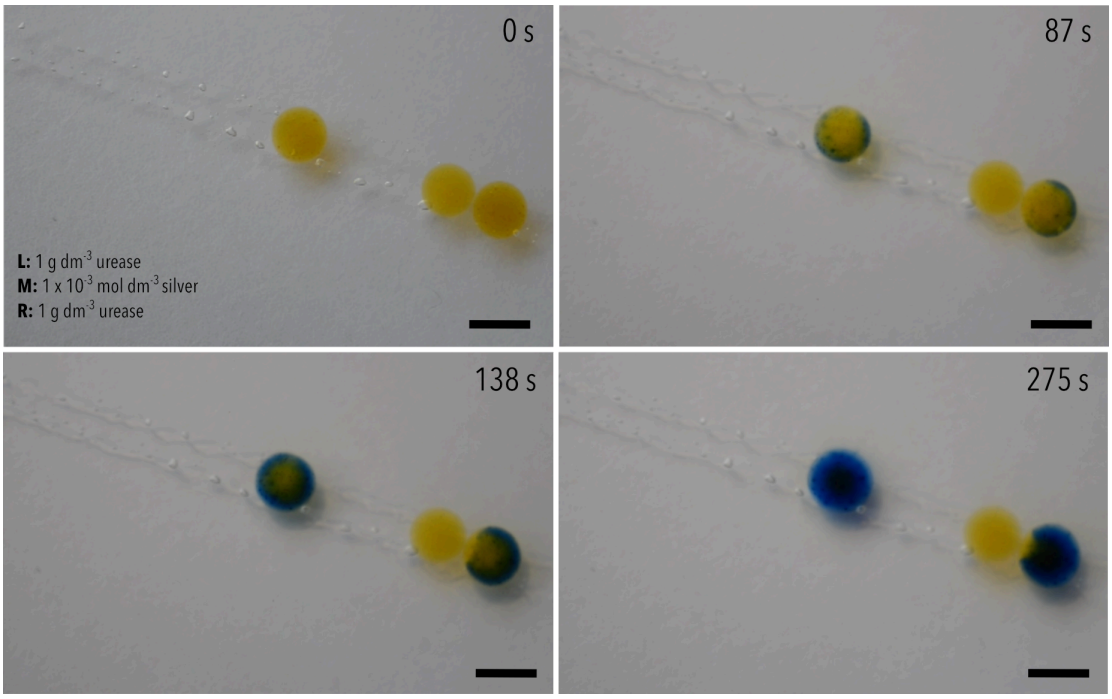

Figure 4.3 | When a urease containing bead is placed next to a bead containing 1 x 10^{-3} mol dm^{-3} silver ions in a 0.1 mol dm^{-3} solution of urea, it is either partially or fully inhibited, depending on the concentration of urease in the bead. In this case, at an enzyme concentration of 1 g dm^{-3}, contact with the 'silver' bead prevents a small region of the bead from increasing in pH and thus it remains yellow, this region being the contact point between the 2 beads. The rest of the bead is, however, able to increase in pH in the same fashion as its uninfluenced neighbour to the left (the onset of colour change to blue occurring at 38 seconds). Scale bar = 5 mm. See the video that accompanies the paper for full sequence.

the outer two (left and right) are 'enzyme' beads and the middle bead contains silver at a concentration of 1 x 10^{-3} mol dm^{-3}. This 'silver' bead is placed in direct contact with the right hand 'enzyme' bead. In scenario b, the left and middle beads are 'enzyme' beads, whilst the right-hand bead is 'silver'.

In each case, the bead on the left transitions from yellow to blue indicating an increase in pH, and the time taken for this to happen increases with a decreasing enzyme concentration. For a 1 g dm^{-3} bead, the onset of colour change is at 38 seconds, for a 0.25 g dm^{-3} bead it is at 82 seconds, and for a 0.125 g dm^{-3} bead it

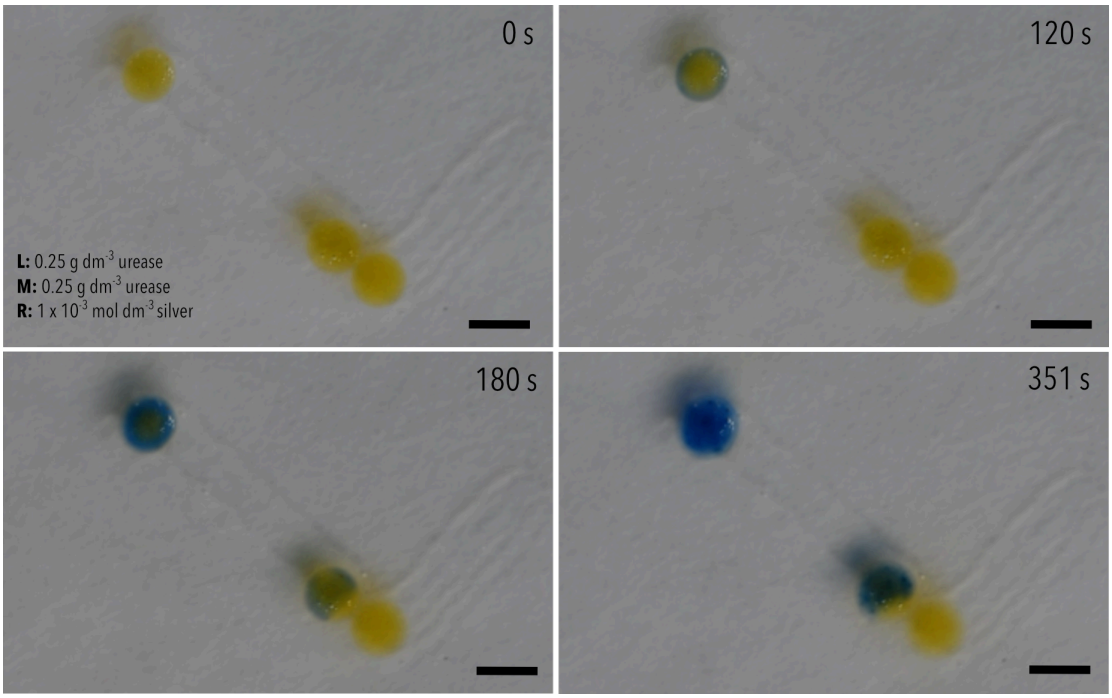

Figure 4.4 | When a urease containing bead is placed next to a bead containing 1 x 10^{-3} mol dm^{-3} silver ions in a 0.1 mol dm^{-3} solution of urea, it is either partially or fully inhibited, depending on the concentration of urease in the bead. When the enzyme concentration in the beads is lowered to 0.25 g dm^{-3}, a similar behaviour is observed to that of figure 4.3, however the yellow region at the contact point is widened, such that a large portion of the enzyme bead remains at low pH after 351 seconds. The uninfluenced bead transitions to high pH and blue at 82 seconds. Scale bar = 5 mm. See the video that accompanies the paper for full sequence.

is at 218 seconds. The right 'enzyme' bead, however, displays a different behaviour, on account of its interaction with the 'silver' bead.

In the case of an enzyme concentration of 1 g dm^{-3} (scenario a, figure 4.3), contact with the 'silver' bead deactivates a small region of the 'enzyme' bead hereby arresting its colour change. This region is in proximity to the contact point between the two beads. The majority of the bead remains enzymatically active, however, and thus able to undergo the colour transition from yellow to blue.

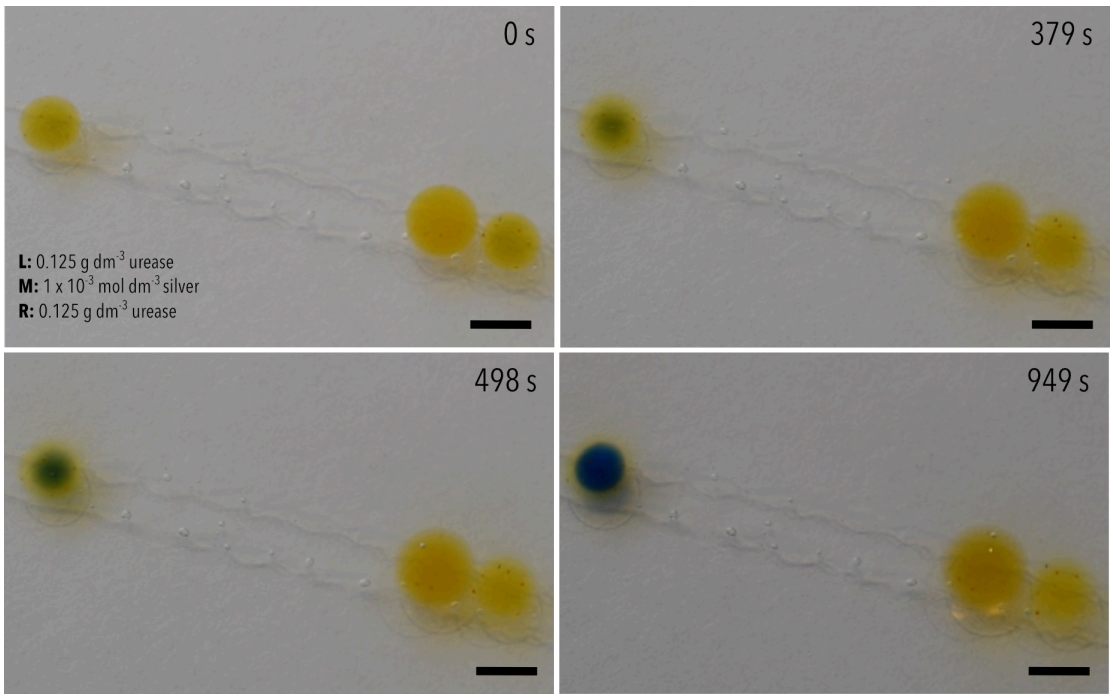

Figure 4.5 | When a urease containing bead is placed next to a bead containing 1 x 10^{-3} mol dm^{-3} silver ions in a 0.1 mol dm^{-3} solution of urea, it is either partially or fully inhibited, depending on the concentration of urease in the bead. When the enzyme concentration is lowered further to 0.125 g dm^{-3}, this yellow region is extended fully across the entire 'enzyme' bead, remaining after 949 seconds. The uninfluenced bead transitions to high pH and blue at 218 seconds. Scale bar = 5 mm. See the video that accompanies the paper for full sequence.

When the enzyme concentration in the beads is lowered to 0.25 g dm^{-3} (scenario b, figure 4.4) a similar behaviour is observed. Note that we exchanged the two beads, so now the 'silver' bead is on the outer right. The yellow region at the contact point is widened, such that a larger portion of the 'enzyme' bead remains at low pH (and thus yellow) after 351 seconds. When the enzyme concentration is lowered further to 0.125 g dm^{-3} (scenario c, figure 4.5), this yellow region is extended fully across the entire 'enzyme' bead, and remains yellow after 949 seconds.

From these observations, we deduce that the silver ions loaded into the 'silver' bead are able to diffuse into the 'enzyme' bead with which they make contact but not with the 'enzyme' bead found further afield. The different responses of the

'enzyme' beads to this influx of silver ions is explained by the time-delayed behaviour of the urease.

The concentration of silver used, here 1 x 10^{-3} mol dm^{-3}, far exceeds that of the amount needed to deactivate each urease molecule. In scenario a, figure 4.3, *ca.* 1.8 x 10^{-6} mol dm^{-3} of urease was present (at 545 kDa). We therefore postulate that the enzymatic reaction at higher enzyme loadings generates a sufficiently high flux to influence the diffusional flow profile of the silver ions, hindering bead penetration. When the enzyme concentration is low, this counter flux caused by the enzymatic reaction is too low to stop complete penetration of the silver ions, hereby deactivating the 'enzyme' bead fully.

The second communication tool we employ is the reactivation of urease by chelating the bound silver ions with dithiothreitol (DTT), see figure 4.1, c.[36,37]

When a bead containing both urease, at a concentration of 5 g dm^{-3}, and silver cations, at a concentration of 2 x 10^{-4} mol dm^{-3}, is immersed in a 0.1 mol dm^{-3} solution of urea, no pH increase is observed (left bead in figure 4.6, confirming figure 4.2). If an identical bead makes contact with one containing 0.52 mol dm^{-3} DTT, the encapsulated DTT diffuses into the silver-deactivated 'enzyme' bead. This results in the chelation of silver ions from the urease and thus its reactivation. This is visualised on the right-hand side of figure 4.6, where the 'DTT' bead (far-right) makes contact with a silver-bound 'urease' bead (centre), inducing a transition from yellow to blue. This quite clearly shows that DTT can act as an 'on' switch to a previously deactivated 'urease' bead, and that the 'urease' bead receives a chemical signal from the 'DTT' bead.

In the final communication scenario shown in figure 4.7, our two switches are used in unison to create a trio of communicating beads.

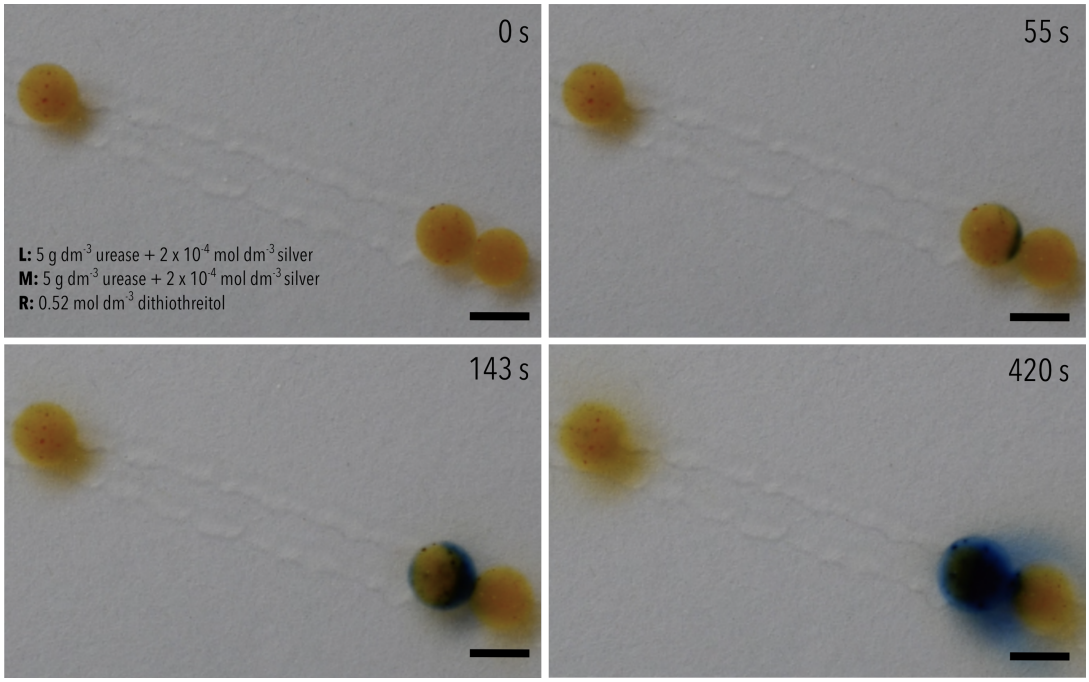

Figure 4.6 | When a bead containing both urease, at a concentration of 5 g dm^{-3}, and silver, at a concentration of 2 x 10^{-4} mol dm^{-3}, is immersed in a 0.1 mol dm^{-3} solution of urea, no pH increase is observed (left bead). If an identical bead (middle bead) makes contact with one containing 0.52 mol dm^{-3} DTT (right bead), the contained DTT diffuses into the silver-bound 'enzyme' bead. This results in the chelation of silver ions from the urease and thus its reactivation. Scale bar = 5 mm. See the video that accompanies the paper for full sequence.

Just as in figure 4.5, a 1 x 10^{-3} mol dm^{-3} 'silver' bead sits next to a 0.125 g dm^{-3} 'urease' bead (far left and the top middle bead, respectively). In this case, however, a third bead is introduced, namely a 0.52 mol dm^{-3} 'DTT' bead (bottom middle). The far-right bead, containing 0.125 g dm^{-3} urease, undergoes its colour and pH change as expected (onset at 214 seconds).

As the left-hand 'enzyme' bead makes contact with a 'silver' bead, a pH increase after this time period is not observed, as the silver inhibits the enzyme. After a longer delay (420 seconds), a pH increase is observed, in contrast to figure 4.5 where no 'DTT' bead is present. We infer that the 'DTT' bead present in figure

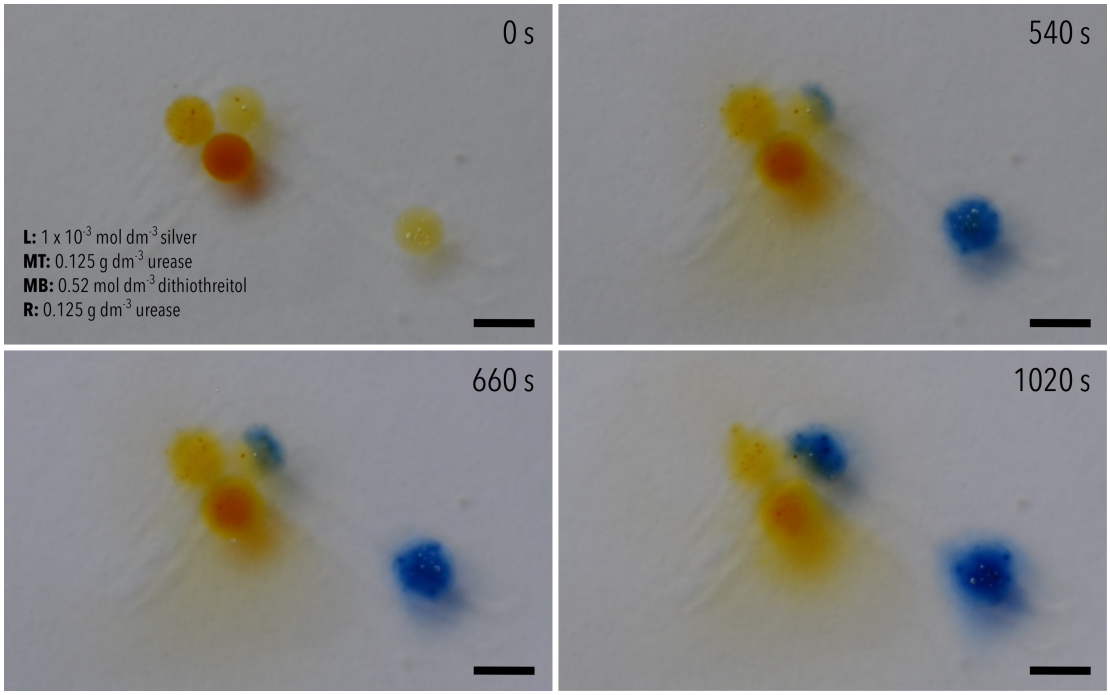

Figure 4.7 | Just as in figure 4.5, a 1 x 10^{-3} mol dm^{-3} 'silver' bead sits next to a 0.125 g dm^{-3} 'urease' bead (far left and the top middle bead, respectively) in an aqueous solution of 0.1 mol dm^{-3} urea. In this case, however, a third bead is introduced, namely a 0.52 mol dm^{-3} 'DTT' bead (bottom middle). The far-right bead, containing 0.125 g dm^{-3} urease, undergoes its colour and pH change as expected (onset at 214 seconds). As the left-hand 'enzyme' bead makes contact with a 'silver' bead, a pH increase after this time period is not observed, as the silver binds to the enzyme active site. After a longer delay (420 seconds), a pH increase is observed, in contrast to figure 4.5 where no 'DTT' bead is present. Scale bar = 5 mm. See the video that accompanies the paper for full sequence.

4.7 competes with the 'silver' bead, chelating and thus removing any silver blocking urease activity. Importantly, the observed behaviour of the 'enzyme' bead requires communication with both the 'silver' and 'DTT' bead, in the form of two competitive chemical signals.

4.3 Conclusions

In conclusion, we have demonstrated that by using a trio of simple biochemical, inorganic and organic molecules, we can conduct exchanges of communications, or 'conversations' between soft hydrogel beads. The interplay between the enzyme urease, the enzyme inhibitor silver (Ag^+), and the Ag^+ chelator dithiothreitol (DTT) allows for exchange of information of complexity analogous to signalling in simple microorganisms and to the physiochemical mechanisms theorised to have been used by the earliest protocells. We believe that this system demonstrates an advance in the communication capabilities of entirely soft systems.

4.4 Experimental methods

4.4.1 Materials

Alginic acid sodium salt (referred to as sodium alginate in this paper), calcium chloride hexahydrate (98%), calcium hydroxide (≥ 95 %, ACS reagent) urease from *Canavalia ensiformis* (Jack bean) type III (100K units), DL-dithiothreitol (≥ 98 %), silver nitrate (≥ 99.0 %) and urea (99.0 - 100.5%) were purchased from Sigma Aldrich. Acetic acid glacial and bromothymol blue, ACS reagent were purchased from Fisher Scientific.

4.4.2 Gel bead synthesis

Sodium alginate solutions were prepared by dissolving dry alginic acid powder in water at an appropriate concentration (5 or 10 wt. %) overnight. Once prepared, solutions were used within 3 weeks. 0.1 mol dm^{-3} aqueous solutions of silver nitrate were prepared and kept in darkness to prevent degradation. Once prepared, these were used within 1 week.

4.4.2.1 Urease beads

In the case of 1 and 5 g dm^{-3} urease beads, dry urease powder was dissolved into 5 wt. % sodium alginate solutions at appropriate concentrations. For lower concentration urease beads, 1 g dm^{-3} aqueous urease solutions were prepared, diluted as necessary, and combined with appropriate volumes of 10 wt. % sodium alginate solutions to produce solutions of a desired urease concentration. Bromothymol blue was added to each of these urease/sodium alginate solutions at a concentration of 2 mg cm^{-3} and corrected to a pH of 3.5 using a 1 mol dm^{-3} aqueous solution of acetic acid.

4.4.2.2 Urease/silver beads

For beads containing both urease and silver nitrate, the above protocol (*urease beads*) was repeated. This was followed by the addition of an aliquot of 0.1 mol dm^{-3} aqueous solution of silver nitrate to produce solutions of a desired silver ion concentration. These solutions were kept in darkness to prevent degradation.

4.4.2.3 Silver beads

An aliquot of 0.1 mol dm^{-3} aqueous solution of silver nitrate was added to 5 cm^3 of 5 wt. % sodium alginate solution to produce a solution of a desired silver ion concentration. Bromothymol blue was added at a concentration of 2 mg cm^{-3} and corrected to a pH of 3.5 using a 1 mol dm^{-3} aqueous solution of acetic acid. The solution was kept in darkness to prevent degradation.

4.4.2.4 Dithiothreitol beads

0.08 g of dithiothreitol was added to 1 cm^3 of 5 wt. % sodium alginate solution. Bromothymol blue was added at a concentration of 2 mg cm^{-3} and corrected to a pH of 3.5 using a 1 mol dm^{-3} aqueous solution of acetic acid.

To form solid beads, these 4 alginate solutions were introduced to calcium ions, hereby ionically cross-link the alginic acid polymer chains to form millimetre sized beads with liquid cores. Beads make contact with calcium solutions for a few minutes, which is not long enough to cross-link throughout the bead. Alginate beads were cross-linked by dropping the alginate solution into a 0.1 mol dm^{-3} solution of calcium chloride hexahydrate from a pipette tip. For silver beads, a 0.1 mol dm^{-3} aqueous solution of calcium hydroxide was used as the calcium ion source (so as to prevent precipitation of silver chloride). Both solutions are corrected to pH 3.5 using a 1 mol dm^{-3} aqueous solution of acetic acid. Beads are rinsed in deionised water before use.

4.4.3 Communication experiments

For all experiments, gel beads were immersed in a petri dish containing 20 cm^3 of deionised water and 2 cm^3 of a 1 mol dm^{-3} aqueous solution of urea corrected to a pH of 3.5 using a 1 mol dm^{-3} aqueous solution of acetic acid. Communication experiments were filmed on a Nikon D5100 camera with AF-S DX Micro NIKKOR 40mm f/2.8G Lens.

4.4.4 Full timings breakdown

Table 4.1 Full timings breakdown

		Onset of blue colour / seconds	
Experiment	**Figure**	**Blank bead**	**Paired bead**
1 g dm^{-3} enzyme/silver bead	2	25	*n/a*
1 g dm^{-3} enzyme + silver bead	3a	38	43
0.25 g dm^{-3} enzyme + silver bead	3b	82	130
0.125 g dm^{-3} enzyme + silver bead	3c	218	*n/a*
5 g dm^{-3} enzyme/silver + DTT bead	4	*n/a*	42
0.125 g dm^{-3} enzyme + silver + DTT bead	5	214	420

4.5 References

1 H. M. Schaefer, in *Animal Behaviour: Evolution and Mechanisms*, ed. P. M. Kappeler, Springer Berlin Heidelberg, Berlin, 2010, ch. 1, pp. 3-28.

2 P. Fedurek and K. E. Slocombe, *Hum. Biol.*, 2011, **83**, 153–173.

3 M. J. Hertenstein and D. Keltner, *Sex Roles*, 2011, **64**, 70–80.

4 A. Llopis-Lorente, P. Díez, A. Sánchez, M. D. Marcos, F. Sancenón, P. Martínez-Ruiz, R. Villalonga and R. Martínez-Máñez, *Nat. Commun.*, 2017, **8**, 15511.

5 M. E. Taga and B. L. Bassler, *Proc. Natl. Acad. Sci.* , 2003, **100**, 14549–14554.

6 G. Witzany, *Plant Signal. Behav.*, 2006, **1**, 169–78.

7 A. Sbarbati and F. Osculati, *Cells Tissues Organs*, 2006, **183**, 206–219.

8 M. F. Ali and E. D. Morgan, *Biol. Rev.*, 1990, **65**, 227–247.

9 T. Nakano, M. J. Moore, Fang Wei, A. V. Vasilakos and Jianwei Shuai, *IEEE Trans. Nanobioscience*, 2012, **11**, 135–148.

10 B. P. Bean, *Nat. Rev. Neurosci.*, 2007, **8**, 451–465.

11 C. M. Waters and B. L. Bassler, *Annu. Rev. Cell Dev. Biol.*, 2005, **21**, 319–346.

12 G. M. Cooper, *The Cell: A Molecular Approach. 2nd edition.*, Sinauer Associates, Sunderland, MA, United States, 2000.

13 J. S. King and R. H. Insall, *Trends Cell Biol.*, 2009, **19**, 523–530.

14 V. V. Yashin, G. V. Kolmakov, H. Shum and A. C. Balazs, *Langmuir*, 2015, **31**, 11951–11963.

15 D. A. Hammer and N. P. Kamat, *FEBS Lett.*, 2012, **586**, 2882–2890.

16 O. Kuksenok, P. Dayal, A. Bhattacharya, V. V. Yashin, D. Deb, I. C. Chen, K. J. Van Vliet and A. C. Balazs, *Chem. Soc. Rev.*, 2013, **42**, 7257-7277.

17 G. V Kolmakov, V. V Yashin, S. P. Levitan and A. C. Balazs, *Proc. Natl. Acad. Sci.* , 2010, **107**, 12417–12422.

18 O. B. Usta, A. Alexeev, G. Zhu and A. C. Balazs, *ACS Nano*, 2008, **2**, 471–476.

19 P. Dayal, O. Kuksenok and A. C. Balazs, *Proc. Natl. Acad. Sci. U. S. A.*, 2013, **110**, 431–6.

20 L. Zhang and X. Wang, *J. Phys. Chem. Lett.*, 2015, **6**, 2530–2537.

21 H. Shum, V. V. Yashin and A. C. Balazs, *Soft Matter*, 2015, **11**, 3542–3549.

22 M. Ibele, T. E. Mallouk and A. Sen, *Angew. Chemie Int. Ed.*, 2009, **48**, 3308–3312.

23 C. Giménez, E. Climent, E. Aznar, R. Martínez-Máñez, F. Sancenón, M. D. Marcos, P. Amorós and K. Rurack, *Angew. Chemie Int. Ed.*, 2014, **53**, 12629–12633.

24 A. Jesorka, N. Stepanyants, H. Zhang, B. Ortmen, B. Hakonen and O. Orwar, *Nat. Protoc.*, 2011, **6**, 791–805.

25 A. Karlsson, R. Karlsson, M. Karlsson, A.-S. Cans, A. Strömberg, F. Ryttsén and O. Orwar, *Nature*, 2001, **409**, 150–152.

26 R. Lentini, N. Y. Martín, M. Forlin, L. Belmonte, J. Fontana, M. Cornella, L. Martini, S. Tamburini, W. E. Bentley, O. Jousson and S. S. Mansy, *ACS Cent. Sci.*, 2017, **3**, 117–123.

27 S. Tateyama, Y. Shibuta and R. Yoshida, *J. Phys. Chem. B*, 2008, **112**, 1777–1782.

28 I. C. Chen, O. Kuksenok, V. V. Yashin, A. C. Balazs and K. J. Van Vliet, *Adv. Funct. Mater.*, 2012, **22**, 2535–2541.

29 A. R. DeGroot and R. J. Neufeld, *Enzyme Microb. Technol.*, 2001, **29**, 321–327.

30 N. Das, A. M. Kayastha and O. P. Malhotra, *Biotechnol. Appl. Biochem.*, 1998, **27**, 25–9.

31 R. W. Jaggers and S. A. F. Bon, *Mater. Horiz.*, 2017, **4**, 402–407.

32 R. W. Jaggers and S. A. F. Bon, *J. Mater. Chem. B*, 2017, **5**, 7491-7495.

33 G. R. Behbehani, A. A. Saboury, A. Taherkhani, L. Barzegar and A. Mollaagazade, *J. Therm. Anal. Calorim.*, 2011, **105**, 1081–1086.

34 X. Ma, X. Wang, K. Hahn and S. Sánchez, *ACS Nano*, 2016, **10**, 3597–3605.

35 L. Hellerman, M. E. Perkins and W. M. Clark, *Proc. Natl. Acad. Sci. U. S. A.*, 1933, **19**, 855–60.

36 B. Krajewska, *J. Enzyme Inhib. Med. Chem.*, 2008, **23**, 535–542.

37 B. Krajewska, W. Zaborska and M. Chudy, *J. Inorg. Biochem.*, 2004, **98**, 1160–1168.

5 Control of capsule membrane permeability with catalytic particles

This chapter details research published in the paper: R. W. Jaggers, R. Chen, and S. A. F. Bon, *Materials Horizons*, 2016, **3**, 41-46

5.1 Introduction

A vesicle is a self-contained body of liquid surrounded by a lamellar, often bilayer-type, membrane dispersed in a liquid environment. In nature, the membranes of vesicles and cells are composed of phospholipid amphiphiles. These amphiphiles contain both a hydrophilic and hydrophobic domain which allows them be assembled into bilayer-type spherical structures.[1] Their membranes are composed of an inner hydrophobic region surrounded by outer hydrophilic domains that face the inner and outer aqueous environments in which the vesicle can be found.[2]

Vesicles can also be formed artificially by the spontaneous assembly of amphiphilic building blocks under appropriate solvent conditions, given that the ratio between the hydrophilic and hydrophobic domains is appropriate.[3–5] These building blocks can be either natural or synthetic, namely lipids or di-block copolymers, and their corresponding structures are known as *liposomes* or *polymersomes*, respectively.

Compartmentalisation of small and finite volumes of liquids and the consecutive emergence of membrane bioenergetics are identified as being of key importance in the evolution of cells, and hence the origins of life.[6] The ability to mediate transport across a cell membrane is crucial for cellular activity, from regulation of ion transport to uptake of nutrients.[7] In eukaryotic and prokaryotic cells, functional proteins embedded in the cell membrane regulate transport of ions and molecules and are known as transmembrane proteins (TMPs). This concept of regulating and controlling membrane permeability on demand is being explored in a variety of scientific fields, using a range of both biological and chemical methods.

A pioneering example where biology, in the form of TMPs, meets synthetic macromolecular chemistry, in the form of polymer vesicles, was reported by Meier and co-workers in which polymersome nanoreactors were permeabilised to small solutes by the inclusion of a nonspecific channel protein, bacterial porin OmpF, into the membrane wall.[8] In a different study, Meier and co-workers demonstrated the incorporation of Aquaporin Z, a water channel protein, into the walls of polymeric vesicles.[9] Inclusion of this protein resulted in a significantly increased water permeability, almost 90 times greater than vesicles without. Choi and Montemagno elegantly demonstrated that several proteins working in conjunction with one another could be inserted into a vesicle membrane, creating a multi-protein, light-driven adenosine triphosphate (ATP) engine.[10] Moreover, channel proteins have also been used to mediate deoxyribonucleic acid (DNA) translocation by acting as a receptor for binding bacteriophage viruses, creating polymeric vehicles for DNA.[11]

Synthetic membrane channels have also been used to modify the permeability of polymeric vesicles, for example, Hammer and colleagues showed that the inclusion of dendritic helical pores facilitates proton transport across a membrane.[12] Perrier, Jolliffe and co-workers demonstrated the use of cyclic peptide– poly(*N*-isopropylacrylamide) conjugates as thermoresponsive channels,[13] whilst Gin *et al.* showed that aminocyclodextrins can be used as anion-selective channels.[14]

The use of membrane channels is not the only route towards gaining control of transmembrane transport; the inherent permeability of a vesicle membrane itself can be influenced by physical phenomena. Near their liquid-crystalline transition temperatures, liposomes exhibit an enhanced leakiness of their membranes,[15] a property exploited by Yatvin and co-workers in their design of temperature-controlled, drug-releasing vesicles.[16] Battaglia and co-workers demonstrated shear-rate induced modulation of polymersome membrane permeability.[17]

The amphiphilic balance of the macromolecular building blocks of polymer vesicles can be altered to regulate permeability. Oxidative responsive

polymersomes in which the hydrophobic propylene sulfide units were oxidised by hydrogen peroxide into their more hydrophilic propylene sulfoxide analogues were reported by Tirelli, Hubbell and co-workers.[18] A variation on this concept using glucose oxidase to generate hydrogen peroxide in situ was reported by Hubbell *et al.*[19] Ahmed and Discher showed that triggered partial hydrolysis of the block copolymer building blocks of vesicular structures induced self-porating membranes capable of enhanced release.[20] Du and Armes showed a pH dependence in polymersome membrane assembly that affects permeability.[21] Eisenberg *et al.* interestingly showed that an alternating pH in the surrounding solution of a vesicle can trigger a "breathing" behaviour, resulting in the diffusion of species in and out of the vesicle upon a reversible change in vesicle volume.[22] Van Hest and co-workers incorporated phenyl boronic acid based stimuli responsive block copolymers into vesicular structures which allowed for pore formation at both high pH and sugar exposure.[23] De Geest and co-workers created core–shell capsules consisting of a degradable microgel core surrounded by a semi-permeable membrane. Upon degradation of the microgel core, the accompanied increase in osmotic pressure ruptures the surrounding membrane and triggers the release of the encapsulated species.[24]

One interesting approach is the use of functional nanoparticles on or in the membrane, as well as inside, of manmade vesicles. In these hybrid supracolloidal structures it has been shown that control of membrane permeability is possible using the characteristic features of the nanoparticles.

Oh and co-workers incorporated nanoparticles of silver[25] and gold[26] into the membranes of phospholipid vesicles and showed enhanced membrane fluidity and thus permeability. Paasonen and colleagues used the concept of hyperthermia to show that exposure to light of vesicles with gold nanoparticles on or in their membranes enhanced their permeability.[27] Weitz *et al.* created giant polymersomes from poly(*N*-isopropyl acrylamide) containing di-block copolymers and gold nanoparticles using microfluidics.[28] These polymersomes exhibited thermo- and photo-responsive behaviour, as well as tuneable permeability. Lecommandoux and

others prepared magneto-responsive polymer vesicles by embedding iron oxide nanoparticles into the lamellar membranes of vesicles.[29–34] Upon exposure to an externally applied magnetic field the vesicles could undergo magnetotaxis (gradient field), deform, be used as contrast agents in magnetic resonance imaging and as drug delivery vehicles that delivered their payload by means of radiofrequency magnetic hyperthermia.

In this chapter, we show that manganese oxide particles that are embedded into the membranes of polymer capsules are able to enhance permeability upon activation and reaction of the catalytic particles with small amounts of hydrogen peroxide. To the best of our knowledge, this concept of using chemical heterogeneous catalysis as a strategy to influence membrane permeability has not been previously reported. We believe that our method offers an interesting tactic to control and regulate release from vesicular structures dispersed in a liquid.

5.2 Results and Discussion

Since their first description in 1925, double emulsion droplets have received continued interest.[35] Double emulsion droplets of controlled dispersity can be made, for example, by membrane emulsification techniques,[36] using T-shaped microchannels,[37] electrified coaxial liquid jets,[38] or in this case, flow focusing microfluidic devices.[39–42]

Polymer capsules of low dispersity in size distribution were prepared using a microfluidics technique from water-*in*-oil-*in*-water double-emulsion droplets, with a middle phase of chloroform containing poly(*n*-butyl methacrylate)$_{94}$-*block*-poly-(2-(dimethylamino) ethyl methacrylate)$_{37}$ and manganese oxide particles, as shown in figure 5.1.

For membrane permeability and release studies, which are described later, the inner aqueous phase contained either sodium sulfate, sodium fluoride, or congo red dye.

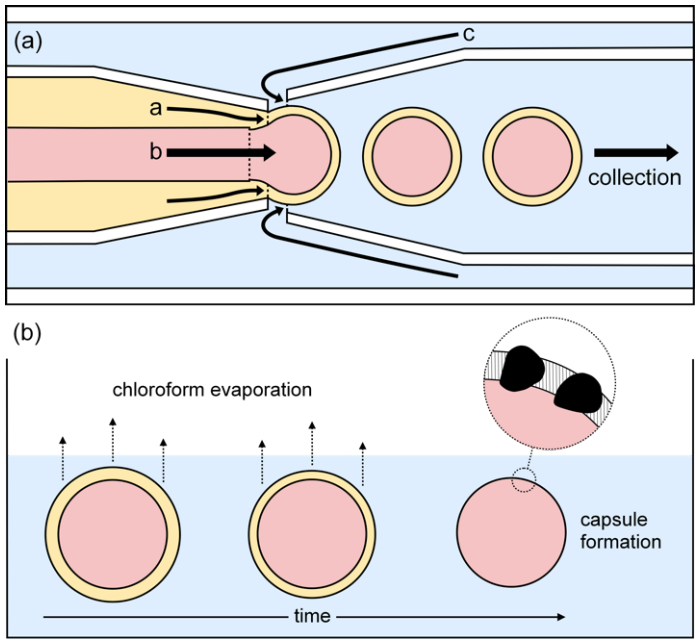

Figure 5.1 | Schematic drawings of (a) the formation of double emulsion droplets of low dispersity in size distribution using a flow-focussing microfluidic device. An inner aqueous phase (pink, b) is contained within an intermediate organic phase containing amphiphilic block copolymer, poly(*n*-butyl methacrylate)-*block*-poly(2-(dimethylamino) ethyl methacrylate, and catalyst particles (yellow, a) in an aqueous outer phase (blue, c); (b) the formation of capsules from the double emulsion droplets. After evaporation of the volatile organics from the middle phase, vesicular polymer capsules are formed, containing catalyst, that is manganese oxide, particles in their walls.

Dark field microscopy indicates that manganese oxide particles are part of the membrane of the capsule as scattering is observed, as shown in figure 5.2, a. Cryogenic scanning electron microscopy confirms that manganese oxide particles are embedded into the membrane of the polymer capsule, shown in figure 5.3. The addition of small amounts of hydrogen peroxide (0.1 wt. %) to sodium sulfate loaded capsules dispersed in a barium chloride solution showed a steady release of their content in the form of observed precipitation of barium sulfate particles, see figure 5.2, b.

This observation implies a dramatic change in permeability of the capsule membranes when exposed to a chemical trigger and prompted us to study the

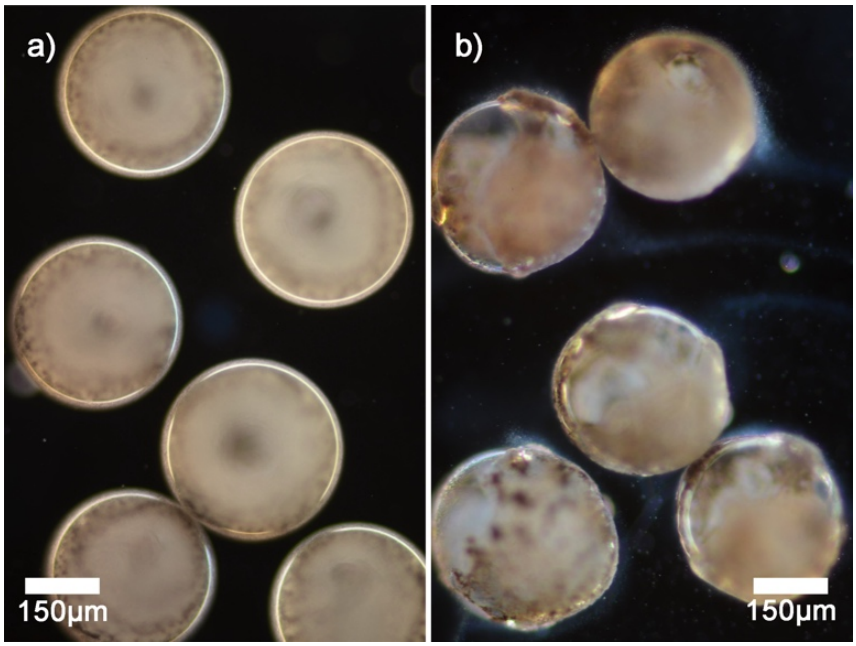

Figure 5.2 | Dark field microscopy images of (a) capsules with membrane embedded manganese oxide particles; (b) capsules undergoing slow release of encapsulated sulfate ions upon addition of a small amount of hydrogen peroxide. The outer water phase contains Ba^{2+} cations, and hence the precipitation of barium sulfate occurs, which is observed as a haze.

release characteristics of the catalytic manganese oxide containing membranes quantitatively.

Fluoride ion selective electrode measurements were carried out in the continuous phase of sodium fluoride loaded capsules. To provide reference, the release profiles of capsules with and without embedded manganese oxide particles were compared, as shown in figure 5.4. Complete release of fluoride ions results in a concentration of 62 ppm.

The capsules without manganese particles showed a significantly higher release rate of fluoride ions than those with particles embedded in their membranes. It is worth noting that the experiments start when chloroform has not fully evaporated from the membrane phase. Its presence led to retardation, as initially a thicker hydrophobic barrier has to be overcome by the ions. For capsules without particles in their walls, this retardation period was 20–30 min. Once chloroform had

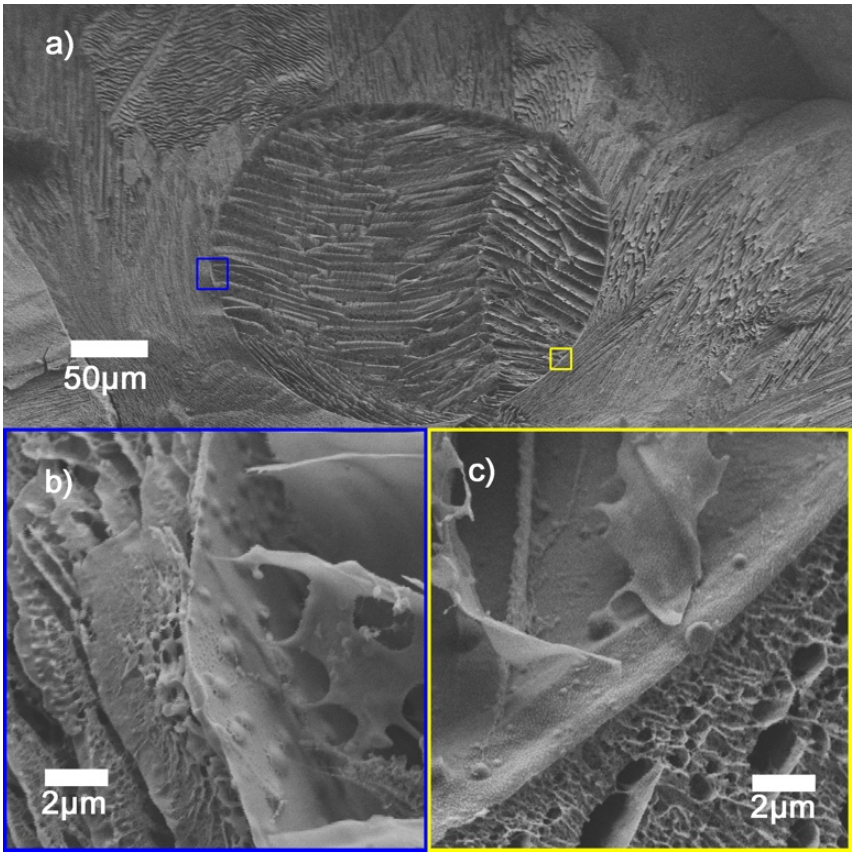

Figure 5.3 | Cryo-SEM images of capsules with membrane embedded manganese oxide particles: (a) overview image of a single frozen capsule in ice; (b) magnified observation of the region in blue in panel (a); (c) magnified view of the region in yellow in panel (a). The manganese oxide particles can be clearly observed to be part of the vesicular membrane. These images suggest a wall thickness of 100-200 nm, far exceeding those that would be observed in the case of a unilamellar vesicular structure. The capsule wall may be multilamellar or less ordered.

evaporated, the release rate reached its maximum and started to decelerate as the concentration difference between the inside and outside of the capsules decreased. Strikingly, the chloroform evaporation process took much longer for the capsules with manganese dioxide particles (about 100–110 min, see figure 5.4). It is plausible that both the reduced effective surface area due to the presence of impermeable manganese oxide particles (*ca.* 20 volume percent of the membranes) and particle induced light scattering (protecting the capsules from heating up due to light exposure under the microscope) explain this observation. We speculate that the

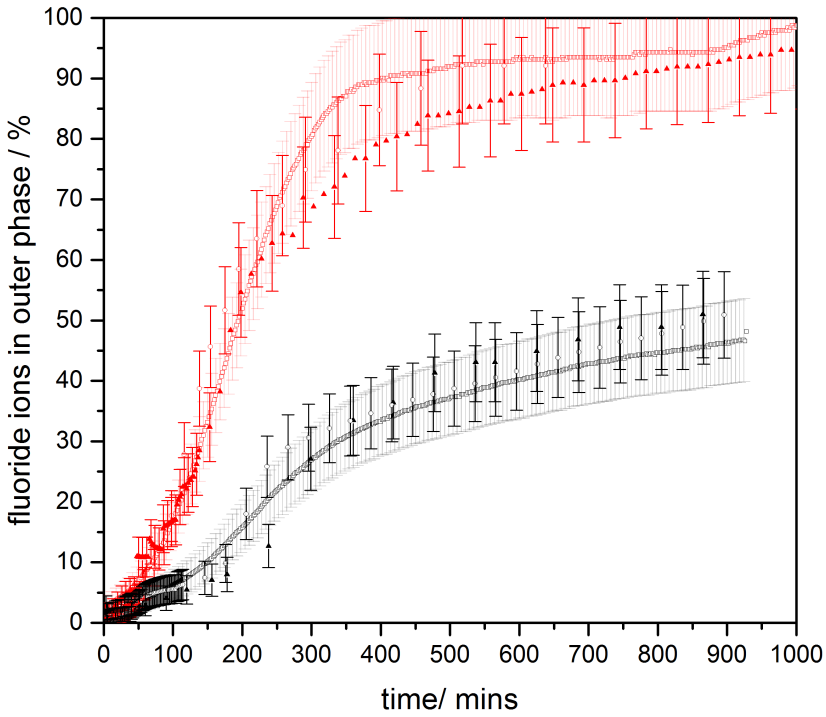

Figure 5.4 | Fluoride ion release profiles of two different capsule populations. 'Naked' capsules (red), containing no manganese oxide particles, show a faster rate of release than those with (black). Square root error bars.

slowdown of release after *ca.* 300 minutes is due to the fading out of the chloroform plasticisation effect, making the capsule membranes less fluid-like.

The release behaviour of the manganese oxide capsules exposed to different hydrogen peroxide solutions was studied. For this we prepared water-based dispersions of *ca.* 6000 capsules containing 0.2 mol dm^{-3} sodium fluoride (6 cm^3 of water outer phase, 0.1 cm^3 of inner aqueous phase). Again, release profiles were measured with a fluoride selective electrode. When a diluted hydrogen peroxide solution was added after 150 min, 0.2 cm^3 of 3 wt. % H_2O_2 (establishing a bulk H_2O_2 concentration of *ca.* 0.1 wt. %), a clear increase in membrane permeability and thus enhanced release rate of fluoride ions was observed, see figure 5.5. Approximately 20–30 minutes after this stimulus, the release rate dropped to a similar level to that of the sample without H_2O_2 (in the region between 200 minutes and 250 minutes), indicating that the majority of the hydrogen peroxide trigger had been consumed. The same treatment was repeated at both 250 minutes

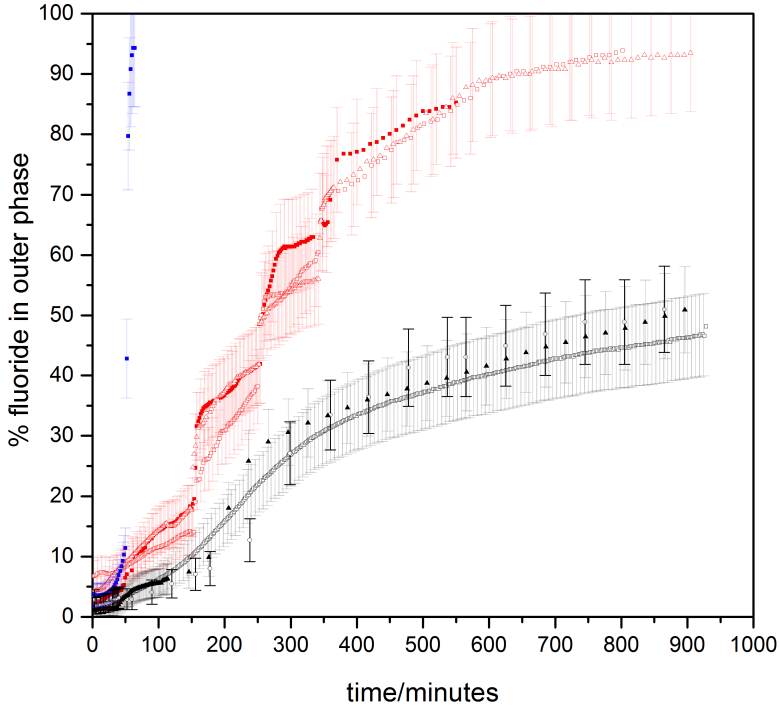

Figure 5.5 | Fluoride ion release profiles of water-based dispersions of *ca.* 6000 MnO_2 particle embedded capsules containing 0.2 mol dm^{-3} sodium fluoride (6 cm^3 of water outer phase, 0.1 cm^3 of inner aqueous phase) with (a) 3.0 cm^3 of 30 wt. % H_2O_2 added at 50 min (blue, dashed vertical line indicates time of hydrogen peroxide addition), (b) aliquots of 0.2 cm^3 of 3 wt. % H_2O_2 added at 150, 250 and 340 min (red, solid vertical lines indicate time of hydrogen peroxide addition), and (c) no H_2O_2 stimulus (black). This process of "catalytic" enhanced release was visualized clearly under dark field microscopy observations in which release of sulfate ions triggered the formation of insoluble barium sulfate particles (see figure 5.2, b). Square root error bars.

and 340 minutes in order to confirm the initial observation. Again, a temporary increase in membrane permeability was observed. This shows that the catalytic reaction between hydrogen peroxide and the manganese oxide particles increases membrane permeability until the hydrogen peroxide is depleted, see figure 5.5. The exact mechanism of this temporary increased permeability is not fully understood. We hypothesise that the catalytic breakdown of hydrogen peroxide to dioxygen and water at the site of the particles induces the formation of transient openings at the interface between the particles and the membrane, thus increasing membrane permeability. It is important to note that the driving force for release

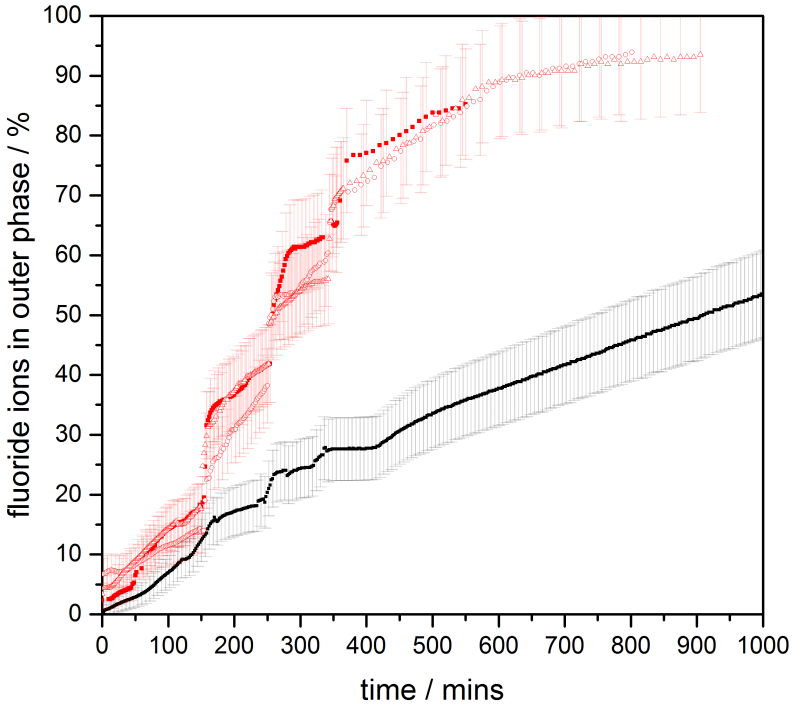

Figure 5.6 | Fluoride ion release of particle-embedded capsules with hydrogen peroxide (red) and water (black) triggers at 150, 250 and 340 minutes. Square root error bars.

depends on the difference between the concentrations of fluoride ions inside and outside of the polymer capsules. Therefore, we also carried out blank experiments in which aliquots of water were added. Indeed, small enhancements of release rates were observed in line with the induced concentration change, as shown in figure 5.6. However, this effect was minor in comparison with the hydrogen peroxide catalytic trigger. Another point worth noting, which could plausibly explain enhanced release, is the potential self-destruction of a sub set of capsules upon addition of the hydrogen peroxide trigger. We therefore carried out smaller scale experiments with 200 capsules and counted the capsules before and after our release experiments. Less than 4 capsules (2 %) were found to be destroyed in each of these runs. The majority of capsules survive the peroxide trigger and therefore we can conclude that that enhanced membrane permeability was indeed achieved by the catalytic activity of the manganese oxide particles.

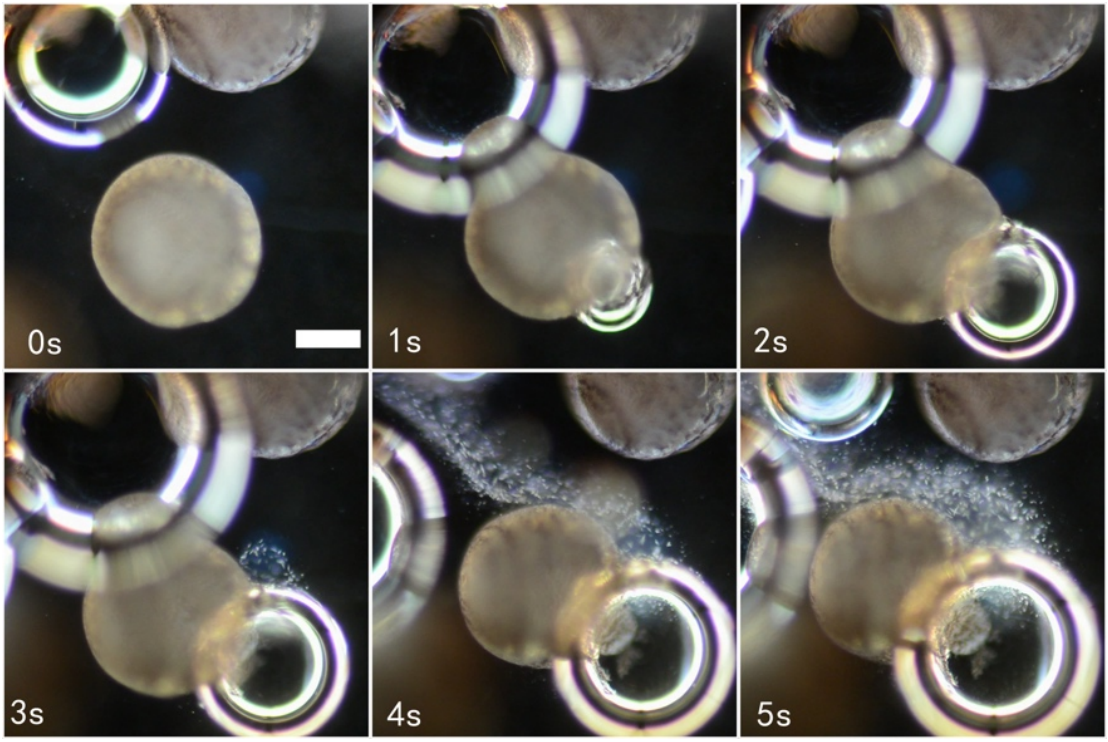

Figure 5.7 | Dark microscopy sequence of video stills (see video that accompanies paper DOI: 10.1039/C5MH00093A) of a water-based (containing barium cations) dispersion of capsules with membrane embedded manganese oxide particles and loaded with sodium sulfate, after the addition of a large aliquot of hydrogen peroxide. The stills show the formation of oxygen bubbles, leading to deformation and rupture of the capsule membranes hereby releasing the sulfate ion content, as visualized by the formation of a stream of *in situ* formed barium sulfate particles (a white haze). Scale bar: 150 μm.

One could argue that the manganese oxide particles act as stoppers, which upon peroxide activation, could pop out, hereby creating a temporary pore allowing for the observed enhancement in release of fluoride ions. ICP-OES measurements of the outer water phase post peroxide treatment showed no sign of presence of manganese. We therefore can confirm that the manganese oxide particles remained associated with the capsule membranes (the experimental methods section describes this experiment in detail).

Triggered release of the full capsule contents from hybrid capsules is possible upon exposure to high concentrations of hydrogen peroxide (3.0 cm^3, 30 wt. %). The formation of oxygen bubbles upon catalytic reaction causes imminent membrane deformation and rupture, followed by immediate release and self-destruction of the capsules (figure 5.5, blue, and figure 5.7).

A question one could ask is if there is a variation between release profiles of different compounds from the capsules. The capsule membrane can be seen as a barrier for transport phenomena. We therefore decided to look at the release profile of the diazo dye congo red, which is the disodium salt of 3,30-([1,10-biphenyl]-4,40-diyl)bis(4-aminonaphthalene-1-sulfonic acid). In equivalent experiments to those of the aforementioned fluoride release ones, polymer

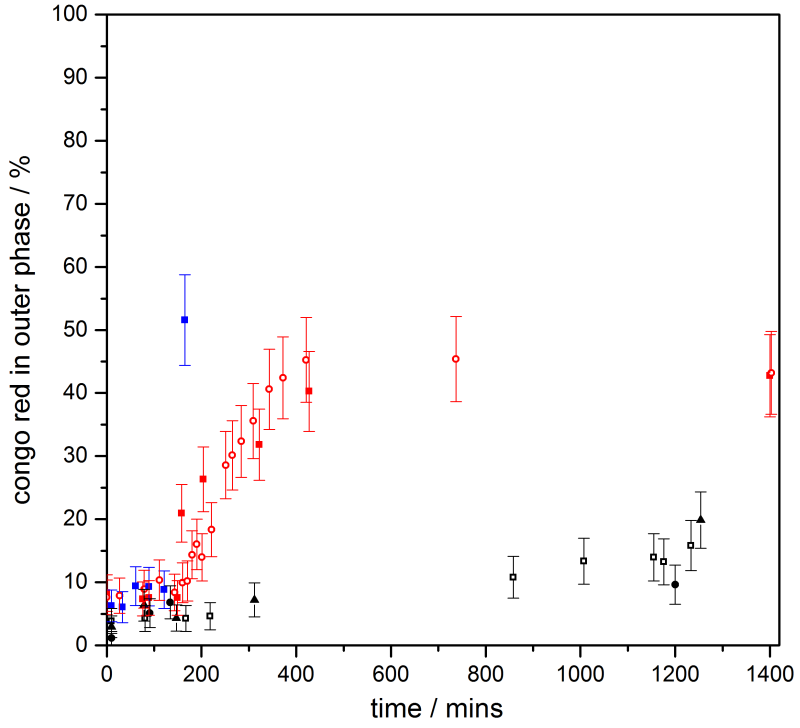

Figure 5.8 | Congo red release profiles of water-based dispersions of *ca.* 6000 MnO_2 particle embedded capsules containing 3.0 mmol dm^{-3} congo red dye (6 cm^3 of water outer phase, 0.1 cm^3 of inner aqueous phase) with (a) 3.0 cm^3 of 30 wt. % H_2O_2 (blue), or (b) 0.2 cm^3 of 3 wt. % H_2O_2 (red) added at 150 min (solid vertical line indicates time of hydrogen peroxide addition), and (c) no H_2O_2 stimulus (black). Square root error bars.

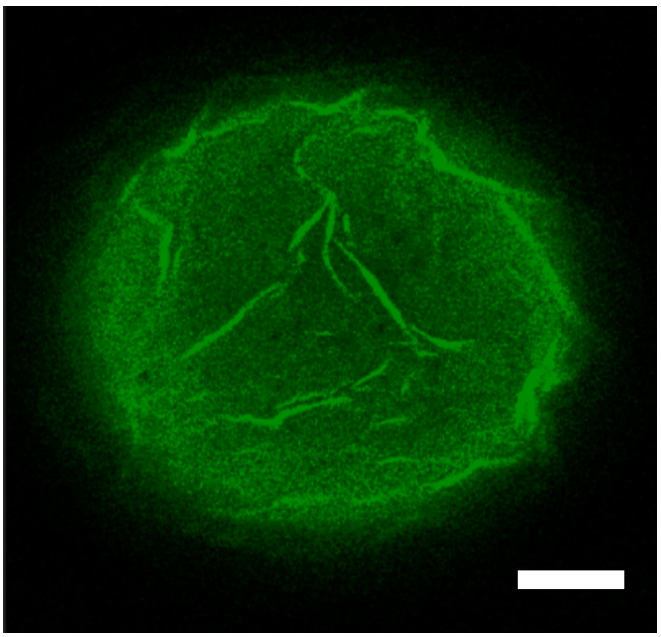

Figure 5.9 | Confocal microscope image of a partially buckled polymer capsule loaded with 0.003 mol dm^{-3} congo red dye solution, the capsule being dispersed in an aqueous sodium chloride environment. Scale bar = 50 μm.

capsules were loaded with an aqueous solution of congo red (3.0 mmol dm^{-3}) and the dye concentration in the outer phase was monitored using UV-Vis spectroscopy (λ_{max} = 505 nm). The results are displayed in figure 5.8.

As seen in the fluoride release experiments, treatment with 3.0 cm^3 of 30 wt. % hydrogen peroxide causes rupture of all capsules triggering instant and "complete" release, whilst a smaller 0.2 cm^3 of 3 wt. % of H_2O_2 treatment caused temporary acceleration of dye release. When we compare the release profiles of fluoride ions with congo red dye from manganese oxide loaded capsules in the absence of any trigger, the fraction of congo red released after 900 minutes is substantially lower, that is 11 % versus *ca.* 48 % of the fluoride ions. It should be noted, however, that over the time period of 400 to 900 minutes, release rates appear not to differ substantially.

The addition of 0.2 cm^3 of 3 wt. % of H_2O_2 after 150 min clearly enhances the release rate of congo red. What is striking is that in both catalytic scenarios the total amount released was limited to approximately 50 % of the encapsulated dye

expected to be released. We found that the reason for this was the strong physisorption of the dye to the amphiphilic block copolymer, that is poly(*n*-butyl methacrylate)$_{94}$-*block*-poly(2-(dimethylamino) ethyl methacrylate)$_{37}$. This strong adsorption, and therefore accumulation of congo red into the capsule membrane wall, was confirmed by confocal microscopy, see figure 5.9. For this we purposely buckled a polymer capsule using a sodium chloride solution. As can be seen from the image, a higher intensity and thus, concentration, of the dye was observed in the wrinkled parts of the membrane.

5.3 Conclusions

We have demonstrated that the permeability of vesicular-type structures containing catalytically active colloidal particles as part of their membrane can be regulated by use of a chemical trigger. This model system offers an exciting method of regulating and controlling transmembrane transport, which may be of interest to a range of scientific fields.

One comment we would like to make that relates to the area of the evolution of life is that a hybrid vesicular structure, which has "active" colloidal particles either adhered to the surface of the membrane, or embedded into it, can achieve chemically activated control of membrane permeability. This is what we have shown here.

The origin of biological membranes remains ambiguous. Wächtershäuser[43,44] and Russell and co-workers,[45] for example, argue that porous pyrite (FeS) structures found in deep-sea hydrothermal vents contain small pockets of water and have the ability to accumulate organic matter due to the relative hydrophobic nature of pyrite. The hypothesis is that these compartmentalised structures are suitable microenvironments for life to evolve and, therefore, can be seen as semi-permeable predecessors to protocells (protocells, the predecessors to modern cells, possess a self-replicating genome encapsulated by a membrane that can grow and divide, thus allowing it replicate. Unlike a cell, however, a protocell mediates its

cell uptake not with sophisticated membrane transport control, but by diffusion through the membrane alone. The evolution of these primitive cell analogues is a hot topic of debate amongst evolutionary scientists, with particular focus on the requirements of self-replication and cell function).[46,47] They are formed through precipitation and assembly of metal sulfides on the surface of hydrogen sulfide rich gas bubbles, another example being based on zinc sulfide.[48] A modern synthetic analogue of such semipermeable compartmentalised structures would be a colloidosome,[49] which can be built from colloidal particles that adhere to liquid–liquid, or liquid–gas interfaces, so-called Pickering stabilisers.[50] The next step in evolution of these early compartmentalised structures describes the formation of a cell membrane in the form of liposomes, and herein is where the problem lies. How would a primitive cell get its nutrients when modern model lipid-based cell membranes are effectively non-permeable for desired molecules on an acceptable time scale, if membrane-proteins are left out?[51] Mansy and co-workers suggested that protocells made with fatty acid components were able to take up nucleotides through concerted flipping,[52] fast at high temperatures, and that in addition DNA strand separation processes benefited from thermal fluctuations.[53] We would like to suggest here that a hybrid vesicular structure, which has "active" colloidal particles as part of its membrane, may have controlled permeability in primitive cells.

5.4 Experimental methods

5.4.1 Poly(*n*-butyl methacrylate)-*b*-poly(2-(dimethylamino) ethyl methacrylate) synthesis

5.4.1.1 Materials

Ethyl α-bromoisobutyrate (98%), 2-(dimethylamino) ethyl methacrylate (DMAEMA, 98%,), CuBr and *n*-butyl methacrylate (BMA, 99%) were obtained from Sigma-Aldrich. CuBr was purified using the method of Keller and Wycoff.[54] Before use, BMA and DMAEMA were passed through a column of aluminium

oxide (98%, basic, Sigma-Aldrich) to remove radical polymerisation inhibitors. *N*-(*n*-propyl)-2-pyridylmethanimine (PPMI, 95%) was prepared using the procedure reported by Haddleton and co-workers.[55]

5.4.1.2 Synthesis

Poly(*n*-butyl methacrylate)-*b*-poly(2-(dimethylamino)ethylmethacrylate) (pBMA-*b*-pDMAEMA) was synthesised by atomic transfer radical polymerisation (ATRP) as follows. To synthesise the first block (pBMA), a Schlenk tube was charged with 10 g toluene, 10 g BMA (70 mmol), 0.185g ethyl α-bromoisobutyrate (0.95 mmol) and 0.138 g CuBr (0.96 mmol). The tube was sealed and subjected to three freeze pump thaw cycles to de-aerate the sample then placed, stirring, into a 90 °C oil bath under a gaseous nitrogen atmosphere. After 15 minutes, 0.3 cm^3 of PPMI ligand was injected into the tube to initiate the reaction (turning the solution dark brown). The reaction was left for 4 hours after which the contents of the tube were exposed to air and cooled rapidly in a water bath.

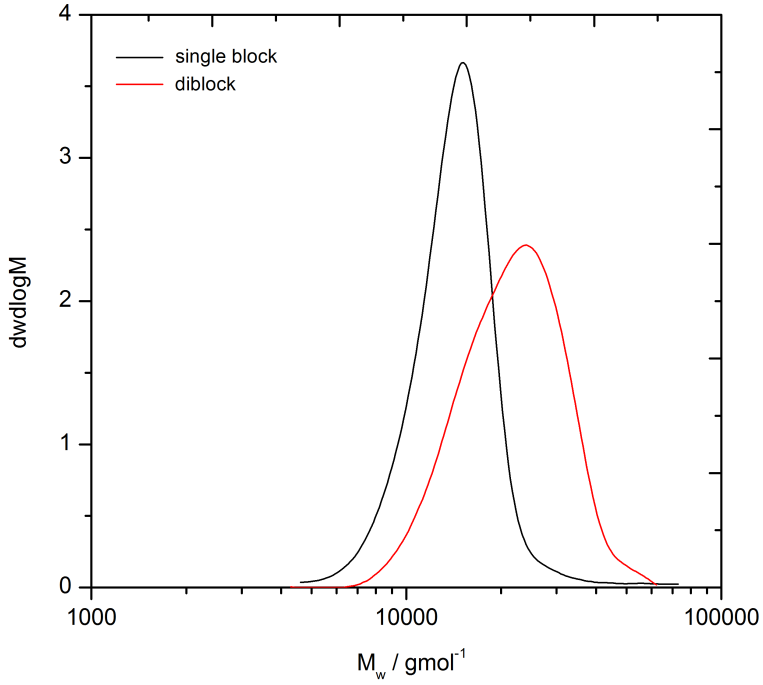

Figure 5.10 | Molar mass distribution plot of the BMA block (black) and the di-block copolymer (red).

5.4.1.3 Characterisation

p(BMA)-*b*-p(DMAEMA) (M_n = 20000 g mol^{-1}, PDI = 1.13) was obtained by the ATRP method described above. The molar mass distribution of the di-block

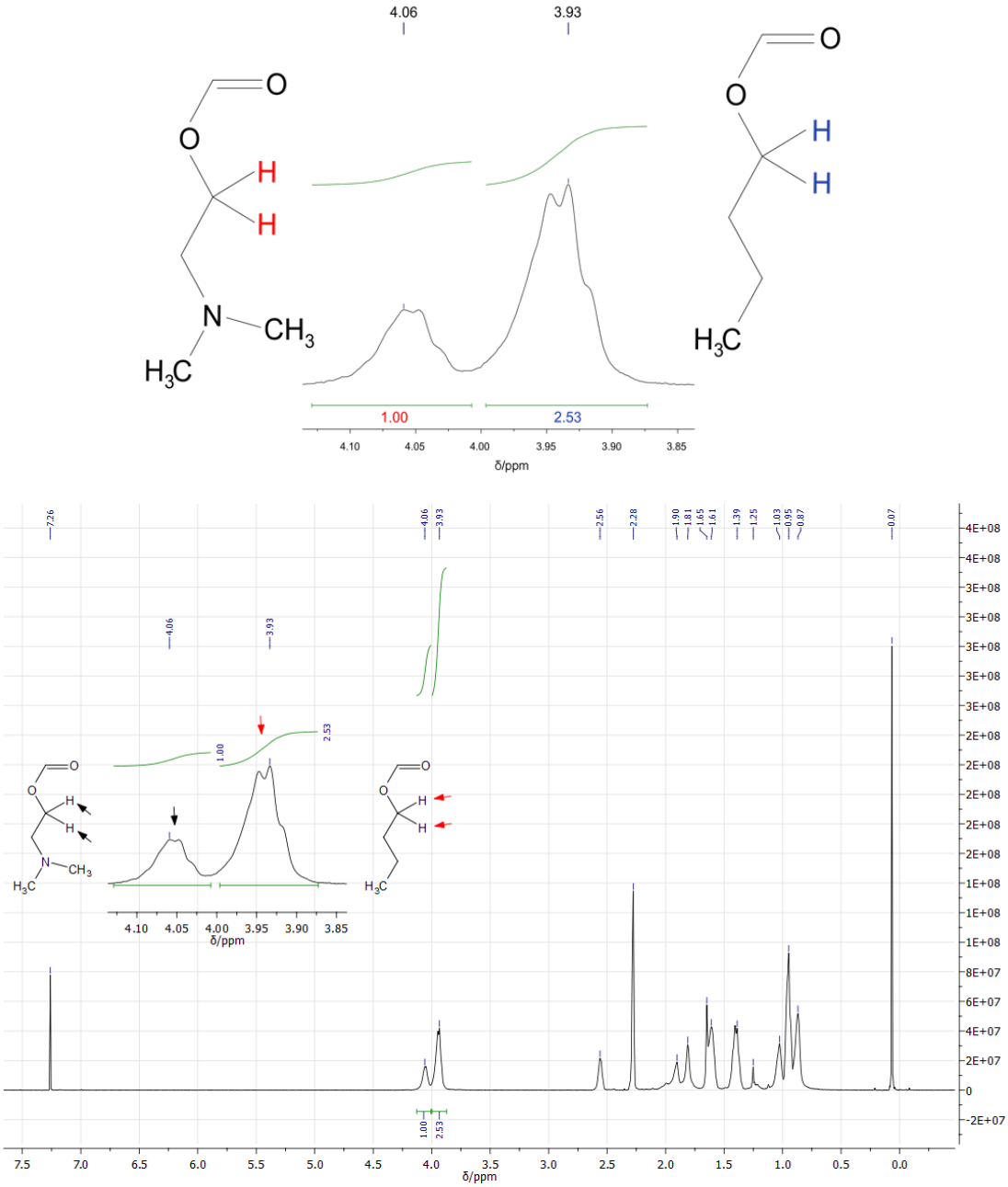

Figure 5.11 | Top The two proton environments used to assess block ratio alongside their H^1 NMR peaks **Bottom** The full H^1 NMR spectrum of poly(*n*-butyl methacrylate)-*block*-poly(2-(dimethylamino) ethyl methacrylate). ^{1}H NMR (400 MHz, $CDCl_3$, 298 K) δ = 0.07 (s, 2H); 0.80-1.1 (m, 9.2 H); 1.39 (m, 3H); 1.6 (m, 3H); 1.8 – 2.0 (m, 3H); 2.3 (s, 3H); 2.6 (m, 1H); 3.9 (m, 2.5 H); 4.0 (m, 1H).

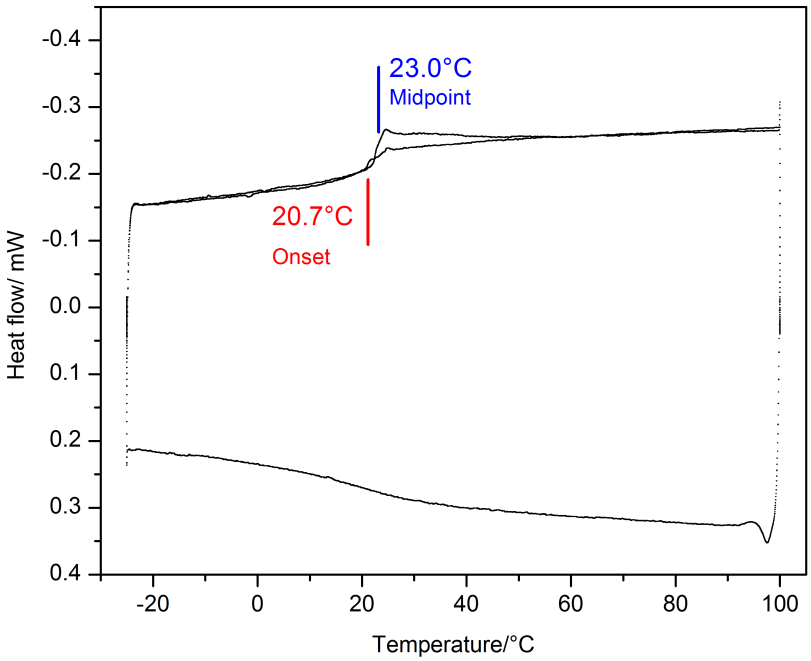

Figure 5.12 | The DSC curve of p(BMA)-*b*-p(DMAEMA) showing the onset and maximum glass transition temperature.

copolymer was determined using gel permeation chromatography (GPC) on the Agilent Varian 390-LC (refractive index detection, mixed E columns and chloroform mobile phase). Figure 5.10 shows the reported molecular weights. The first block, poly(*n*-butyl methacrylate) has a molecular weight of 13500 g mol^{-1} (degree of polymerisation (DP) of 94) and a molar-mass dispersity of 1.10. The di-block copolymer has a molecular weight of 20000 g mol^{-1} and a molar-mass dispersity of 1.13, therefore giving the second block a weight of 6500 g mol^{-1}. The block ratio is compared to that reported by H^1 NMR spectroscopy. Using the ratio of the integrals of the O-CH_2- protons for the DMAEMA and BMA blocks, the DP of the DMAEMA block can be calculated based on that reported for the BMA block, see figure 5.11. A DMAEMA: BMA ratio of 1:2.53 gives a DP of 37 for the DMAEMA block (5800 g mol^{-1}).

CHN analysis (CE 440 Elemental Analyser with thermal conductivity detector - Warwick Analytical Services Ltd) confirms this block ratio; GPC/NMR reported a C, H and N weight percentage of 65, 10 and 3%, respectively, whilst CHN analysis reported 66, 10 and 3%. Differential scanning calorimetry (DSC 1 STARe

system) reported a glass transition temperature of 20.67 – 24.60 °C (onset-mid), in agreement with that reported in literature (figure 5.12). Two heating cycles and one cooling cycle were carried out (-25 to 100°C) at a rate of 2 K min^{-1} with 25 minute isotherms. The nitrogen flow rate was 40 mL min^{-1}.

5.4.2 Microfluidic Device Construction and Capsule Formation

5.4.2.1 Materials

Standard wall borosilicate glass capillaries (GC100-10, OD 1.0 mm, ID 0.58 mm and GC200-7.5, OD 2.0 mm, ID 1.16 mm) were purchased from Harvard Apparatus. Clear Tygon tubing (0.8 mm ID) was purchased from Cole Parmer. Evo-Stik Two Part epoxy resin was applied to seal the capillaries where necessary. Solutions were introduced to the microfluidic device through the tubing attached to syringes driven by positive displacement syringe pumps (Harvard Apparatus, PHD 2000 series). Weller Dispensing Needles KDS3012P (GA 30, ID 0.15 mm) and KDS1812P (GA 18, ID 0.97 mm) were used to introduce the inner phase and outer/intermediate phases, respectively).

5.4.2.2 Preparation of Capsules by Microfluidics

A glass capillary with an inner and outer diameter of 1.16 mm and 2.0 mm, respectively, forms the outer casing of the device and contains the flow of the outer phase (see figure 5.13). For these studies, a 5 wt. % PVA aqueous solution is used to provide additional stabilisation during capsule formation. Within this, two capillaries with inner and outer diameters of 0.58 mm and 1.0 mm, respectively, were tapered with a laser puller to allow flow focusing of the middle organic phase (injection to 110 μm and collection to 120 μm). These tapered capillaries were aligned to create a flow-focused junction where double droplets are formed (see figure 5.14). A 5 mg cm^{-3} solution of $p(BMA)_{94}$-*b*-$p(DMAEMA)_{37}$ in chloroform is used as a volatile intermediate phase. Upon evaporation of the chloroform, the amphiphilic copolymer self-assembles into capsules. In the case

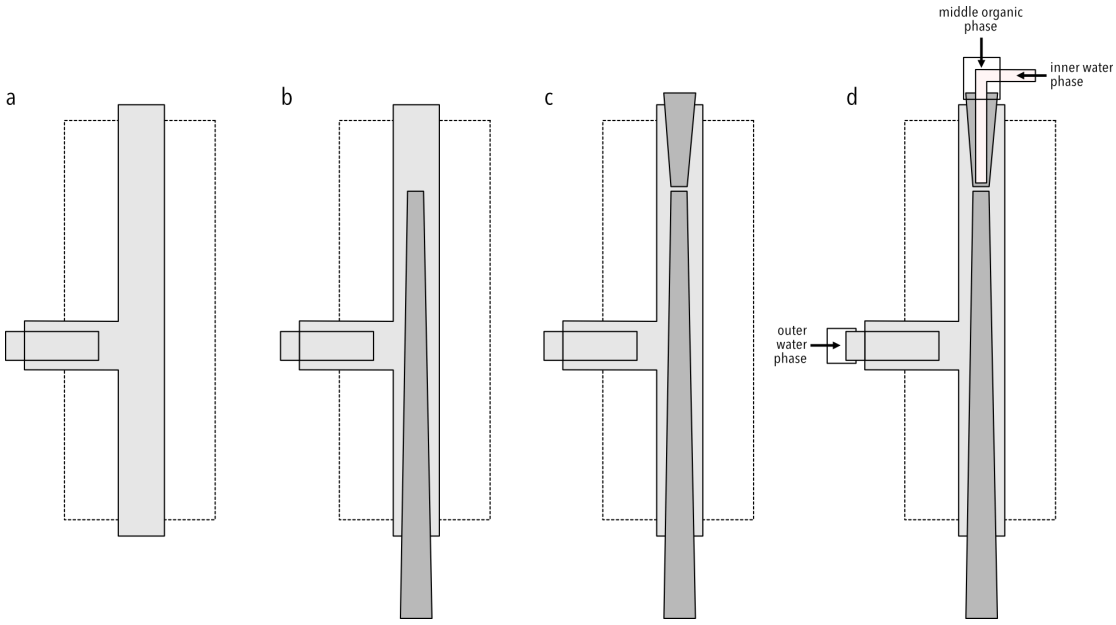

Figure 5.13 | The assembly of a microfluidic device, from left to right, a-d (a) creation of outer phase channel (b) insertion of the flow focused collection capillary (c) insertion of the flow focused middle phase capillary (d) insertion of the inner phase needle through the middle phase feed tube.

of particle embedded capsules, an additional 6 mg cm^{-3} of manganese oxide particles is added to the intermediate phase and the solution ultra-sonicated to disperse the particles. The inner phase, a 0.2 mol dm^{-3} sodium fluoride, 0.2 mol dm^{-3} sodium sulphate or 0.003 mol dm^{-3} congo red solution, is introduced at the junction via a 0.15 mm ID dispensing needle. Optimum flow rates for capsule synthesis were 0.15 mL min^{-1} for the outer phase, 0.005 mL min^{-1} for the middle phase and 0.005 mL min^{-1} for the inner phase. Once formed by the device, capsules were collected in outer phase solution. The average inner and outer diameter of double emulsion droplets was 311 and 328 μm, respectively. 20 minutes of sample collection corresponds to a total of *ca.* 6000 capsules. The total surface area of this sample is 1.93 x 10^{-3} m^2 and the theoretical capsule wall thickness is 242 nm. Optical images of the produced objects were obtained by a Leica DM 2500M optical microscope and accompanying Nikon D5100 camera. Electron microscopy images were obtained on a Zeiss Supra 55VP electron microscope with an attached cryo-SEM unit. Cryo-SEM images show a wall thickness of 100-200 nm with

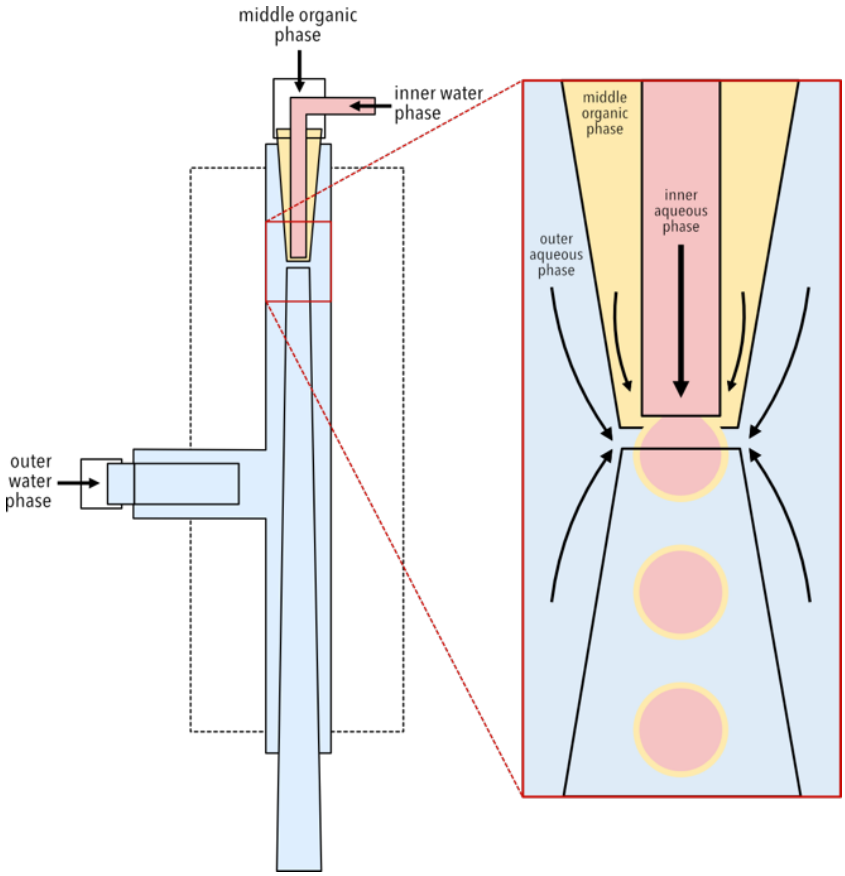

Figure 5.14 | Left A microfluidic device for the formation of monodisperse double droplets. An inner aqueous, middle organic and outer aqueous phase meet at a flow focused junction to form water- *in* – oil – *in* – water double droplets. **Right** The device is driven by three syringe pumps loaded with syringes and the outer phase is instated first. After wetting the capillary walls, the middle phase is switched on to generate single emulsion droplets. Finally, the inner phase is introduced to generate double-emulsion droplets.

manganese dioxide particles (*ca.* 1-2 μm) embedded in approximately a third of the capsule surface. Distribution of manganese dioxide particles is not uniform across all capsules due to a non-homogenous distribution of particles in the initial intermediate phase solution and the higher density of particles with respect to the solvent phase (causing movement during chloroform evaporation). Based on a theoretical unilamellar wall thickness of 22.4 nm (a bilayer formed from fully extended chains overlapping in their hydrophobic region), it is clear that a unilamellar structure is not formed. The capsule wall may be multilamellar or less ordered.

5.4.3 Release Measurements

5.4.3.1 Triggered release of sodium sulfate from capsules: visual release studies

A sample of sodium sulfate encapsulated capsules was added to a reservoir containing 1 cm^3 of 0.1 mol dm^{-3} barium chloride solution. The sample was placed under the Leica DM 2500M optical microscope and capsule rupture was observed following the addition of 0.1 cm^3 of 30 wt. % hydrogen peroxide solution; upon catalytic reaction of the embedded manganese oxide particles with peroxide in the continuous phase, oxygen bubbles start to form rapidly. These oxygen bubbles disrupted the membrane sufficiently enough to cause capsule collapse, as demonstrated by the video that accompanies paper DOI: 10.1039/C5MH00093A. Upon capsule rupture, a white crystal precipitate of barium sulfate is formed following the reaction of sodium sulfate and barium chloride.

5.4.3.2 Triggered release of sodium fluoride from capsules: quantitative release studies

Samples of capsules loaded with sodium fluoride solution (at a fluoride ion concentration of 3800 ppm) were prepared following the procedure outlined in section 5.4.2.2. A sample of capsules collected after 20 minutes of microfluidic device output (a total inner volume of 0.1 cm^3) was collected into 3 cm^3 of outer phase solution. During collection and the first hour of each experiment, capsules were agitated in solution to prevent destabilization caused by prolonged contact with each other during the chloroform evaporation stage. This was achieved by circulating the outer phase solution at the location of the capsules. Agitation was continued throughout the experiment. To prevent an imbalance of osmotic pressure across the capsule wall, sodium chloride is added to the outer phase at a chloride ion concentration of 3800 ppm. Changes in the fluoride ISE response in the outer phase solution were measured over a period of 900 minutes; following a calibration of the ISE with fluoride ion standards, the fluoride ion concentration

in the outer phase is calculated. After this time, the sample is sonicated and the capsules ruptured, allowing for a 100 % release value to be calculated. This procedure was followed for capsules with and without manganese oxide particles in their walls in the absence of a hydrogen peroxide trigger. Capsules with manganese oxide particles in their walls were then treated with hydrogen peroxide triggers. 3.0 cm^3 of 30 wt. % hydrogen peroxide was added to a sample of capsules at 50 minutes resulting in rapid capsule rupture and 100 % release after 64 minutes. Temporary increases in fluoride ion release were triggered by 0.2 cm^3 additions of 3 wt. % hydrogen peroxide at 150, 250 and 340 minutes. Capsules were monitored for changes in size after triggered release. 3 hours after the addition of a 0.3 wt. % hydrogen peroxide trigger, the capsule wall thickness appeared to have increased by *ca.* 4μm. After two more identical triggers and 24 hours, the capsules' shape and size varied (see figure 5.15), likely due to oxygen bubbles trapped at the capsule surface.

5.4.3.3 Triggered release of congo red dye from capsules: quantitative release studies

Samples of particle-embedded capsules loaded congo red solution were prepared following the procedure outlined in section 5.4.2.2. A sample of capsules collected after 20 minutes of microfluidic device output (a total inner volume of 0.1 cm^3) was collected into 3 cm^3 of PVA outer phase solution. Capsules were agitated as

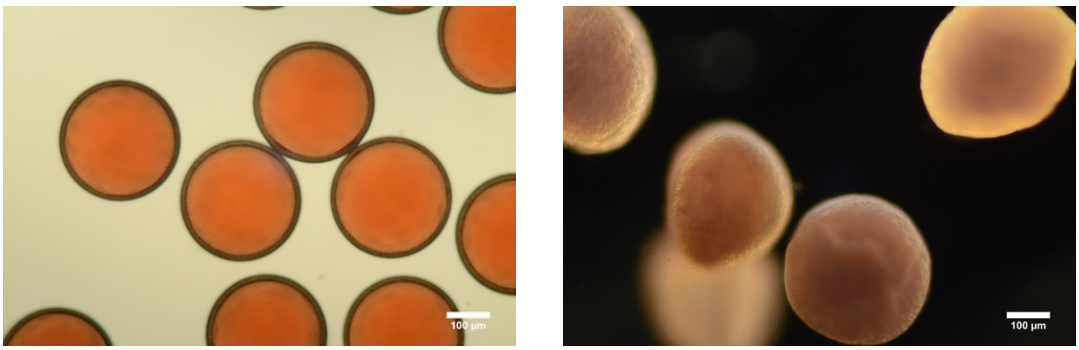

Figure 5.15 | Left: Congo red loaded capsules embedded with manganese oxide particles before three 3 wt. % hydrogen peroxide triggers; Right: capsules 24 hours after.

before. Over a period of *ca.* 1300 minutes, 1 cm^3 aliquots of the outer phase were removed from the sample and their UV-Vis spectra measured over the wavelength range of 200-850 nm. After each measurement, the aliquots were returned to the sample. For each sampling point, the concentration of congo red dye was calculated. Given the known molar extinction coefficient of 2500 L mol^{-1} cm^{-1} and path length of 1 cm, the Beer-Lambert law was used to plot a calibration curve by taking the absorbance value of the wavelength maximum, 505 nm, of congo red. From this plot and the absorbance values of each sampling point, congo red concentration is calculated. Percentage of dye release is calculated by comparison of concentration at a given time and after total release (based on initial capsule loading).

5.4.4 Quantification of manganese by Inductively Coupled Plasma – Optical Emission Spectroscopy (ICP-OES) detection

Samples of capsules monitored in the release studies have a total manganese concentration of 69358 ppb after the addition of three 0.2 cm^3 3 wt. % hydrogen peroxide triggers. This value is taken as the expected outer phase manganese concentration if 100 % of particles became dissociated with the membrane on application of the trigger (assuming particles only fell into the outer phase, not the inner phase). After the application of the triggers to the sample, elemental manganese content in the outer phase was determined by ICP-OES. This technique has a lower limit of detection of 25 ppb; a required solid content of < 0.1 % for analysis made a sample dilution necessary, increasing the limit of detection to 1250 ppb. Results indicated that the concentration of manganese in the outer phase was indistinguishable from that of the manganese-free blanks. The loss of manganese (IV) oxide to the outer phase from the capsules was therefore ≤ 1.8 %, with respect to the manganese (IV) oxide particles embedded in the capsule walls.

5.4.5 Confocal Microscopy

Congo Red loaded polymer capsules were observed with a confocal laser scanning microscope (Leica TCS SP5, Leica Microsystems). Figure 5.9 (512 x 512 pixels, 8-bit pixel depth, 4.0x digital zoom, 32 line average) was acquired on a Leica DMI6000 microscope using a HC PL FLUOTAR 10.0x 0.30 dry objective lens, at a scan speed of 8000 Hz. Congo red was visualised using an argon laser (λ = 504 nm, 30 % intensity) with a spectral detection window of 560 – 671 nm. Data was collected and analysed using the Leica LAS-AF8 confocal acquisition software.

5.5 References

1 J. N. Israelachvili, *Intermolecular and surface forces*, Academic Press, Cambridge, MA, 2011.

2 D. E. Discher and A. Eisenberg, *Science*, 2002, **297**, 967–973.

3 J. N. Israelachvili, D. J. Mitchell and B. W. Ninham, *Biochim. Biophys. Acta - Biomembr.*, 1977, **470**, 185–201.

4 M. P. Sheetz and S. J. Singer, *Proc. Natl. Acad. Sci. U. S. A.*, 1974, **71**, 4457–4461.

5 J. N. Israelachvili and D. J. Mitchell, *Biochim. Biophys. Acta*, 1975, **389**, 13–19.

6 R. Egel, D.-H. Lankenau and A. Y. Mulkidjanian, *Origins of life : the primal self-organization*, Springer, 2011.

7 S. J. Singer and G. L. Nicolson, *Science*, 1972, **175**, 720–731.

8 C. Nardin, S. Thoeni, J. Widmer, M. Winterhalter and W. Meier, *Chem. Commun.*, 2000, **0**, 1433–1434.

9 M. Kumar, M. Grzelakowski, J. Zilles, M. Clark and W. Meier, *Proc. Natl. Acad. Sci. U. S. A.*, 2007, **104**, 20719–20724.

10 H.-J. Choi and C. D. Montemagno, *Nano Lett.*, 2005, **5**, 2538–2542.

11 A. Graff, M. Sauer, P. Van Gelder and W. Meier, *Proc. Natl. Acad. Sci. U. S. A.*, 2002, **99**, 5064–5068.

12 A. J. Kim, M. S. Kaucher, K. P. Davis, M. Peterca, M. R. Imam, N. A.

Christian, D. H. Levine, F. S. Bates, V. Percec and D. A. Hammer, *Adv. Funct. Mater.*, 2009, **19**, 2930–2936.

13 M. Danial, C. M.-N. Tran, K. A. Jolliffe and S. Perrier, *J. Am. Chem. Soc.*, 2014, **136**, 8018–8026.

14 N. Madhavan, E. C. Robert and M. S. Gin, *Angew. Chemie Int. Ed.*, 2005, **44**, 7584–7587.

15 D. Papahadjopoulos, K. Jacobson, S. Nir and I. Isac, *Biochim. Biophys. Acta - Biomembr.*, 1973, **311**, 330–348.

16 M. B. Yatvin, J. N. Weinstein, W. H. Dennis and R. Blumenthal, *Science*, 1978, **202**, 1290–1293.

17 J. Gaitzsch, D. Appelhans, L. Wang, G. Battaglia and B. Voit, *Angew. Chemie Int. Ed.*, 2012, **51**, 4448–4451.

18 A. Napoli, M. Valentini, N. Tirelli, M. Müller and J. A. Hubbell, *Nat. Mater.*, 2004, **3**, 183–189.

19 A. Napoli, M. J. Boerakker, N. Tirelli, R. J. M. Nolte, N. A. J. M. Sommerdijk and J. A. Hubbell, *Langmuir*, 2004, **20**, 3487–3491.

20 F. Ahmed and D. E. Discher, *J. Control. Release*, 2004, **96**, 37–53.

21 J. Du and S. P. Armes, *J. Am. Chem. Soc.*, 2005, **127**, 12800–12801.

22 S. Yu, T. Azzam, I. Rouiller and A. Eisenberg, *J. Am. Chem. Soc.*, 2009, **131**, 10557–10566.

23 K. T. Kim, J. J. L. M. Cornelissen, R. J. M. Nolte and J. C. M. van Hest, *Adv. Mater.*, 2009, **21**, 2787–2791.

24 B. G. De Geest, S. De Koker, J. Demeester, S. C. De Smedt and W. E. Hennink, *Polym. Chem.*, 2010, **1**, 137–148.

25 S.-H. Park, S.-G. Oh, J.-Y. Mun and S.-S. Han, *Colloids Surf., B*, 2005, **44**, 117–122.

26 S.-H. Park, S.-G. Oh, J.-Y. Mun and S.-S. Han, *Colloids Surf., B*, 2006, **48**, 112–118.

27 L. Paasonen, T. Laaksonen, C. Johans, M. Yliperttula, K. Kontturi and A. Urtti, *J. Control. Release*, 2007, **122**, 86–93.

28 E. Amstad, S.-H. Kim and D. A. Weitz, *Angew. Chemie Int. Ed.*, 2012, **51**, 12499–12503.

29 S. Lecommandoux, O. Sandre, F. Chécot, J. Rodriguez-Hernandez and R. Perzynski, *Adv. Mater.*, 2005, **17**, 712–718.

30 S. Lecommandoux, O. Sandre, F. Chécot and R. Perzynski, *Prog. Solid State Chem.*, 2006, **34**, 171–179.

31 M. Krack, H. Hohenberg, A. Kornowski, P. Lindner, H. Weller and S. Förster, *J. Am. Chem. Soc.*, 2008, **130**, 7315–7320.

32 C. Sanson, O. Diou, J. Thévenot, E. Ibarboure, A. Soum, A. Brûlet, S. Miraux, E. Thiaudière, S. Tan, A. Brisson, V. Dupuis, O. Sandre and S. Lecommandoux, *ACS Nano*, 2011, **5**, 1122–1140.

33 E. Amstad, J. Kohlbrecher, E. Müller, T. Schweizer, M. Textor and E. Reimhult, *Nano Lett.*, 2011, **11**, 1664–1670.

34 Y. Chen, A. Bose and G. D. Bothun, *ACS Nano*, 2010, **4**, 3215–3221.

35 W. Seifriz, *J. Phys. Chem.*, 1925, **29**, 738–749.

36 S. Higashi and T. Setoguchi, *Adv. Drug Deliv. Rev.*, 2000, **45**, 57–64.

37 S. Okushima, T. Nisisako, T. Torii and T. Higuchi, *Langmuir*, 2004, **20**, 9905–9908.

38 I. G. Loscertales, A. Barrero, I. Guerrero, R. Cortijo, M. Marquez and A. M. Gañán-Calvo, *Science*, 2002, **295**, 1695–1698.

39 A. S. Utada, E. Lorenceau, D. R. Link, P. D. Kaplan, H. A. Stone and D. A. Weitz, *Science*, 2005, **308**, 537–541.

40 L. Brown, S. L. McArthur, P. C. Wright, A. Lewis and G. Battaglia, *Lab Chip*, 2010, **10**, 1922–1928.

41 R. K. Shah, H. C. Shum, A. C. Rowat, D. Lee, J. J. Agresti, A. S. Utada, L.-Y. Chu, J.-W. Kim, A. Fernandez-Nieves, C. J. Martinez and D. A. Weitz, *Mater. Today*, 2008, **11**, 18–27.

42 A. Jahn, J. E. Reiner, W. N. Vreeland, D. L. DeVoe, L. E. Locascio and M. Gaitan, *J. Nanoparticle Res.*, 2008, **10**, 925–934.

43 G. Wächtershäuser, *Syst. Appl. Microbiol.*, 1988, **10**, 207–210.

44 G. Wächtershäuser, *Proc. Natl. Acad. Sci.* , 1994, **91**, 4283–4287.

45 M. J. Russell, A. J. Hall, A. G. Cairns-Smith and P. S. Braterman, *Nature*, 1988, **336**, 117.

46 I. A. Chen, R. W. Roberts and J. W. Szostak, *Science*, 2004, **305**, 1474–1476.

47 J. C. Blain and J. W. Szostak, *Annu. Rev. Biochem.*, 2014, **83**, 615–640.

48 A. Y. Mulkidjanian and M. Y. Galperin, *Biol. Direct*, 2009, **4**, 27.

49 A. D. Dinsmore, M. F. Hsu, M. G. Nikolaides, M. Marquez, A. R. Bausch and D. A. Weitz, *Science*, 2002, **298**, 1006–1009.

50 S. U. Pickering, *J. Chem. Soc., Trans.*, 1907, **91**, 2001–2021.

51 D. W. Deamer, *Nature*, 2008, **454**, 37–38.

52 S. S. Mansy, J. P. Schrum, M. Krishnamurthy, S. Tobé, D. A. Treco and J. W. Szostak, *Nature*, 2008, **454**, 122–125.

53 S. S. Mansy and J. W. Szostak, *Proc. Natl. Acad. Sci. U. S. A.*, 2008, **105**, 13351–13355.

54 R. N. Keller, H. D. Wrcoff and L. E. Marchi, *Inorganic Syntheses, Volume 2*, John Wiley & Sons, Inc., 1946.

55 D. M. Haddleton, M. C. Crossman, B. H. Dana, D. J. Duncalf, A. M. Heming, D. Kukulj and A. J. Shooter, *Macro*, 1999, **32**, 2110–2119.

6 Functions and applications of particle - vesicle composites

6.1 Introduction

Vesicles, microscopic sacs that enclose finite volumes of aqueous liquids by thin membranes, have existed since the very first protocells, these being self-assembled lipid-based structures that are considered to be the stepping stone to the origin of life and the predecessor to modern cells.[1–4]

In nature, the membranes of vesicles and cells are composed of phospholipid amphiphiles. These amphiphiles contain both a hydrophilic and hydrophobic domain which allows them be assembled into bilayer-type spherical structures.[5]

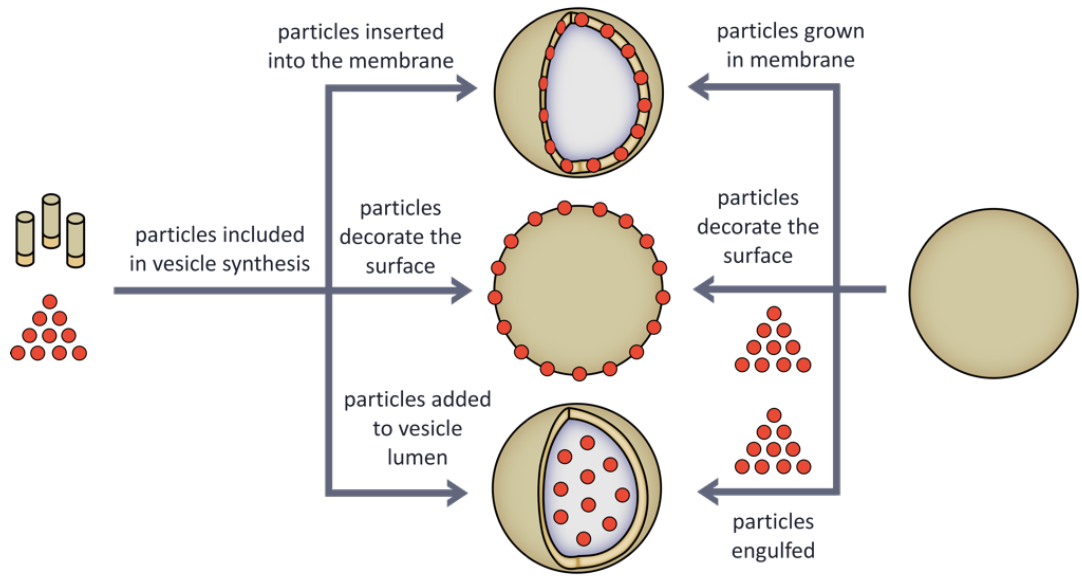

Figure 6.1 | The various routes towards particle-vesicle composite structures. Particles can be included in the vesicle synthesis to generate vesicles containing particles in their walls, on their surfaces or inside of their lumens (the vesicle core). Alternatively, particles can be added to pre-formed vesicles to generate the same three structures.

Their membranes are composed of an inner hydrophobic region surrounded by outer hydrophilic domains that face the inner and outer aqueous environments in which the vesicle can be found.[6]

Vesicles can also be formed artificially by the spontaneous assembly of amphiphilic building blocks under appropriate solvent conditions, given that the ratio between the hydrophilic and hydrophobic domains is appropriate.[7–9] These building blocks can be either natural or synthetic, namely lipids or di-block copolymers, and their corresponding structures are known as *liposomes* or *polymersomes*, respectively.

Many reviews consider the development and importance of liposomes and polymersomes, and the reader is referred to these sources for further information.[6,10–13] Instead of solely focusing on vesicles, this review will take a look at a range of functions that particles have brought to vesicles, considering the interactions between the two building blocks and how new behaviours can be derived from the pairing of particles and vesicles (the possibilities of which are summarised in figure 6.1).

Particles, here defined as localised objects smaller than the vesicle with which they are associated, find use in a wide range of applications, such as catalysis,[14,15] drug delivery,[16,17] pigments,[18] nanoswimmers[19,20] and rheology modifiers.[21] Particles can be immobilised within a passive support such as a vesicle, whether that be as part of their walls, on their surface or inside the vesicle core, to deliver new hybrid behaviours that neither the particle or vesicle possess alone.

At over 100 publications to date, particles and vesicles have been combined in a plethora of ways, tackling a wide range of chemical, biological and physical problems. This review will assess the importance and novelty of a number of examples with a selection of different applications.

6.2 The beginnings of composite vesicles: functional liposomes

Artificial liposomes were first synthesised in 1963 by Bangham,[22] but the first mention of combining particles with vesicles was not reported until 1978 by Williams *et al.*[23] In this work, cobalt sulfide particles are grown inside of phosphatidylcholine vesicles 25 nm in diameter and used as inorganic probes to track vesicles. The following year,[24] similar experiments demonstrated the inclusion of magnetite (Fe_3O_4) into these vesicles, however these particles are grown prior to vesicle formation. Due to the limitations of microscopy technology, the precise location of magnetite particles is unknown, however this experiment is the first example of particles being included in a vesicle synthesis. Even as early as 1979, the authors recognised the potential use of these vesicles as magnetic drug carriers. In 1983, Margolis *et al.* demonstrated the association of ferromagnetic ferrite particles (50 nm in diameter) with liposomes bearing anti-fibronectin antibodies capable of binding to mouse embryo fibroblasts.[25] Upon binding the so called *magnetoliposomes*, the cells could be sorted using a magnetic field. This study demonstrates how combining the behaviour of a biologically interfacing vesicle with that of functional nanoparticles can generate new materials.

In the same year, Hong *et al.* showed that gold nanoparticles could be associated with liposomes, this time internalised.[26] These 15 nm gold particles were used as a histological marker to track the uptake and endocytosis of liposomes into cells, useful in electron microscopy due to their high electron density, size and shape uniformity. Colloidal iron (1-5 nm particles) was later used by Mezei *et al.* for the same reasons to monitor liposome-cell interactions.[27]

These early studies focused on combining the capabilities of particles and vesicles to tackle specific, biological problems. Though several authors published similar studies around this period,[28–30] such as the growth of silver oxide crystals in vesicles[31] or the growth of cadmium sulfide particles in and on vesicles,[32,33] their characterisation of composite vesicles was still limited.

With the advent of vesicles formed from synthetic block-copolymers in 1995 by Eisenberg *et al.*,[34] coined *polymersomes* in 1999,[10] came more robust synthetic vesicles capable of more severe modifications to their structures.[6] This, along with advancements in electron microscopy (higher resolution and cryogenic techniques, for example) resulted in a number of composite vesicles with a range of new functions and behaviours that could be properly characterised.

In this review, we focus on four ways that particles are able to change the behaviour of lipid or polymer vesicles, namely: the stabilisation of vesicles by particles, shape changes in vesicles, the moderation of membrane permeability and taxis of vesicles using particles.

6.3 Stabilisation of vesicles by particles

As vesicles are composed of fluid bilayers, they can be unstable and often have a tendency to flocculate and fuse with one another.[35,36] Traditionally, vesicles can be stabilised by incorporating polyethylene glycol modified lipids into their membranes,[37–39] or by adsorbing polyelectrolytes onto their surfaces,[40,41] to provide steric stabilisation. Particles can also adsorb to and decorate vesicle surfaces,[42–47] providing stabilisation in the form of repulsive electrostatic interactions between the vesicle and nanoparticles in some cases. These particles can be polymer latexes,[48–50] silica,[51,52] gold[53] and even hydrogels particles.[54] As always, nature has led the way. For example, bacteria can coat themselves with S-layer proteins,[55] and coccolithophorids (a eukaryotic phytoplankton) have a $CaCO_3$-based nano-patterned colloidal armour.[56]

Back in 1999, Weitz *et al.* demonstrated that arrays of negatively microspheres could be assembled onto the outside of positively charged mixed bilayer vesicles, thus forming two-dimensional crystals in adhesive zones of the vesicle only.[57,58]

Zhang *et al.* later showed that if carboxyl modified gold nanoparticles are adsorbed to the outer surface of phospholipid liposomes they can control their fusion

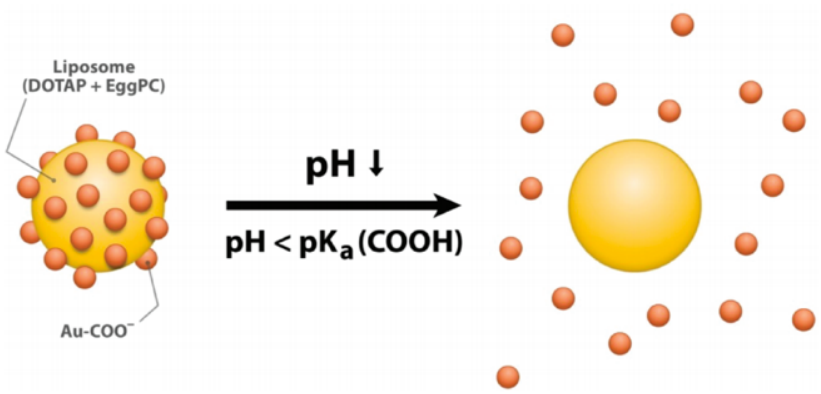

Figure 6.2 | Schematic illustrations of a carboxyl-modified gold nanoparticle (AuC)-stabilised liposome and its destabilisation at acidic pH. The liposome is stabilised by deprotonated gold particles (Au-COO$^-$) at neutral pH. When the pH drops below the pK_a value of the carboxylic group (pK_a = *ca.* 5), Au-COO$^-$ nanoparticles are protonated to form Au-COOH, which subsequently detach from the liposome, resulting in the formation of a bare liposome with fusion activity resuming. Reproduced with permission from Zhang *et al.*[53]

activity.[53] As shown in figure 6.2, at neutral pH, gold nanoparticles, *ca.* 4 nm diameter, are bound to the surface of 1,2-di-(9Z-octadecenoyl)-3-trimethylammonium propane (DOTAP) vesicles. Liposomes are stabilised whilst the pH is above the pK_a of the gold's surface carboxylic acid groups (Au-COO$^-$), but below it (p$K_a \approx 5$), the nanoparticles are protonated (Au-COOH), causing them to detach from the liposome. The subsequent destabilisation of liposomes causes them to fuse with one another. The concept of acid-responsive vesicles could be of use in transdermal drug delivery, as human skin is acidic, especially when infected.[59] One can imagine vesicles that are triggered to fuse and release their contents when in contact with such an acidic surface, delivering medicinal or therapeutic payloads.

Here in the *BonLab*, we demonstrated the assembly of polymeric and silica spheres onto the assembly of poly(*n*-butyl methacrylate)-*b*-(2-(dimethylamino) ethyl methacrylate) vesicles, to produce armours that we observe with cryogenic scanning electron microscopy.[42]

A further notable example includes that by Gradzielski *et al.*, who showed that 100 nm zwitterionic dipalmitoylphosphatidylcholine (DPPC) lipid vesicles below their glass transition temperature (i.e. in a soft/liquid state) can be effectively stabilised by negatively charged silica nanoparticles. This study is particularly interesting because particle concentration appears to play a key role in determining vesicle stability.[52] Small amounts of surface-adsorbed silica nanoparticles, in this case Ludox® HS 40 *ca.* 16 nm in diameter, initially leads to enhanced flocculation, whilst higher concentrations make the vesicles more negatively charged and stable for a longer period of time. This stability is shown to be optimum at neutral pH and at a low ionic strength. The reason why a low particle concentration induces flocculation is somewhat unclear, however the authors speculate that at low concentrations, particles bridge between vesicles, causing them to be brought into close contact whilst still in an unstable state.

Interestingly, local membrane bending is observed where nanoparticles adsorb. As silica particles are adhered to the vesicle membrane below the phase transition

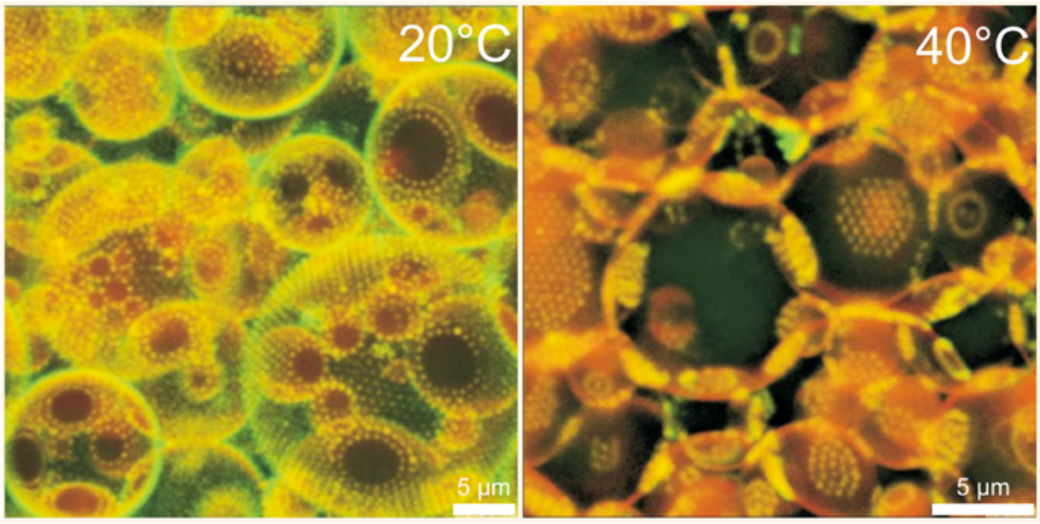

Figure 6.3 | Fluorescence confocal micrographs of giant lipid vesicles decorated with thermoresponsive PNIPAM microgels at 20 °C (left) and above the PNIPAM volume phase temperature transition at 40 °C (right). Reproduced with permission from Nylander *et al.*[54]

temperature of DPPC, indents are made and appear to be retained in the cooling process.

A beautiful example of an entirely soft composite system comes from Nylander *et al.*, who show that 1,2-dioleoylsn-glycero-3-phosphocholine (DOPC) vesicles can be stabilised by thermoresponsive poly(N-isopropylacrylamide) (PNIPAM) particles, as shown in figure 6.3.[54] Responsive polymers that undergo volume phase transitions can be particularly useful as building blocks for self-assemblies,[60,61] as they can adapt their conformation and interactions to their environments.[62–67] Just like their solid-core counterparts, cross-linked polymer particles can act as Pickering stabilisers at interfaces,[68,69] and PNIPAM particles are no exception. As these microgel particles exhibit a reversible volume phase transition in water around 32 °C, their stabilising efficiency can be controlled as a function of temperature. Below their phase transition the particles stabilise DOPC vesicles, as they behave as soft particles with a 'fuzzy' surface. They adsorb on the vesicle surface forming densely packed 2D hexagonal arrays across the surface. Above the phase transition temperature, the particles contract into hard spheres, altering the vesicle membrane-microgel interactions and causing microgels to instead rearrange into domains at the vesicle interface (similar to the aforementioned two-dimensional crystal formed on vesicles surfaces by Weitz *et al.*). The authors propose that this is because the microgel particles become smaller, harder, and more hydrophobic, thus creating depletion zones. This demonstrates that the softness and deformability of the particles is crucial for interactions between the particles and the membrane. Again, stabilisation by particles prevents fusion of the vesicles and offers a trigger that could be used in the delivery of active agents by means of a temperature change that induces vesicle rupture.

6.4 Shape changes in vesicles

In these examples of vesicle stabilisation by particles, we have neglected to consider the physical relationship between a hard sphere and a soft elastic membrane.[70] When a particle interacts with a vesicle membrane, whether that be

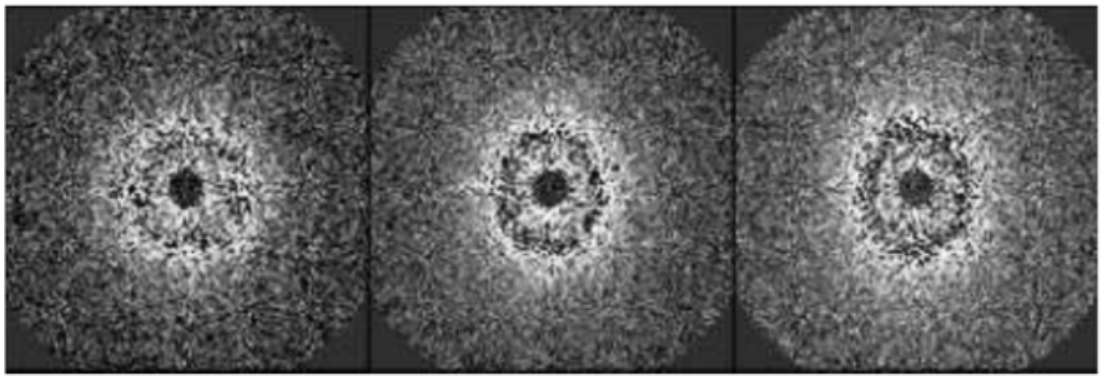

Figure 6.4 | Deformation of the hollow magnetic shells of vesicles proven by the anisotropy of the 2D small-angle neutron scattering (SANS) patterns under a horizontal magnetic field of intensity B = 0 G (left), B = 540 G (middle) and B = 1050 G (right). Reproduced with permission from Lecommandoux *et al.*[81]

on the inner or outer surface, it can deform the vesicle to induce a range of interesting shape changes. Both local deformation of the membrane by a particle and the impact on vesicle shape by particles collectively have been studied experimentally[52,71–74] and theoretically.[75–80]

Lecommandoux *et al.* directly observed incorporation of particles in the vesicle membrane,[81–83] when magnetite nanoparticles (7.6 nm in diameter) were loaded into the walls of amphiphilic poly-butadiene-*block*-poly(glutamic acid) di-block copolymer vesicles, either 208 or 624 nm in diameter. The application of a magnetic field allows the shape of the vesicle to be modified, even at relatively low magnetic field intensities (B = 290 G), as shown in figure 6.4.

Instead of embedding particles into the membrane walls, they can be loaded into the lumen (interior) of the vesicle in order to manipulate its structure, as demonstrated by Orwar *et al.*[84] As figure 6.5 shows, 20 nm CdSe/CdTe (core/shell) nanocrystals can induce tubulation of flat giant unilamellar vesicles (FGUVs) formed from the spreading of *ca.* 20 μm multilamellar soybean lipid vesicles. By encapsulating these particles inside of the vesicle and introducing low concentrations of calcium ions (1-4 mmol dm^{-3}), transient tubes several hundred micrometres in length were formed, analogous to biological nanotubes that fulfil

important functions within cells (such as signalling and transport). The authors theorised that these tubes form because of a mismatch between the inner and the outer monolayers of the upper FGUV bilayer, resulting in spontaneous curvature changes.

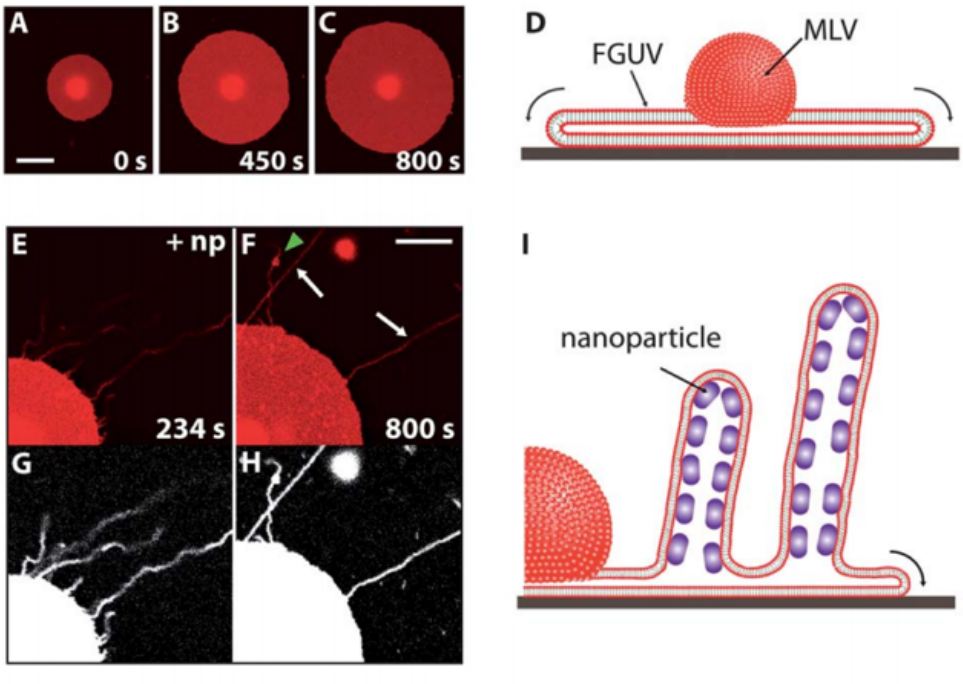

Figure 6.5 | Spreading and transient tubulation in flat giant unilamellar vesicles (FGUVs) in 2 mM Ca^{2+} containing buffer solution. (A–C) Fluorescence micrograph time series of a FGUV which does not contain nanoparticles and spreads circularly on SiO_2. Scale bar: 20 μm. (D) Schematic drawing of the profile of the FGUV in (A–C) spreading out the lipid material from the multilamellar vesicles (MLV) onto the solid support. Arrows indicate the motion of the rolling bilayer. (E) Fluorescence micrograph of the spreading edge of a nanoparticle encapsulating FGUV, which is displaying transient tubulation while circularly spreading on SiO_2. (F) Fluorescence micrograph of the FGUV at 800 s, when the tubes had retracted into the FGUV. The remaining tubes in (F) became immobilised onto the surface. The green arrow in (F) shows the immobilised end of one tube. Scale bar: 40 mm. (G, H) False coloured black and white images of (E,F). (I) Schematic drawing showing the profile of the FGUV in (E–H). Structures in the tubes represent the nanoparticles (20 nm in diameter). Arrow indicates the motion of the rolling bilayer. Reproduced with permission from Orwar *et al.*[84]

In contrast, Imai *et al.* confined charged colloidal particles into non-spherical vesicles at much higher volume fractions (≈ 0.5), transforming them into multi-bead vesicles upon an osmotic pressure difference, as shown in figure 6.6.[85] As the vesicle volume is reduced due to loss of water, preservation of surface area results in an increase in excess area. This excess area leads to non-spherical shapes such as tubes, discocytes or stomatocytes. Packing of particles inside the vesicles transforms them into multi-bead vesicles, in order to obtain the largest free volume for the encapsulated colloids. In considering the shape deformation pathways of these vesicles, the authors theorise that the repulsive interaction between colloids might induce the observed transitions.

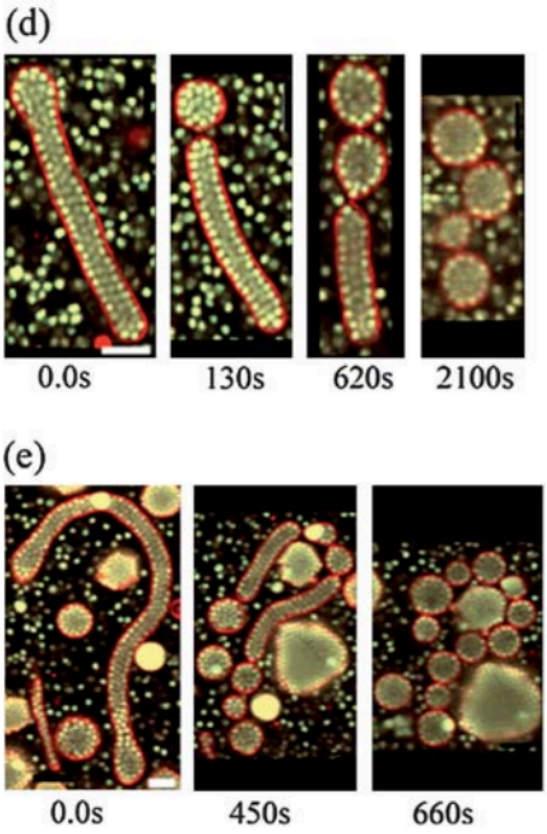

Figure 6.6 | Shape deformation pathways of giant vesicles encapsulating dense colloids upon the application of an osmotic pressure difference, in the case of (d) medium and (e) long tubes. Reproduced with permission from Imai *et al.*[85]

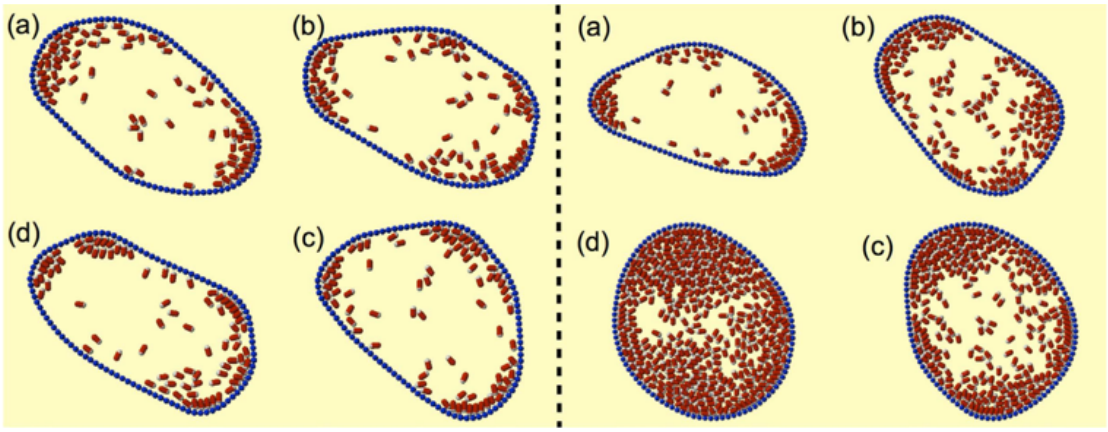

Figure 6.7 | Shape fluctuations of a vesicle where the bounding membrane is composed of $N_b = 100$ beads, and the vesicle contains active swimmers **Left panel:** snapshots of vesicle shapes explored by the active vesicle for low packing fraction of elongated swimmers ($\varphi = 0.16$). **Right panel:** the vesicle becomes more symmetric as the number of active particles increases, φ is 0.16 (a), 0.31 (b), 0.51 (c) and 0.76 (d). Reproduced with permission from Angelani *et al.*[86]

Angelani *et al.* theorised that filling vesicles with active particles can also lead to interesting behaviours, as shown in figure 6.7.[86] In their computational study, swimming particles accumulate leading to pinched spots of high density, curvature and pressure. Local fluctuations of particle density produce a local pressure increase that induces a larger curvature on the flexible membrane. Since active particles tend to accumulate at concave boundaries, this local curvature increase drives further accumulation of swimmers, which in turn raises the local pressure. When vesicle packing is sufficiently high, however, the particles cover the inner membrane uniformly, leading to more consistent pressure and curvature.

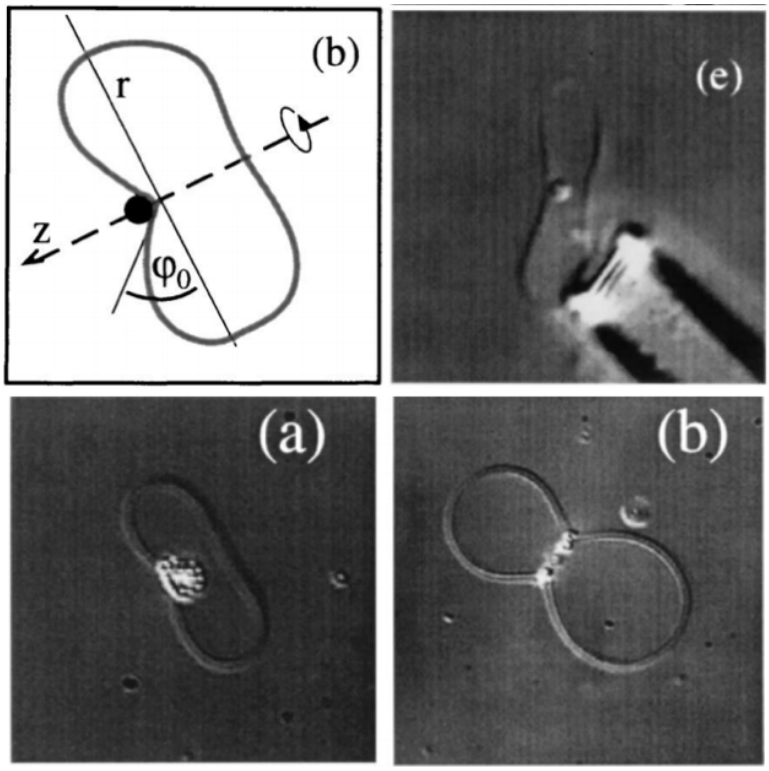

Figure 6.8 | Top: (b) Schematic of a pinched, hat-like membrane deformation around a bead, observed practically with a single bead on a vesicle in (e). **Bottom:** (a) Phase separation of many beads into a condensed hexagonal packed cluster. The cluster is located at the concave dip of a stomatocyte shaped liposome. (b) Beads clustered in a ring form around the waist of a dumbbell shaped multilamellar vesicle. Reproduced with permission from Safinya *et al.*[87]

Conversely, particles sitting on the surface of vesicles can also induce radical shape changes, as shown in figure 6.8. Safinya *et al.* showed that particles can induce pinched shape deformations of the membrane of a vesicle, and, if a number are decorating a fluid membrane, can interact with one another.[87] Giant unilamellar 1-palmytoyl-2-oleoyl phosphocholine and dimiristoyl phosphocholine liposomes (*ca.* 10 μm in diameter) were decorated with protein grafted latex beads (0.9 μm in diameter). Vesicles with single beads attached clearly show induced contours around the bound bead, and interestingly, particles appear to be driven to negative curvature regions on non-spherical vesicles, the most energetically favoured conformation. When two beads are attached to spherical vesicles, there is no preferential location and the beads approach each other if lipid mobility is

preserved (i.e. above the lipid chain melting temperature). Critically, the beads do not aggregate freely in solution, thus their approach is not mediated by colloidal interactions alone. This collective particle behaviour can even generate ring shaped strings of beads around the waist of a dumbbell shaped vesicle, notable as the precursor to the budding and fission of membranes.

Sticking with the interaction of multiple beads on a vesicle surface, Cacciuto and Šarić computed a phase diagram for the different aggregates formed by nanoparticles adsorbing onto a lipid bilayer as a function of surface bending rigidity and nanoparticles adhesive energy, as shown in figure 6.9.[88] Over a wide range of bending rigidities (≈ 10 – 100 k_BT), nanoparticles can organize into linear aggregates, providing that the binding energy is sufficiently large. Similar to the experimental observations of Safinya *et al.*, particles can pinch around the circumference of a vesicle, this time into longer chains.

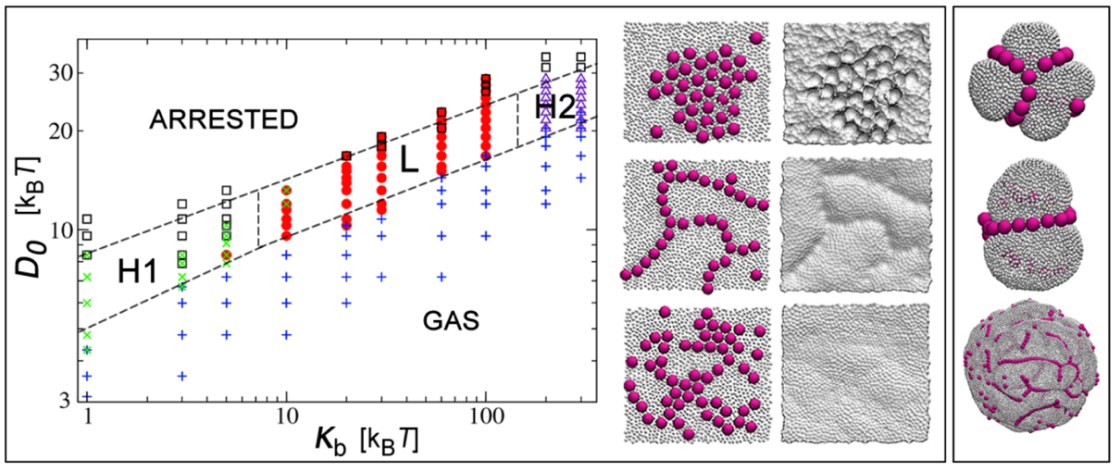

Figure 6.9 | Left panel: Phase diagram of particle self-assembly on a fluid surface in terms of the surface bending rigidity k_b and particle binding energy D_0. **Middle panel**: The snapshots show typical aggregates in the H_1, L, and H_2 phases in a top-to-bottom order and the deformation pattern they leave on the membrane. The membrane area is A ≈ (40 x 40)σ^2, the nanoparticle size σ_{np} = 4σ, and their surface fraction ϱ = 0.27. **Right panel:** Snapshots of the linear aggregates on the spherical membrane. Reproduced with permission from Cacciuto and Šarić.[88]

Finally, vesicles can engulf particles that adhere to their surfaces in a similar fashion to the cellular uptake termed *endocytosis*. During endocytosis, molecules adhered to the membrane, the bilayer invaginates and the target is completely wrapped in a newly formed vesicle.[89]

Several studies consider this process both theoretically and experimentally,[90–99] but we will focus on two noteworthy examples. The first from Kroeger *et al.* presents experimental evidence of the internalisation of particles by poly(dimethylsiloxane)-*block*-poly(2-methyloxazoline) vesicles, 110 nm in diameter.[94] Using photon- and fluorescence-correlation spectroscopy, the authors show species selective uptake dependent on particle size and concentration. A threshold concentration for particle uptake is shown, explained by the surface area ratio between polymersomes and particles necessary for successful particle adhesion to the membrane. Unsurprisingly, a higher concentration of nanoparticles leads to internalisation of more particles. Furthermore, size selectivity is seen. Loading incorporation rates decreases as the nanoparticle radius increases from 15, to 36 to 57 nm, but interestingly, cryo-TEM reveals that particles are engulfed via different mechanisms depending on their size. Smaller particles are engulfed as clusters instead of single wrapped particles, as in the case for the larger nanoparticles.

The phenomena of particle endocytosis by vesicles was also approached from a theoretical standpoint by Gao and Yi, where they consider the effects of particle size and elasticity on particle incorporation.[100] In this study, elastic particles of different sizes and rigidities are incorporated into a lipid vesicle of fixed surface area, whilst the size of the particle determines the mode of particle uptake. The incorporation of small particles leads to continuous vesicle volume evolution, as the vesicle undergoes a smooth shape transformation. Conversely, vesicles wrapping a large particle undergo a discontinuous shape transition from concave shallow bowl-shaped stomatocytes into almost closed cups. Furthermore, softer particles are more prone to partial wrapping but require stronger adhesion energy to be fully engulfed. By taking into consideration adhesion energy, size, and rigidity

ratios between particles and vesicles, as well as the spontaneous curvature of the vesicle, the authors construct wrapping phase diagrams containing all wrapping states.

6.5 Moderating membrane permeability

Vesicle membranes are self-assembled bilayers of amphiphiles, and as such have a characteristic fluidity (as the term *fluid mosaic model* devised in 1972, describing a cell membrane, suggests).[101] This fluidity allows for ions and small molecules to pass

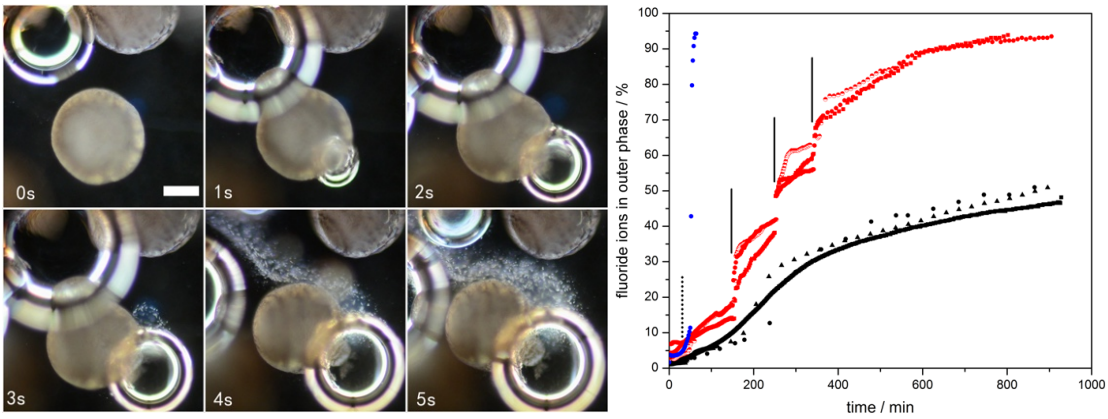

Figure 6.10 | Left: Dark microscopy sequence of video stills of a water-based (containing barium cations) dispersion of capsules with membrane embedded manganese oxide particles and loaded with sodium sulfate, after the addition of a large aliquot of hydrogen peroxide. The stills show the formation of oxygen bubbles, leading to deformation and rupture of the capsule membranes hereby releasing the sulfate ion content, as visualised by the formation of a stream of in-situ formed barium sulfate particles (a white haze). Scale bar: 150 μm. **Right:** Fluoride ion release profiles of water-based dispersions of *ca.* 6000 MnO_2 particle embedded capsules containing 0.2 mol dm^{-3} sodium fluoride (6 cm^3 of water outer phase, 0.1 cm^3 of inner aqueous phase) with (a) 3.0 cm^3 of 30 wt. % H_2O_2 added at 50 min (blue, dashed vertical line indicates time of hydrogen peroxide addition), (b) aliquots of 0.2 cm^3 of 3 wt. % H_2O_2 added at 150, 250 and 340 min (red, solid vertical lines indicate time of hydrogen peroxide addition), and (c) no H_2O_2 stimulus (black).

through the membrane and makes vesicles inherently leaky, thus an increase in membrane fluidity results in an increase in membrane permeability.

Here in the *BonLab*, we recently showed that embedding manganese oxide (MnO_2, *ca.* 3 μm) nanoparticles into the walls of giant polymer capsules allows for the regulation of membrane permeability by the introduction of a chemical trigger (see figure 6.10).[102] MnO_2 embedded poly(butyl methacrylate)-*block*-poly(2-(dimethylamino) ethyl methacrylate) capsules, approximately 300 μm in diameter, were synthesised using flow-focused microfluidics. Upon exposure to low concentrations of hydrogen peroxide, an enhancement in the rate of release of capsule contents is observed, whereas a high concentration causes capsule rupture and complete release. We hypothesise that the increase in release is due to an increase in capsule permeability caused by the catalytic activity of the particles, likely the generation of oxygen bubbles. This work is an example of chemically regulated membrane permeability and offers an alternative to the more traditional methods of regulation, such as membrane proteins or the other external triggers previously discussed.[12]

Heating gold nanoparticles has also been shown to be an effective way to increase membrane fluidity.[103] 200-500 nm diameter DPPC and distearoylphosphatidylcholine (90:10) liposomes were loaded with 1.4 nm diameter gold nanoparticles and exposed to 250 nm UV light. Irradiation causes local heating of the particles so they act as localised heat sources, absorbing UV radiation and transferring heat to the membrane. The authors hypothesise that the permeability of the bilayer is increased by the separation of gel and fluid phases, allowing the encapsulated dye calcein to escape. Interestingly, triggered release of the dye was observed when gold particles are on the outer and inner membrane, as well as when part of the membrane itself.

Amphiphiles can be assembled into giant unilamellar vesicles (GUVs) and multilamellar vesicles with diameters of 1 – 500 μm using microfluidic templating,[104] to generate a wide range of fascinating structures.[105] For example,

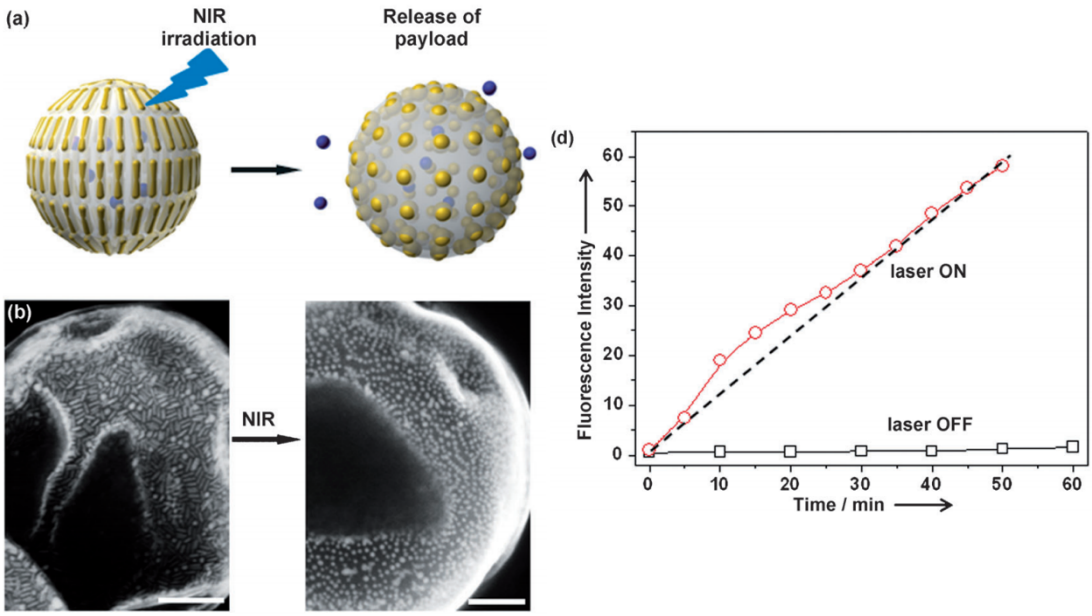

Figure 6.11 | (a) Near infrared triggered release using giant vesicles. The photo thermally induced shape deformation of gold nanorods into spherical nanoparticles creates extra spacing between particles for the release of encapsulated molecules. (b) SEM images of giant vesicles before and after exposure to the laser, showing the shape deformation. Scale bars are 200 nm. (d) The release profiles rhodamin B giant vesicles with laser on (○) and laser off (□). Reproduced with permission from Nie *et al.*[106]

Nie *et al.* formed gold nanorod embedded poly(ethylene oxide)-*block*-polystyrene (PEO-*b*-PS) vesicles (1.28 μm in diameter) from the microfluidic-assisted assembly of PEO-*b*-PS-tethered gold nanorods (40 nm by 10 nm), as shown in figure 6.11.[106] Upon irradiation with near infrared light (700 to 1000 nm), these vesicles can be burst to deliver a payload due to intense localised heating. Laser exposure causes the rods to deform into spherical nanoparticles due to photo thermally induced melting, and this shape deformation is theorised to create extra spacing between particles for the release of encapsulated molecules.

Remarkably, nanoparticles need not be embedded in the membrane itself, but can impact fluidity by simply being in close proximity to the vesicle.[107–114] Zasadzinski *et al.* showed that DPPC vesicles either loaded with, covered in, or found near hollow gold nanoshells (HGNs) could be irradiated with near infrared radiation to

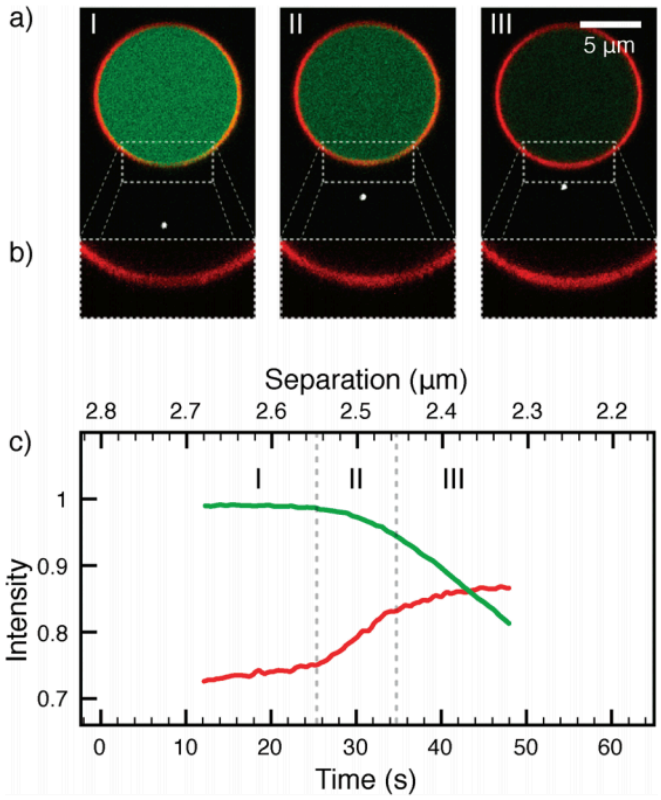

Figure 6.12 | Controlled leakage of a GUV upon approach of an optically trapped gold nanoparticle. (a) Confocal images of a GUV surface (red), its cargo (green), and an optically trapped gold nanoparticle (bright white spot) as the trapped nanoparticle approaches the GUV. (b) Zoom in on the membrane in the boxes of (a). (c) Intensity of the fluorophores in the boxed regions of (a) as a function of travelled distance, the alexa hydrazide signal (AH) is normalized by its initial value, the intensity of texas red is normalized by the initial AH value. The GUV becomes leaky around t = 26 s. Reproduced with permission from Oddershede *et al.*[110]

achieve near instantaneous release of liposome contents.[109] The laser-heated HGNs act as nanosonicators to temporally disrupt the lipid membrane, but are most effective when tethered to the vesicle surface. The membrane permeabilising power of a gold particle as a function of its distance from the vesicle was further investigated by Oddershede *et al.*, demonstrating the concept of 'controlled leakage' mediated by particle distance, as shown in figure 6.12.[110]

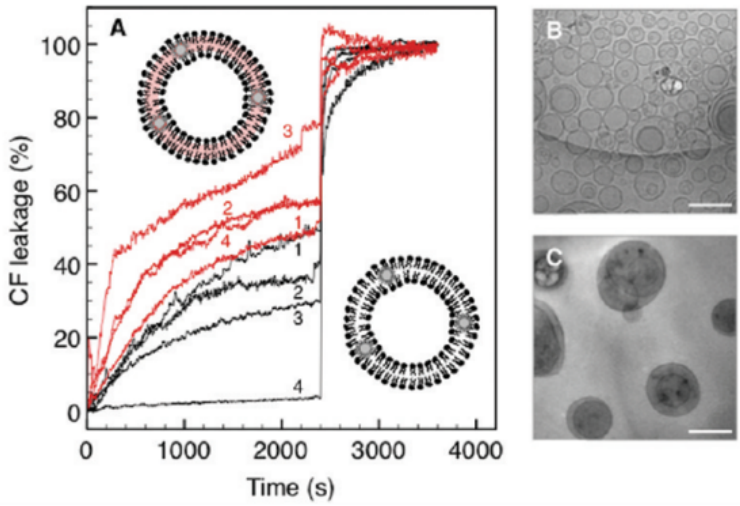

Figure 6.13 | Carboxyfluorescein (CF) leakage from bilayer-decorated magnetic liposomes (dMLs). (A) Percent CF leakage with (red) and without (black) radiofrequency heating at 250 A and 281 kHz for (1) DPPC and dMLs formed at lipid molecule to nanoparticle (L/N) ratios of (2) 25000:1, (3) 10000:1, and (4) 5000:1. The inset schematics (not to scale) in (A) depict dML heating with or without radiofrequency heating. Cryo-TEM images are shown at 10 mM lipid for (B) DPPC liposomes and (C) dMLs formed at a L/N ratio of 10000:1 (200 nm scale bars). Reproduced with permission from Bothun *et al.*[116]

Alternating magnetic fields (AMF) have also been shown to trigger release from vesicles containing iron oxide nanoparticles in their walls.[115] When AMF pulses were applied to PEGylated 2-distearoyl-sn-glycero-3-phosphocholine vesicles containing 5 nm diameter iron oxide particles in their walls, release rates of the membrane impermeable dye calcein increased. Critically, hyphenating 1 minute AMF pulses with 1 minute equilibrium periods resulted in a more constant release rate than in the case of longer pulsing cycles. It is not just the magnetic susceptibility of iron oxide that makes it a useful tool in membrane functionalisation. Exposure to radio frequencies (RF) causes nanoparticle heating and can lead to increased membrane permeability, as shown by Bothun *et al.* in figure 6.13.[116] 100 nm diameter DPPC vesicles containing 5 nm diameter oleic acid stabilised maghemite particles in their walls (confirmed by cryo-TEM) were loaded with solutions of the fluorescent dye carboxyfluorescein (CF). Dye leakage from the vesicles was significantly increased upon exposure to radio frequency (RF)

heating at optimum lipid molecule to nanoparticle ratios (5000:1, in this study), justified by a trade-off between structural changes and aggregation that impacts local heating and membrane permeability. The authors rightly consider that the inclusion of particles into membranes is, by design, disruptive to the membrane and can have a negative impact on vesicle stability. As many authors make clear, a balance between structural integrity and particle functionality must be sought, especially when attempting to moderate membrane permeability.[117–119]

These examples show that colloidal metal nanoparticles, specifically iron oxide, gold and silver, can act as effective heat transducers that directly impact the structural integrity of a vesicle membrane. In comparison to bulk heating, these composite systems provide the added benefit of precise spatial and temporal control. In fact, particles can still change membrane permeability without heating. Oh *et al.* showed that by simply including silver and gold nanoparticles in the walls, DPPC vesicle permeability could be increased.[120,121] By monitoring the movement of dye molecules in the membrane using fluorescent anisotropy spectroscopy, membrane fluidity is measured and showed to be higher for vesicles containing nanoparticles.

6.6 Taxis of vesicles using particles

Several of the examples discussed so far have used the release of vesicle contents as a probe for change in membrane structure. There are, however, composite vesicles that have been designed with triggered release as their primary function, capable of some rather unique behaviours.[102,122–131]

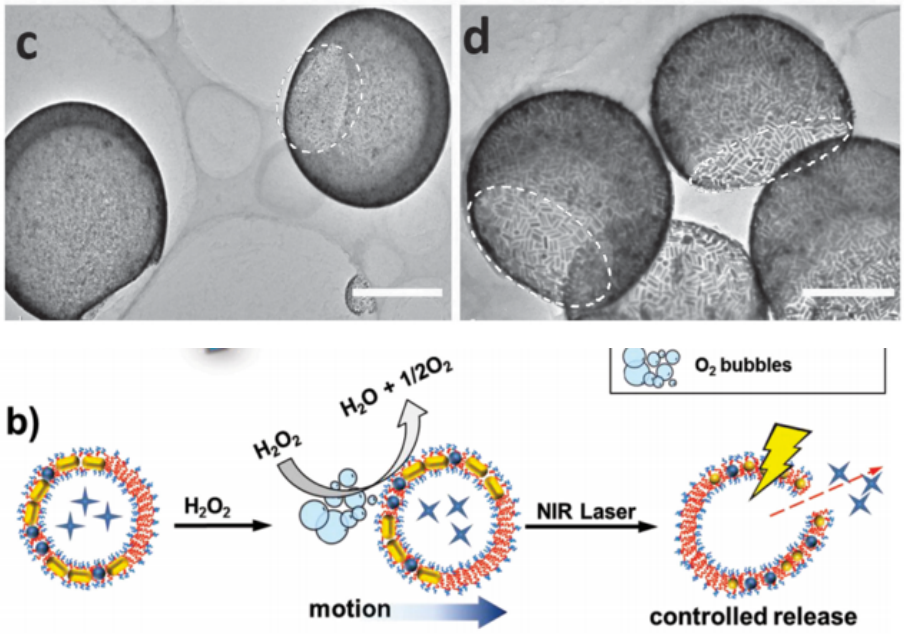

Figure 6.14 | Top: TEM images of composite vesicles containing platinum and gold nanoparticle rich domains, identified by the dashed circles. Scale bars are 1 μm in image (c) and 500 nm in image (d). **Bottom:** Scheme of the self-propelling of composite vesicles in the presence of hydrogen peroxide (H_2O_2) as fuel and the payload release from vesicles upon the irradiation of near infrared (NIR) light. Reproduced with permission from Nie *et al.*[122]

Extracellular vesicles form naturally during biological functions for purposes such as storage, transport, and communication,[132] therefore it is not surprising that synthetic vesicles have been designed to carry out similar tasks. One such example is the transport and delivery of a drug by Janus vesicles powered by platinum and gold nanoparticles, as shown in figure 6.14.[122] Vesicles were synthesised from a combination of free PEO-*b*-PS polymer and PEO-*b*-PS polymer tethered nanoparticles that phase separate during synthesis to yield Janus (two-faced) structures. Platinum catalyses the breakdown of hydrogen peroxide into water and oxygen bubbles, providing a source of propulsion when embedded into the walls of a vesicle. As the platinum particles are confined to one side of the vesicle it is propelled with direction, and once it arrives at its destination, a near infra-red laser heats the gold particles in the walls bursting the vesicle and releasing the encapsulated drug.

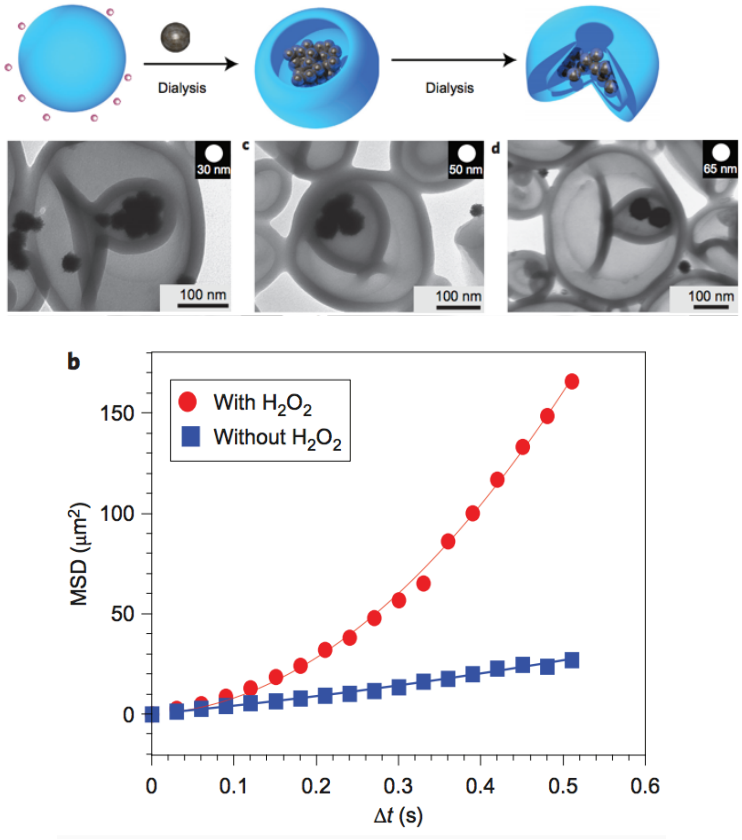

Figure 6.15 | Top: (a) Strategy for entrapping preformed platinum nanoparticles during the transformation of vesicles into stomatocytes. **Middle:** TEM images of entrapped nanoparticles of different sizes, namely 30, 50 and 65 nm. **Bottom:** Average mean square displacement (MSD) of the platinum-filled stomatocytes before and after the addition of 20 cm^3 H_2O_2, calculated from the tracking coordinates of 57 particles (the particles were selected from the upper part of the major size distribution). Reproduced with permission from Van Hest *et al.*[130]

Swimming, by means of bubble propulsion, is possible whether you're at the nano-[20] or millimetre length scale,[133] and as van Hest and Wilson note, these self-propelling objects are reminiscent of miniature rocket engines, as shown in figure 6.15.[130,134] Their work concerns the propulsion of so called *stomatocytes*, bowl shaped structures formed from the osmotic deformation of polymer vesicles. The stomatocytes have platinum nanoparticles entrapped within their cavities that, when exposed to hydrogen peroxide fuel, generate a rapid discharge of oxygen bubbles from their opening that induces movement. Their speed is determined not only by the concentration of the fuel in the continuous phase, but also by growing

temperature-sensitive polymer brushes on the motor. These polymer brushes moderate the stomatocyte opening size upon a temperature change, thus the hydrogen peroxide influx can be controlled and the vesicle's speed regulated. More recently, Battaglia *et al.* showed that synthetic vesicles could cross the blood-brain barrier by means of chemotactic transport.[135] By fabricating polymersomes from blends of two different copolymers, asymmetric structures are formed. These polymersomes are filled with glucose oxidase that catalyse the breakdown of glucose to D-glucono-δ-lactone and hydrogen peroxide, and catalase to catalyse the decomposition of hydrogen peroxide into water and oxygen. By forming the vesicle from polymers of different permeabilities, the reaction products are preferentially expelled from one region of the vesicle, thus generating a vesicle capable of directed self-propulsion. These loaded vehicles are able to penetrate the blood-brain barrier four times more effectively than their comparable non-chemotactic systems.

6.7 Conclusions

In this review, we have used a number of select examples to demonstrate the power of combining particles and vesicles in generating new superstructures. These nanocomposites have a wide range of functions and behaviours that take advantage of both the functional support provided by the vesicle and the associated active particles, in most cases yielding responsive entities. A number of our examples theorise the possibilities for particle-vesicle composites that are yet to be experimentally realised, and one can expect the next decade of research to present a host of new and exciting systems developed in all areas of science.

6.8 References

1 G. Wächtershäuser, *Mol. Microbiol.*, 2003, **47**, 13–22.

2 D. A. Hammer and N. P. Kamat, *FEBS Lett.*, 2012, **586**, 2882–2890.

3 J. C. Blain and J. W. Szostak, *Annu. Rev. Biochem.*, 2014, **83**, 615–640.

4 S. S. Mansy and J. W. Szostak, *Proc. Natl. Acad. Sci. U. S. A.*, 2008, **105**,

13351–13355.

5 J. N. Israelachvili, *Intermolecular and surface forces*, Academic Press, Cambridge, MA, 2011.

6 D. E. Discher and A. Eisenberg, *Science*, 2002, **297**, 967–973.

7 J. N. Israelachvili, D. J. Mitchell and B. W. Ninham, *Biochim. Biophys. Acta - Biomembr.*, 1977, **470**, 185–201.

8 M. P. Sheetz and S. J. Singer, *Proc. Natl. Acad. Sci. U. S. A.*, 1974, **71**, 4457–4461.

9 J. N. Israelachvili and D. J. Mitchell, *Biochim. Biophys. Acta*, 1975, **389**, 13–19.

10 B. M. Discher, Y.-Y. Won, D. S. Ege, J. C.-M. Lee, F. S. Bates, D. E. Discher and D. A. Hammer, *Science*, 1999, **284**, 1143–1146.

11 R. P. Brinkhuis, F. P. J. T. Rutjes and J. C. M. van Hest, *Polym. Chem.*, 2011, **2**, 1449–1462.

12 C. Schmitt, A. H. Lippert, N. Bonakdar, V. Sandoghdar and L. M. Voll, *Front. Bioeng. Biotechnol.*, 2016, **4**, 19.

13 V. P. Torchilin, *Nat. Rev. Drug Discov.*, 2005, **4**, 145–160.

14 P. J. F. Harris, *Int. Mater. Rev.*, 1995, **40**, 97–115.

15 B. Hvolbæk, T. V. W. Janssens, B. S. Clausen, H. Falsig, C. H. Christensen and J. K. Nørskov, *Nano Today*, 2007, **2**, 14–18.

16 W. H. De Jong and P. J. A. Borm, *Int. J. Nanomedicine*, 2008, **3**, 133–149.

17 M. Gaumet, A. Vargas, R. Gurny and F. Delie, *Eur. J. Pharm. Biopharm.*, 2008, **69**, 1–9.

18 D. A. Scott, *Stud. Conserv.*, 2016, **61**, 185–202.

19 A. R. Morgan, A. B. Dawson, H. S. Mckenzie, T. S. Skelhon, R. Beanland, H. P. W. Franks and S. A. F. Bon, *Mater. Horizons*, 2014, **1**, 65–68.

20 B. W. Longbottom, L. A. Rochford, R. Beanland and S. A. F. Bon, *Langmuir*, 2015, **31**, 9017–9025.

21 J. A. Bonham, M. A. Faers and J. S. van Duijneveldt, *Soft Matter*, 2014, **10**, 9384–9398.

22 A. D. Bangham, *Adv. Lipid Res.*, 1963, **1**, 65–104.

23 A. J. Skarnulis, P. J. Strong and R. J. P. Williams, *J. Chem. Soc. Chem.*

Commun., 1978, **0**, 1030–1032.

24 S. Mann, A. J. Skarnulis and R. J. P. Williams, *J. Chem. Soc. Chem. Commun.*, 1979, **0**, 1067–1068.

25 L. B. Margolis, V. A. Namiot and L. M. Kljukin, *Biochim. Biophys. Acta - Biomembr.*, 1983, **735**, 193–195.

26 K. Hong, D. S. Friend, C. G. Glabe and D. Papahadjopoulos, *Biochim. Biophys. Acta - Biomembr.*, 1983, **732**, 320–323.

27 M. Foldvari, G. T. Faulkner and M. Mezei, *J. Microencapsul.*, 1988, **5**, 231–241.

28 K. Gao and L. Huang, *Biochim. Biophys. Acta - Biomembr.*, 1987, **897**, 377–383.

29 P. Herve, F. Nome and J. H. Fendler, *J. Am. Chem. Soc.*, 1984, **106**, 8291–8292.

30 S. Mann and J. P. Hannington, *J. Colloid Interface Sci.*, 1988, **122**, 326–335.

31 J. L. Hutchison, S. Mann, A. J. Skarnulis and R. J. P. Williams, *J. Chem. Soc. Chem. Commun.*, 1980, **0**, 634–635.

32 Y. M. Tricot and J. H. Fendler, *J. Phys. Chem.*, 1986, **90**, 3369–3374.

33 H. J. Watzke and J. H. Fendler, *J. Phys. Chem.*, 1987, **91**, 854–861.

34 L. Zhang and A. Eisenberg, *Science*, 1995, **268**, 1728–1731.

35 E. Evans and M. Metcalfe, *Biophys. J.*, 1984, **46**, 423–426.

36 E. Evans and D. Needham, *J. Phys. Chem.*, 1987, **91**, 4219–4228.

37 S. Rangelov, K. Edwards, M. Almgren and G. Karlsson, *Langmuir*, 2003, **19**, 172–181.

38 D. D. Lasic, *Angew. Chemie Int. Ed. English*, 1994, **33**, 1685–1698.

39 K. Kostarelos, T. F. Tadros and P. F. Luckham, *Langmuir*, 1999, **15**, 369–376.

40 M. M. Mady and M. M. Darwish, *J. Adv. Res.*, 2010, **1**, 187–191.

41 F. Quemeneur, M. Rinaudo, G. Maret and B. Pépin-Donat, *Soft Matter*, 2010, **6**, 4471–4481.

42 R. Chen, D. J. G. Pearce, S. Fortuna, D. L. Cheung and S. A. F. Bon, *J. Am. Chem. Soc.*, 2011, **133**, 2151–2153.

43 X. Chen, G. Zou, Y. Deng and Q. Zhang, *Nanotechnology*, 2008, **19**, 195703.

44 F. De Persiis, C. La Mesa and R. Pons, *Soft Matter*, 2012, **8**, 1361–1368.

45 H. Pera, T. M. Nolte, F. A. M. Leermakers and J. M. Kleijn, *Langmuir*, 2014, **30**, 14581–14590.

46 K. Shigyou, K. H. Nagai and T. Hamada, *Langmuir*, 2016, **32**, 13771–13777.

47 R. Sarfati and E. R. Dufresne, *Phys. Rev. E*, 2016, **94**, 12604.

48 L. Zhang and S. Granick, *Nano Lett.*, 2006, **6**, 694–698.

49 L. Zhang, L. Hong, Y. Yu, S. Chul Bae and S. Granick, *J. Am. Chem. Soc.*, 2006, **128**, 9026–9027.

50 Y. Yu, S. M. Anthony, L. Zhang, S. Chul Bae and S. Granick, *J. Phys. Chem. C*, 2007, **111**, 8233–8236.

51 S. Savarala, S. Ahmed, M. A. Ilies and S. L. Wunder, *ACS Nano*, 2011, **5**, 2619–2628.

52 R. Michel, T. Plostica, L. Abezgauz, D. Danino and M. Gradzielski, *Soft Matter*, 2013, **9**, 4167–4177.

53 D. Pornpattananangkul, S. Olson, S. Aryal, M. Sartor, C.-M. Huang, K. Vecchio and L. Zhang, *ACS Nano*, 2010, **4**, 1935–1942.

54 A. M. Mihut, A. P. Dabkowska, J. J. Crassous, P. Schurtenberger and T. Nylander, *ACS Nano*, 2013, **7**, 10752–10763.

55 M. Sára and U. B. Sleytr, *J. Bacteriol.*, 2000, **182**, 859–68.

56 J. R. Young, S. A. Davis, P. R. Bown and S. Mann, *J. Struct. Biol.*, 1999, **126**, 195–215.

57 H. Aranda-Espinoza, Y. Chen, N. Dan, T. C. Lubensky, P. Nelson, L. Ramos and D. A. Weitz, *Science*, 1999, **285**, 394–397.

58 L. Ramos, T. C. Lubensky, N. Dan, P. Nelson and D. A. Weitz, *Science*, 1999, **286**, 2325–2328.

59 M.-H. Schmid-Wendtner and H. C. Korting, *Skin Pharmacol. Physiol.*, 2006, **19**, 296–302.

60 M. Shibayama and T. Tanaka, *Volume phase transition and related phenomena of polymer gels*, Springer Berlin Heidelberg, 1993.

61 Y. Li and T. Tanaka, *Annu. Rev. Mater. Sci.*, 1992, **22**, 243–277.

62 Y. Chen, N. Ballard, S. A. F. Bon, *Chem. Commun.*, 2013, **49**, 1524–1526.

63 Y. Chen, N. Ballard and S. A. F. Bon, *Polym. Chem.*, 2013, **4**, 387–392.

64 R. V. Bell, C. C. Parkins, R. A. Young, C. M. Preuss, M. M. Stevens and S. A. F. Bon, *J. Mater. Chem. A*, 2016, **4**, 813–818.

65 Y. Chen, N. Ballard, O. D. Coleman, I. J. Hands-Portman and S. A. F. Bon, *J. Polym. Sci. Part A Polym. Chem.*, 2014, **52**, 1745–1754.

66 G. Huang, Z. Hu and J. Wu, *Macromolecules*, 2003, **36**, 440–448.

67 Y. Chen, G. Nurumbetov, R. Chen, N. Ballard and S. A. F. Bon, *Langmuir*, 2013, **29**, 12657–12662.

68 M. Destribats, V. Lapeyre, M. Wolfs, E. Sellier, F. Leal-Calderon, V. Ravaine and V. Schmitt, *Soft Matter*, 2011, **7**, 7689.

69 W. Richtering, *Langmuir*, 2012, **28**, 17218–17229.

70 A. Šarić and A. Cacciuto, *Soft Matter*, 2013, **9**, 6677–6695.

71 S. Zhang, A. Nelson and P. A. Beales, *Langmuir*, 2012, **28**, 12831–12837.

72 X. Chen, F. Tian, X. Zhang and W. Wang, *Soft Matter*, 2013, **9**, 7592–7600.

73 K. Jaskiewicz, A. Larsen, D. Schaeffel, K. Koynov, I. Lieberwirth, G. Fytas, K. Landfester and A. Kroeger, *ACS Nano*, 2012, **6**, 7254–7262.

74 H. Al-Obaidi, B. Nasseri and A. T. Florence, *J. Drug Target.*, 2010, **18**, 821–830.

75 A. H. Bahrami, R. Lipowsky and T. R. Weikl, *Phys. Rev. Lett.*, 2012, **109**, 188102.

76 X. Yi, X. Shi and H. Gao, *Phys. Rev. Lett.*, 2011, **107**, 98101.

77 W. T. Góźdź, *Langmuir*, 2007, **23**, 5665–5669.

78 H. Noguchi and M. Takasu, *Biophys. J.*, 2002, **83**, 299–308.

79 S. Cao, G. Wei and J. Z. Y. Chen, *Phys. Rev. E*, 2011, **84**, 50901.

80 M. Dutt, M. J. Nayhouse, O. Kuksenok, S. R. Little and A. C. Balazs, *Curr. Nanosci.*, 2011, **7**, 699–715.

81 S. Lecommandoux, O. Sandre, F. Chécot, J. Rodriguez-Hernandez and R. Perzynski, *Adv. Mater.*, 2005, **17**, 712–718.

82 S. Lecommandoux, O. Sandre, F. Chécot, J. Rodriguez-Hernandez and R. Perzynski, *J. Magn. Magn. Mater.*, 2006, **300**, 71–74.

83 S. Lecommandoux, O. Sandre, F. Chécot and R. Perzynski, *Prog. Solid State Chem.*, 2006, **34**, 171–179.

84 I. Gözen, C. Billerit, P. Dommersnes, A. Jesorkaa and O. Orwar, *Soft Matter*, 2011, **7**, 9706–9713.

85 Y. Natsume, O. Pravaz, H. Yoshidab and M. Imai, *Soft Matter*, 2010, **6**, 5359–5366.

86 M. Paoluzzi, R. Di Leonardo, M. C. Marchetti and L. Angelani, *Sci. Rep.*, 2016, **6**, 34146.

87 I. Koltover, J. O. Rädler and C. R. Safinya, *Phys. Rev. Lett.*, 1999, **82**, 1991–1994.

88 A. Šarić and A. Cacciuto, *Phys. Rev. Lett.*, 2012, **108**, 118101.

89 S. D. Conner and S. L. Schmid, *Nature*, 2003, **422**, 37–44.

90 M. Deserno and W. M. Gelbart, *J. Phys. Chem. B*, 2002, **106**, 5543–5552.

91 K. A. Smith, D. Jasnow and A. C. Balazs, *J. Chem. Phys.*, 2007, **127**, 84703.

92 R. Lipowsky and H.-G. Döbereiner, *Europhys. Lett.*, 1998, **43**, 219–225.

93 O. Le Bihan, P. Bonnafous, L. Marak, T. Bickel, S. Trépout, S. Mornet, F. De Haas, H. Talbot, J.-C. Taveau and O. Lambert, *J. Struct. Biol.*, 2009, **168**, 419–425.

94 K. Jaskiewicz, A. Larsen, A. Kroeger, I. Lieberwirth, K. Koynov, W. Meier, G. Fytas and K. Landfester, *Angew. Chem. Int. Ed. Engl.*, 2012, **51**, 4613–4617.

95 P. Nandi, A. Charpilienne and J. Cohen, *J. Virol.*, 1992, **66**, 3363–3367.

96 R. J. Thibault, O. Uzun, R. Hong and V. M. Rotello, *Adv. Mater.*, 2006, **18**, 2179–2183.

97 W. H. Binder, R. Sachsenhofer, D. Farnik and D. Blaas, *Phys. Chem. Chem. Phys.*, 2007, **9**, 6435–6441.

98 H.-Y. Lee, S. H. R. Shin, L. L. Abezgauz, S. A. Lewis, A. M. Chirsan, D. D. Danino and K. J. M. Bishop, *J. Am. Chem. Soc.*, 2013, **135**, 5950–5953.

99 C. Dietrich, M. Angelova and B. Pouligny, *J. Phys. II Fr.*, 1997, **7**, 1651–1682.

100 X. Yi and H. Gao, *Langmuir*, 2016, **32**, 13252–13260.

101 S. J. Singer and G. L. Nicolson, *Science*, 1972, **175**, 720–731.

102 R. W. Jaggers, R. Chen and S. A. F. Bon, *Mater. Horiz.*, 2016, **3**, 41–46.

103 L. Paasonen, T. Laaksonen, C. Johans, M. Yliperttula, K. Kontturi and A.

Urtti, *J. Control. Release*, 2007, **122**, 86–93.

104 G. Nurumbetov, N. Ballard and S. A. F. Bon, *Polym. Chem.*, 2012, **3**, 1043–1047.

105 W. J. Duncanson, T. Lin, A. R. Abate, S. Seiffert, R. K. Shah and D. A. Weitz, *Lab Chip*, 2012, **12**, 2135–2145.

106 J. He, Z. Wei, L. Wang, Z. Tomova, T. Babu, C. Wang, X. Han, J. T. Fourkas and Z. Nie, *Angew. Chemie Int. Ed.*, 2013, **52**, 2463–2468.

107 T. Andersen, A. Kyrsting and P. M. Bendix, *Soft Matter*, 2014, **10**, 4268–4274.

108 T. Andersen, A. Bahadori, D. Ott, A. Kyrsting, S. N. S. Reihani and P. M. Bendix, *Nanotechnology*, 2014, **25**, 505101.

109 G. Wu, A. Mikhailovsky, H. A. Khant, C. Fu, W. Chiu and J. A. Zasadzinski, *J. Am. Chem. Soc.*, 2008, **130**, 8175–8177.

110 A. Kyrsting, P. M. Bendix, D. G. Stamou and L. B. Oddershede, *Nano Lett.*, 2011, **11**, 888–892.

111 A. S. Urban, M. Fedoruk, M. R. Horton, J. O. Rädler, F. D. Stefani and J. Feldmann, *Nano Lett.*, 2009, **9**, 2903–2908.

112 P. M. Bendix, S. N. S. Reihani and L. B. Oddershede, *ACS Nano*, 2010, **4**, 2256–2262.

113 P. M. Bendix, L. Jauffred, K. Norregaard and L. B. Oddershede, *IEEE J. Sel. Top. Quantum Electron.*, 2014, **20**, 15–26.

114 R. M. Gorgoll, T. Tsubota, K. Harano and E. Nakamura, *J. Am. Chem. Soc.*, 2015, **137**, 7568–7571.

115 E. Amstad, J. Kohlbrecher, E. Müller, T. Schweizer, M. Textor and E. Reimhult, *Nano Lett.*, 2011, **11**, 1664–1670.

116 Y. Chen, A. Bose and G. D. Bothun, *ACS Nano*, 2010, **4**, 3215–3221.

117 S. Ma, D. Qi, M. Xiao and R. Wang, *Soft Matter*, 2014, **10**, 9090–9097.

118 Y. Mai and A. Eisenberg, *J. Am. Chem. Soc.*, 2010, **132**, 10078–10084.

119 J. K. Sigurdsson and P. J. Atzberger, *Soft Matter*, 2016, **12**, 6685–6707.

120 S.-H. Park, S.-G. Oh, J.-Y. Mun and S.-S. Han, *Colloids Surf., B*, 2005, **44**, 117–122.

121 S.-H. Park, S.-G. Oh, J.-Y. Mun and S.-S. Han, *Colloids Surf., B*, 2006, **48**,

112–118.

122 L. Wang, Y. Liu, J. He, M. J. Hourwitz, Y. Yang, J. T. Fourkas, X. Han and Z. Nie, *Small*, 2015, **11**, 3762–3767.

123 B. Herranz-Blanco, L. R. Arriaga, E. Mäkilä, A. Correia, N. Shrestha, S. Mirza, D. A. Weitz, J. Salonen, J. Hirvonen and H. A. Santos, *Lab Chip*, 2014, **14**, 1083–1086.

124 C. Sanson, O. Diou, J. Thévenot, E. Ibarboure, A. Soum, A. Brûlet, S. Miraux, E. Thiaudière, S. Tan, A. Brisson, V. Dupuis, O. Sandre and S. Lecommandoux, *ACS Nano*, 2011, **5**, 1122–1140.

125 G. Béalle, L. Lartigue, C. Wilhelm, J. Ravaux, F. Gazeau, R. Podor, D. Carrière and C. Ménager, *Phys. Chem. Chem. Phys.*, 2014, **16**, 4077–4081.

126 S. Nappini, M. Bonini, F. B. Bombelli, F. Pineider, C. Sangregorio, P. Baglioni and B. Nordèn, *Soft Matter*, 2011, **7**, 1025–1037.

127 S. Nappini, M. Bonini, F. Ridi, P. Baglioni, *Soft Matter*, 2011, **7**, 4801–4811.

128 X. Ding, K. Cai, Z. Luo, J. Li, Y. Hu and X. Shen, *Nanoscale*, 2012, **4**, 6289–6292.

129 S. Nappini, T. Al Kayal, D. Berti, B. Nordèn and P. Baglioni, *J. Phys. Chem. Lett.*, 2011, **2**, 713–718.

130 D. A. Wilson, R. J. M. Nolte and J. C. M. van Hest, *Nat. Chem.*, 2012, **4**, 268–274.

131 F. Peng, Y. Tu, J. C. M. van Hest and D. A. Wilson, *Angew. Chemie*, 2015, **127**, 11828–11831.

132 S. El Andaloussi, I. Mäger, X. O. Breakefield and M. J. A. Wood, *Nat. Rev. Drug Discov.*, 2013, **12**, 347–357.

133 R. F. Ismagilov, A. Schwartz, N. Bowden and G. M. Whitesides, *Angew. Chemie Int. Ed.*, 2002, **114**, 674–676.

134 Y. Tu, F. Peng, X. Sui, Y. Men, P. B. White, J. C. M. van Hest and D. A. Wilson, *Nat. Chem.*, 2017, **9**, 480–486.

135 A. Joseph, C. Contini, D. Cecchin, S. Nyberg, L. Ruiz-Perez, J. Gaitzsch, G. Fullstone, X. Tian, J. Azizi, J. Preston, G. Volpe and G. Battaglia, *Sci. Adv.*, 2017, **3**, e1700362.

7 Summary

7.1 Thesis Outlook

To conclude this thesis, we will briefly discuss the outlook and future of each of the four experimental chapters presented. Chapters 1 – 4 describe the addition of catalysts, either biological or inorganic, to soft polymeric structures, namely ionically cross-linked hydrogels or capsules, to generate responsive composite materials.

In chapter 1, we reported independent responsive behaviour and communication in hydrogel alginate-based objects, namely fibres and beads, which have an individually programmed time delay in their response to a shared environmental stimulus. We utilised the enzyme urease to programme a self-regulated change in pH, which in turn activated the designed response of gel fibre disintegration or a change in gel bead colour. This design allowed for independent response behaviour of a collection of bodies in a single closed system, as well as inter-material communication on shorter length scales.

Future work: In the context of this study, the release of oil droplets was simply a visual marker. These oil droplets could also be loaded with a payload that one might want to deliver after a defined time period. We envisage the release of fragrances using this time-programmed setup, and have conducted some preliminary experiments in this area by means of headspace gas chromatography – mass spectrometry (GC-MS). Fibres, with their oil droplets still intact, release loaded fragrances slowly, as the oil-loaded fibre sits in an aqueous environment that acts as a barrier to release to the gas phase above. Once the oil droplets are released, they float to the top and form a thin film on the surface with direct contact to the gas phase, hereby promoting fragrance release. Such a mechanism can be used to create a multi-tiered fragrance system; after 5 minutes, lavandin oil

(lavender) is released, after 10 minutes vanillin (vanilla), and after 20 minutes limonene (oranges).

Furthermore, these fibres could be used to passively release volatile compounds. If the weight percent of alginate polymer is increased from 1 wt. % to 10 wt. % and the fibre is dried, a relatively strong fibre containing a series of oil-loaded reservoirs along its length is created. This oil phase could contain a compound one wished to release in small amounts over extended time-scales (*ca.* months), such as insect repellents. We are currently investigating the rate of release of such compounds from these fibres.

Chapter 2 naturally builds on the work of chapter 1 and demonstrates the design and fabrication soft composite hydrogel objects with temporal and spatial programming. Objects are, again, formed from the biopolymer sodium alginate, the enzyme urease, and oil droplets are formed by a simple gelation procedure to produce autonomous bodies with both time and spatial programming. These continuous objects of non-uniform dimensional composition selectively respond to an environmental stimulus of urea and change colour or disintegrate at pre-defined locations within the hydrogel structure after pre-set time intervals.

Future work: In the context of this work, decomposition of the hydrogel is used to demonstrate time and spatial programming in a large object with variation across its structure. Selective decomposition is only one example of a material response, however, and it occurs in response to a single, specific trigger, that being the pH increase generated by the enzyme urease. To advance the concept of a single soft object with time and spatial programming, more stimuli-response mechanisms should be introduced, to generate a multi-functional object.

These mechanisms are not limited to the enzymatic, and would be selected based on the application one had in mind. For example, a second-generation soft object might take the form of a soft object that can decompose, as we demonstrate, but also self-propel by the generation of oxygen bubbles by gold, platinum or catalase.

This swimming object, which decomposes after a set time period to deliver a payload, may also need to change its shape to get through a gate of specific shape and size. In this case, a polymer with an accessible phase transition temperature (such as poly(N-isopropyl acrylamide)[1] or poly(2-(dimethyl amino)ethyl methacrylate)[2] could be included to introduce regions that can contract upon a change in temperature. This would create a multi-functional object that erases itself after completing its designated task.

Furthermore, objects would ideally be made in a more sophisticated way than by the use of printed templates. Additive layer manufacturing (ALM), the building of 3D-objects by successive layers, could be used to generate more complex and intricate structures than can be accessed using templates. For example, soft objects have recently been built in this way by Lewis, Wood *et al.*[3] and Qi, Dunn, *et al.*.[4]

Chapter 3 further explores the concept of chemical communication touched upon in chapter 1, and looks at increasing the complexity of such communication between millimetre-sized soft hydrogel beads in an aqueous environment. Silver cations and the Ag^+ chelator dithiothreitol (DTT) are used as signalling molecules that, by exploiting their interplay with the enzyme urease, are used to conduct a series of 'conversations' between millimetre-sized beads. Competitive communication between three beads, whereby a central bead receives two competing signals from two senders, is shown.

Future work: The next steps of this research chapter are not trivial. The communication demonstrated here is incredibly simple, especially when directly compared to that which nature is capable of, so taking the concepts developed here further will mean one of two things.

Firstly, it could mean making the communication pathways much more complex, likely by borrowing these from nature. Tools such as cell proteins, receptors and chemical messengers (e.g. hormones or neurotransmitters) could be employed, or cells could be directly introduced into the soft structures themselves.

Secondly, it could mean integrating the simple chemical communication between urease, silver (Ag^+) and dithiothreitol into a more complex structure, such as the larger objects that feature in chapter 2. One could envisage a single soft object, made up of chemically distinct modules (or segments) that are programmed to communicate with each other, in response to their environment. This environmental cue could be the presence of urea, but it could also be a second soft object that needs to make contact with the first in order to induce a response. This route of development is akin to soft robotic communication, and would be an exciting extension of this preliminary study.

Chapter 4 looked at using inorganic catalysis as a tool for making responsive soft materials, where capsule membrane permeability is controlled using catalytic particles. Giant polymer capsules which have membrane-embedded catalytically active manganese oxide particles are made using droplet-based microfluidics. It was demonstrated that these colloidal particles can regulate the membrane permeability of the capsules upon their exposure to, and catalytic reaction with, small amounts of dissolved hydrogen peroxide.

Future work: Following the studies conducted in this chapter, several questions are still outstanding. Firstly, *what is the role of ionic charge (on both the capsule itself and the ions released) on the observed release rate?* Further experiments should ideally study the release of negatively charged fluoride ions from a negatively charged capsule (e.g. one formed from polystyrene-b-poly(acrylic acid)[5]), as well as release of positively charged ions (e.g. K^+, Ca^{2+}) from the same pBMA-*b*-pDMAEMA capsules used in the chapter. We anticipate that a difference in release profile will be observed on account of interactions between the capsule and its contents.

Our second question is*, what impact does shielding a capsule have on the rate of content release?* Capsules armoured by a shell of particles or nanoplates adhered to the capsule surface (by means of electrostatic attraction)[6] would presumably have different release behaviours to 'naked' ones due to the physical barrier between the

capsule and its bulk environment. Furthermore, a shielded capsule which loses its outer shell upon an external trigger could allow for 2 step release profiles, potentially useful in the delivery of active agents.

A third question we have is *how exactly does a catalytic particle modify the membrane permeability?* To answer this, we need to take a closer look at the particle-embedded membrane structure before, during and after the addition of a hydrogen peroxide trigger. We hope to do this with a technique such as small angle x-ray scattering (SAXS) or alternative x-ray spectroscopic methods. Ideally, these techniques will also tell us a little more about the capsule's membrane structure in the absence of particles (i.e. *is it amorphous, multilamellar or something else?*).

One further application of this work is the creation of Janus capsules, which we are able to produce. Unfortunately, we are yet to identify a use for them. Experiments have been conducted to try and induce self-propulsion by means of oxygen bubble production, however *ca.* 10 wt. % of hydrogen peroxide is required to move an object of this size (a concentration at which capsules rupture). To fix this, capsules need to be made more robust. Indeed, gelation of the internal capsule cavity by introduction of sodium alginate followed by calcium cross-linking does make objects strong enough to swim, however the capsule itself still ruptures. The alternative use of a Janus capsule could be spatially selective release of a capsule encapsulated compound, from one face only. This could be of use in the realms of nanoreactor design.

7.2 References

1 G. Huang, Z. Hu and J. Wu, *Macromolecules*, 2003, **36**, 440–448.

2 M. Okubo, H. Ahmad and T. Suzuki, *Colloid Polym. Sci.*, 1998, **276**, 470–475.

3 M. Wehner, R. L. Truby, D. J. Fitzgerald, B. Mosadegh, G. M. Whitesides, J. A. Lewis and R. J. Wood, *Nature*, 2016, **536**, 451–455.

4 Z. Ding, C. Yuan, X. Peng, T. Wang, H. J. Qi and M. L. Dunn, *Sci. Adv.*,

2017, **3**, e1602890.

5 A. Choucair, C. Lavigueur and A. Eisenberg, *Langmuir*, 2004, **20**, 3894–3900.

6 R. Chen, D. J. G. Pearce, S. Fortuna, D. L. Cheung and S. A. F. Bon, *J. Am. Chem. Soc.*, 2011, **133**, 2151–2153.